

Simulation Model Development and Investigation of a Range Extender based on a Switched Reluctance Generator

Master's Thesis

by Muneer Al Sabbagh

Friday 25th May, 2012

Declaration

I, Muneer Al Sabbagh, hereby declare that this submission – except for the supervision by the Institute for Power Electronics and Electrical Drives (ISEA) of RWTH Aachen University – is solely my own work. Information derived from the published or unpublished work of others has been acknowledged in the text and a list of references is given.

Aachen, Friday 25th May, 2012

Contents

1	Introduction										
2	Bac	Background									
	2.1	Range	Extender	2							
	2.2	Switch	ned Reluctance Machine								
		2.2.1	Principle of Operation								
		2.2.2	Operation Strategy	7							
		2.2.3	Multi-phase Machines	11							
		2.2.4	-	12							
		2.2.5	Losses in Switched Reluctance Drive Systems	13							
		2.2.6	Acoustic Noise in Switched Reluctance Drive Systems	17							
		2.2.7	Control of Switched Reluctance Generators	18							
	2.3	Genet	ic Algorithms	19							
		2.3.1	Parent Selection	19							
		2.3.2	Offspring Creation	20							
		2.3.3	Replacement	21							
3	Mod	del		22							
	3.1	Switch	ned Reluctance Generator	22							
	3.2	Power	Electronics Converter	26							
	3.3	DC-lin	ık	26							
	3.4	Batter	ту	28							
		3.4.1	Real Battery Model	28							
		3.4.2	Ideal Battery Model	29							
	3.5	Intern	al Combustion Engine	30							
	3.6		unical System	33							
	3.7		, Losses and Efficiency Calculations	34							
		3.7.1	Power Calculations	36							
		3.7.2	Iron Losses	36							
		3.7.3	Converter Losses	45							
		3.7.4	Ohmic Losses	46							
		3.7.5		46							
		3.7.6	Efficiency	46							
4	Optimization and Analysis 4										
	4.1	Optim	nization Process	47							
		4.1.1	Chromosome	48							
		4.1.2	Fitness Value	48							

Contents

Bi	Bibliography						
Li	List of Tables						
Lis	st of	Figures	5	72			
5	Con	clusion	s and Further Work	71			
	4.5	Summ	ary of Efficiency and Radial Force Optimization Processes	69			
		4.4.5	Efficiency and Excitation Penalty Optimization	68			
		4.4.4	Efficiency and RMS Current Optimization				
		4.4.3	Using the Real Battery Model				
		4.4.2	Effects of Varying System Parameters				
		4.4.1	Influence of Free-wheeling on Efficiency				
	4.4		nization for Maximum Efficiency				
		4.3.5	Using the Real Battery Model				
		4.3.4	Effects of Varying Battery Open-Circuit Voltage				
		4.3.2 4.3.3	Effects of Varying Cable Inductance				
		4.3.1	Effects of Varying Coble Industrance				
	4.3		nizaton for Minimum Radial Forces				
4.2 Example of Optimized Range Extender Operation							
	4.0	T		F (

1 Introduction

This thesis presents the modeling, analysis and optimization of a range extender. A range extender system is a system that extends the range of electric vehicles by charging the battery pack on-board. In this particular system the generation is done by a switched reluctance generator (SRG) that is driven by an internal combustion engine (ICE). The generated electric power is transferred to the battery pack using a power electronic (PE) converter and a DC-link acting as a buffer. An overview of the range extender studied in this work is shown in Figure 1.1. A complete system model is implemented in MATLAB/Simulink. In addition, the performance of the system is optimized for two criteria, which are minimum peak radial forces and maximum efficiency. Furthermore, parameter variations and limitations imposed by the system components are analyzed.

The thesis starts with a background chapter that includes an overview of range extender systems, switched reluctance machines, and genetic algorithms. Next, system modeling is explained using mathematical formulas and block diagrams. In the third chapter the optimization process is elucidated, and results of parameter variations are presented. Conclusions are drawn in the last chapter.

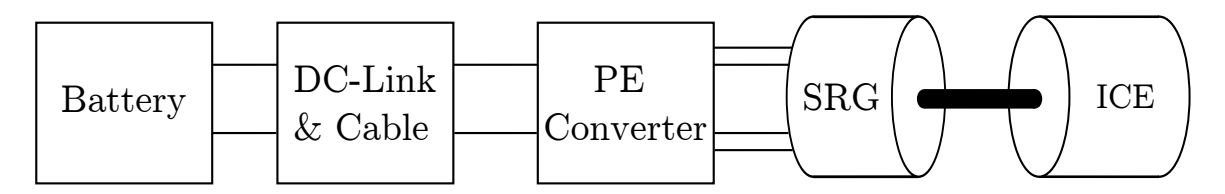


Figure 1.1: Block Diagram of Range Extender System

2.1 Range Extender

Since fuel-dependant vehicles are a major cause for air pollution and climate changes, electric vehicles and hybrid-electric vehicles are being developed to replace these conventional on-road vehicles [2, 11]. These vehicles under development rely on electric motors (EMs) for propulsion, and use battery packs as a primary or secondary storage for energy. An electric vehicle (EV) uses only the energy stored in the batteries for powering up the EMs. To charge the batteries an EV must be connected to a stationary power supply, and it can go as much as the energy stored in the battery allows. On the other hand, a hybrid-electric vehicle (HEV) utilizes an internal combustion engine (ICE) to provide traction power along with the EMs. The ICE could be a gasoline or a diesel engine, with the latter being the preferable choice because it is more efficient [11].

A HEV can be configured in two ways. In the first one, commonly known as series-hybrid, an ICE drives a generator that supplies the EMs with electric power. This means that propulsion is solely done by motors. Although the ICE is operated at the most optimum point, this configuration suffers from low efficiency, because there are two power conversion stages [11]. The other configuration is called the parallel-hybrid, wherein the ICE shares traction duties with the EMs, thereby increasing propulsion capabilities. When only the ICE is working, the EM can function as a generator to charge the batteries. Since EMs are more efficient at low speeds, they are used for traction, while at high speeds the ICE alone or both the ICE and the EMs can be used [11].

However, the goal to be completely independent of fuel energy for transportation is difficult to achieve. The reason for this is the limited capacity of batteries, which implies that vehicles that completely depend on them have limited driving ranges [2]. As a result, the idea to be less dependent on fuel as much as possible and to maximize the battery utilization seems appealing. This can be accomplished by the so-called range extender. A range extender extends the capacity of the battery pack by charging them on-board. It employs a small ICE and a generator, and the generator can also be used as the engine starter. Unlike the charging systems in HEVs, a range extender system has a lower rating than the battery pack [2].

Several range extenders are available commercially. Lotus has developed a range extender with three output variants of 20, 35 and 50 kW. The engines used are either 2- or 3-cylinder gasoline engines and run at speeds between 1500 and 3500 rpm. Generation is done by synchronous motors [24]. In addition, a 22-kW range extender has been developed by Polaris Industries, which makes use of a single-cylinder engine [23].

2.2 Switched Reluctance Machine

The switched reluctance (SR) machine is an electric machine, whose principle of operation has been first introduced in 1840 [29], and has been heavily investigated in the past few decades with the advent of cheap power electronic switches and [10]. Unlike other electrical machines, the torque in a SR machine is not generated due to the Lorentz force but rather due to the reluctance torque. This way of torque generation makes room for attractive advantages of the SR machine such as the absence of commutator, windings or permanent magnets on the rotor. Other advantages of the SR machine compared to other machines are the simpler and more rigid structure and more robust driving circuitry [10]. The SR machine is, however, plagued with several disadvantages like higher torque ripples, higher acoustic noise levels, and more complex mathematical models. Despite that, the SR machine is found in many household applications and in applications with tough conditions.

A SR machine has a doubly-salient structure. That is, both the rotor and stator have prominent teeth. Only the stator has windings, which are wound around each stator tooth. Figure 2.1 shows a two-phase SR machine with 8 stator teeth, 4 rotor teeth. Each phase is composed of 4 windings, and these winding can be connected in series, parallel or a combination of both.

The relationship between the number of stator teeth N_s , number of phases $N_{\rm ph}$ and number of magnetic pole pairs p is given by

$$N_{\rm s} = 2pN_{\rm ph} \tag{2.1}$$

Another characteristic parameters in the structure of a SR machine are the stator pole width β_s and the rotor pole width β_r as shown in Figure 2.1. In addition, the stator interpolar arc τ_{sp} and the rotor interpolar arc τ_{rp} , which are the angle difference between two adjacent stator and rotor teeth, respectively, are shown in Figure 2.1.

Due to the symmetry of the rotor, one can become independent of the machine configuration by utilizing the rotor electrical angle instead of the mechanical angle. In the SR machine shown in Figure 2.1, the rotor repeats itself every $\tau_{\rm rp}$. If this angle is assumed to be one period, then $\theta_{\rm e}$ is related to $\theta_{\rm m}$ by $N_{\rm r}$.

$$\theta_{\rm e} = N_{\rm r} \cdot \theta_{\rm m} \tag{2.2}$$

2.2.1 Principle of Operation

To see how the SR machine works, it is sound to consider a one-phase machine first and then generalize the concepts to multi-phase SR machines. A one-phase SR machine that has two stator teeth and two rotor teeth is shown in Figure 2.2. The windings of this machine are excited by a current source that is a function of rotor angle $\theta_{\rm m}$. When the windings carry current, a flux is created that will try to align the rotor teeth with the stator teeth [10, 21]. Hence, a torque pulse is generated whenever a rotor tooth is being forced to align

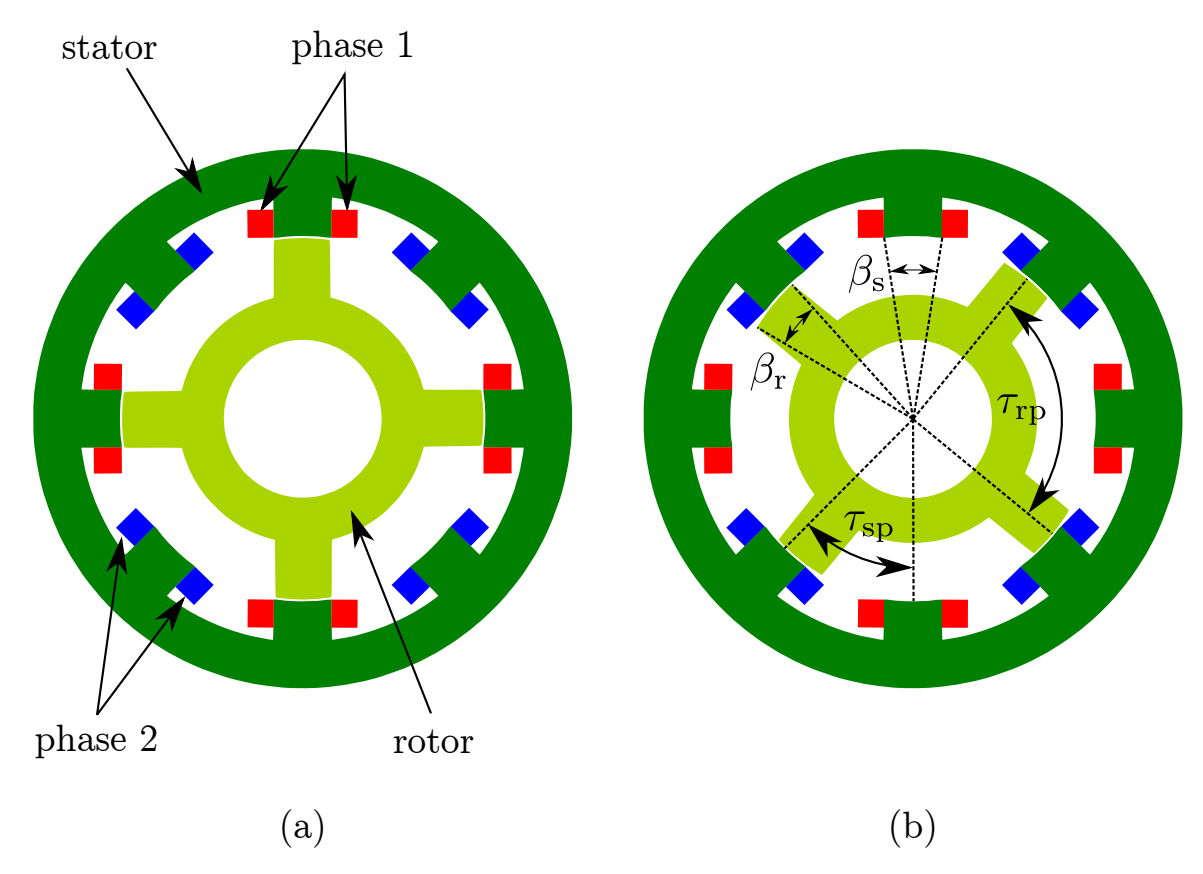


Figure 2.1: Cross-sectional View of a Switched Reluctance Machine

with a stator tooth. As the rotor completes one revolution, a stator tooth will face two rotor teeth, and, hence, two torque pulses are generated every one complete mechanical revolution.

The position at which stator and rotor teeth are aligned is called the aligned position θ^{a} . This position exhibits minimum reluctance seen by the flux. Since the inductance is inversely proportional to reluctance [31], the inductance is at maximum at the aligned position. Likewise, the unaligned position θ^{u} is defined for maximum reluctance (or minimum inductance).

The mathematical formulation of the terminal voltage of a one-phase SR machine leads to the equivalent circuit diagram. From Figure 2.2, the terminal voltage u is equal to

$$u(i,\theta_{\rm m}) = Ri + \frac{\mathrm{d}\psi(i,\theta_{\rm m})}{\mathrm{d}t}$$
 (2.3)

where R is the phase resistance, and ψ is the flux-linkage that depends on current i and rotor angle $\theta_{\rm m}$. Splitting the flux-linkage derivative into its partial derivatives, Equation (2.3) can be rewritten as

$$u(i,\theta_{\rm m}) = Ri + \left[\frac{\partial \psi(i,\theta_{\rm m})}{\partial i}\right]_{\theta_{\rm m}={\rm const}} \frac{\mathrm{d}i}{\mathrm{d}t} + \omega_{\rm m} \left[\frac{\partial \psi(i,\theta_{\rm m})}{\partial \theta_{\rm m}}\right]_{i={\rm const}}$$
(2.4)

where $\omega_{\rm m}$ is the shaft speed and is equal to

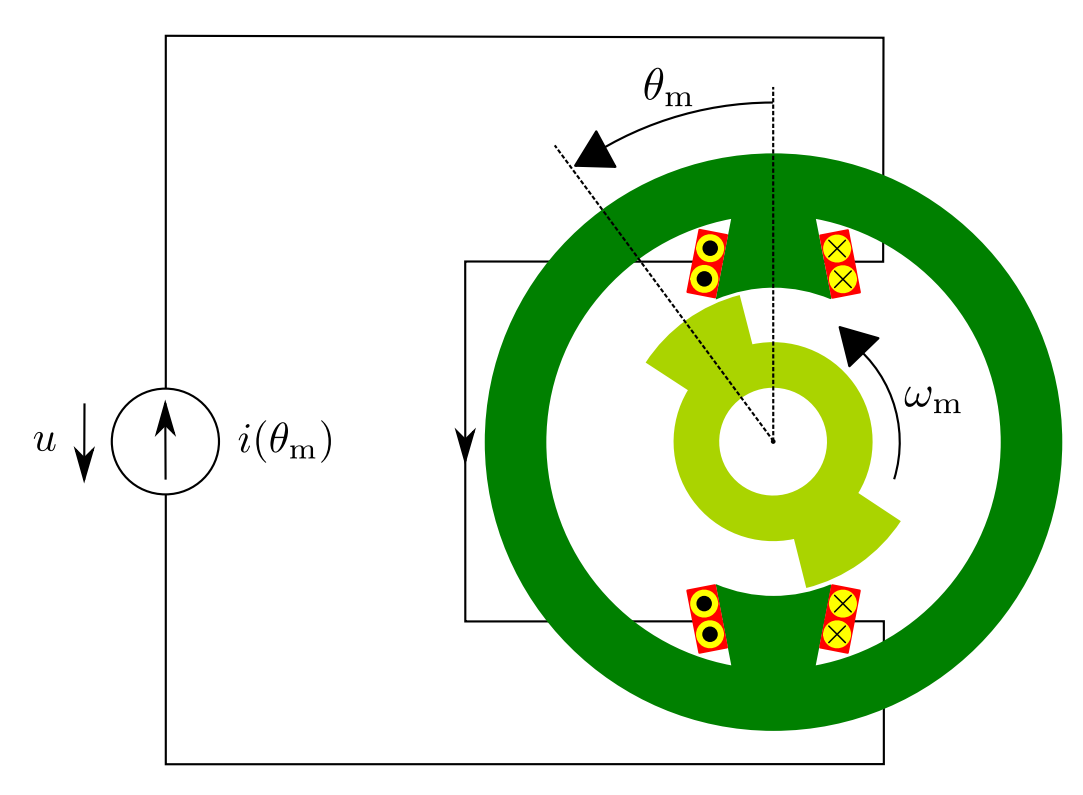


Figure 2.2: One-phase Switched Reluctance Machine

$$\omega_{\rm m} = \frac{\mathrm{d}\theta_{\rm m}}{\mathrm{d}t} \tag{2.5}$$

Equation (2.4) shows three voltage quantities: the first one is an ohmic voltage drop, the second is a voltage drop across an inductance, and the third is a back-EMF. Thus, the inductance and the back-EMF are defined as follows.

$$l(i,\theta_{\rm m}) = \left[\frac{\partial \psi(i,\theta_{\rm m})}{\partial i}\right]_{\theta_{\rm m}={\rm const}}$$
(2.6)

$$u_{\rm e}(i,\theta_{\rm m}) = \omega_{\rm m} \left[\frac{\partial \psi(i,\theta_{\rm m})}{\partial \theta_{\rm m}} \right]_{i={\rm const}}$$
 (2.7)

Combining Equations (2.4), (2.6) and (2.7), Equation (2.8) results from which the equivalent circuit diagram shown in Figure 2.3 is derived.

$$u(i,\theta_{\rm m}) = Ri + l(i,\theta_{\rm m}) \frac{\mathrm{d}i}{\mathrm{d}t} + u_{\rm e}(i,\theta_{\rm m})$$
(2.8)

The field energy $W_{\rm f}$ of the phase is [10, 21]

$$W_{\rm f}(i,\theta_{\rm m}) = \left[\int_0^{\psi} i(\psi,\theta_{\rm m}) d\psi \right]_{\theta_{\rm m}={\rm const}}$$
(2.9)

and the instantaneous torque $T_{\rm e}$ of the SR machine is

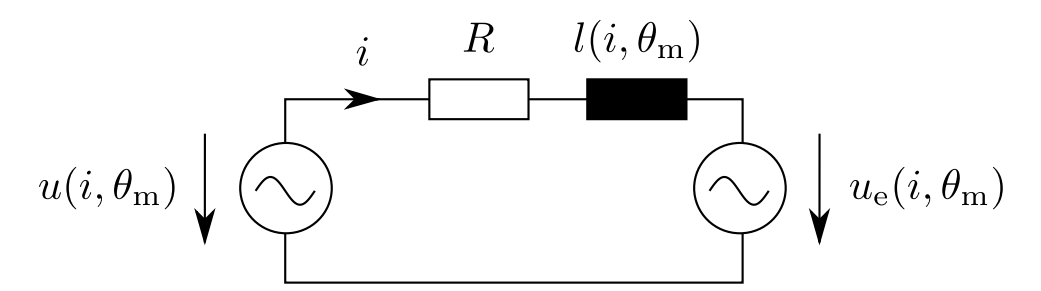


Figure 2.3: Equivalent Circuit Diagram of a One-phase Switched Reluctance Machine

$$T_{\rm e}(i,\theta_{\rm m}) = \left[\frac{\partial}{\partial \theta_{\rm m}}(i\psi - W_{\rm f}(i,\theta_{\rm m}))\right]_{i={\rm const}}$$
(2.10)

The right-hand side of Equation (2.10) is called the co-energy, and is defined by

$$W_{\rm f}'(i,\theta_{\rm m}) = \left[\int_0^i \psi(i,\theta_{\rm m}) di \right]_{\theta_{\rm m} = {\rm const}}$$
(2.11)

Hence, $T_{\rm e}$ can also be expressed in terms of $W'_{\rm f}$.

$$T_{\rm e}(i,\theta_{\rm m}) = \left[\frac{\partial W_{\rm f}'(i,\theta_{\rm m})}{\partial \theta_{\rm m}}\right]_{i={\rm const}}$$
(2.12)

Linear SR Machine

The complexity of SR machines stems from the fact that the machine is usually pushed into saturation to have a better utilization of the magnetic energy [10, 21]. By neglecting magnetic saturation a better insight on the torque generation mechanism can be achieved. For a linear SR machine, the inductance is a function of rotor angle only.

$$l(i,\theta_{\rm m}) = L(\theta_{\rm m}) \tag{2.13}$$

The flux-linkage ψ is in this case

$$\psi = L(\theta_{\rm m})i\tag{2.14}$$

Combining Equations (2.11), (2.12) and (2.14) an expression for the instantaneous torque of a linear SR machine is obtained.

$$T_{\rm e}(\theta_{\rm m}) = \frac{1}{2} i^2 \frac{\mathrm{d}L(\theta_{\rm m})}{\mathrm{d}\theta_{\rm m}} \tag{2.15}$$

Two important information can be deduced from Equation (2.15). The first one is the fact that torque is proportional to the square of the current. This implies that whether the current is positive or negative has no influence on the polarity of torque. The other piece of information one can conclude from Equation (2.15) is the influence of the phase inductance. If the phase winding carries current and the phase inductance is increasing with respect to rotor angle, positive torque is generated and the machine is operated in the motoring mode.

Likewise, if the phase inductance is decreasing, the machine is operated in the generating mode since negative torque is produced according to Equation (2.15). A linear profile of the phase inductance is shown in Figure 2.4 in which the motoring and generating regions are marked.

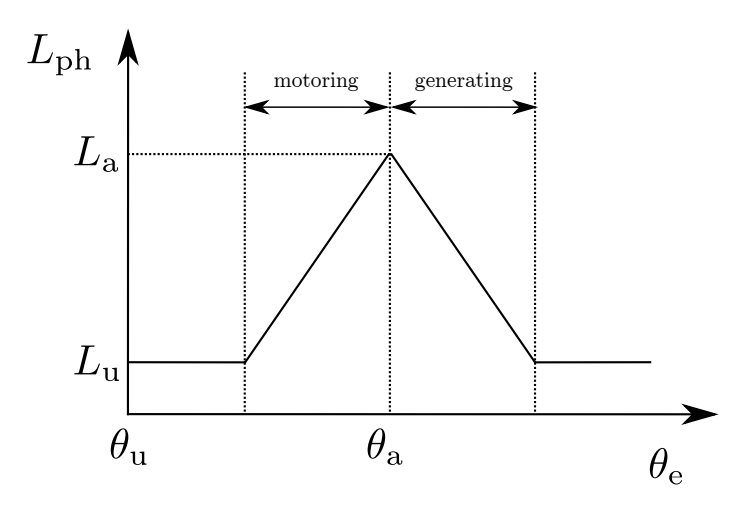


Figure 2.4: Linear Variations of Phase Inductance with Rotor Position

Using Equations (2.7), (2.13) and (2.14), the back-EMF of a linear SR machine is

$$u_{\rm e} = \omega_{\rm m} i \frac{\mathrm{d}L}{\mathrm{d}\theta_{\rm m}} \tag{2.16}$$

Therefore, like the torque, the back-EMF polarity is dependent on the sign of $dL/d\theta$.

2.2.2 Operation Strategy

The basic idea to operate a SR machine as a motor does not differ much from operating it as a generator. A switched reluctance motor (SRM) works by having a suitable amount of current in the phase while the phase inductance is increasing with respect to rotor position (Equation (2.15)). The same idea applies for the switched reluctance generator (SRG) except that the inductance must be decreasing with respect to rotor position. Because of this similarity in operation only the operation of the SRG is considered from this point. However, overcurrents may occur in the generating mode at high speeds if the back-EMF is very large, and this may result in higher torque pulsations and thermal overloading of the power electronic devices [18].

In one electrical cycle the following must be accomplished to operate a SRG successfully:

- 1. phase excitation by applying a positive voltage to the phase to achieve an adequate current level
- 2. phase demagnetization by feeding the current back to the load

A common converter used to implement the aforementioned procedure is the asymmetric half-bridge (AHB) converter, which is shown in Figure 2.5. The phases of an AHB converter are equal to $N_{\rm ph}$. Each phase contains two switches and two diodes. The phase voltage $u_{\rm ph}$ could vary between $U_{\rm DC}$, 0 and $-U_{\rm DC}$ depending on the switching state. In total there are of 4 possible switching states that are tabulated in Table 2.1.

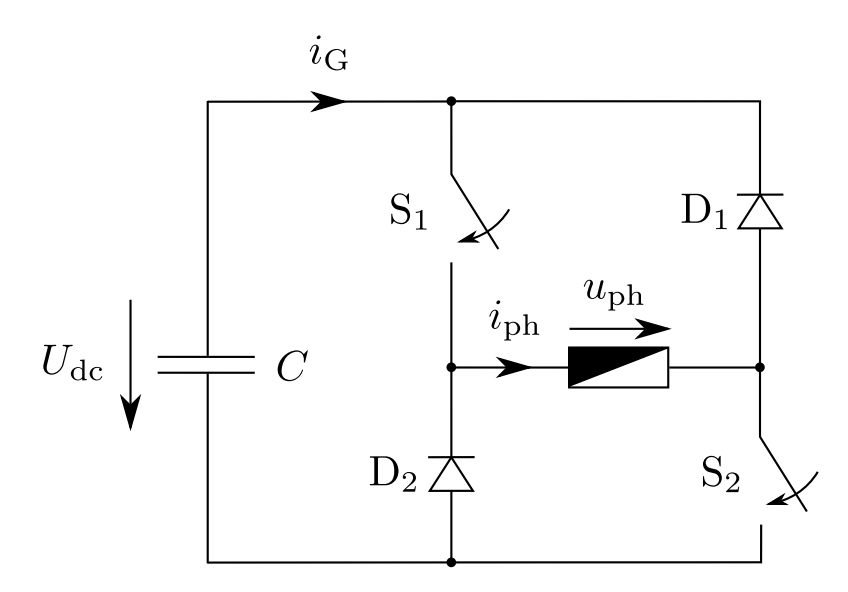


Figure 2.5: One-phase Asymmetric Half-bridge Converter

Table 2.1: States the Asymmetrical Half-bridge Converter

Conducting Devices	$u_{ m ph}$
$S_1 \& S_2$	$U_{\rm DC}$
$S_1 \& D_1$	0
$S_2 \& D_2$	0
$D_1 \& D_2$	$-U_{\rm DC}$

Below base speed the back-EMF voltage is smaller than the phase voltage. This implies that it is possible to regulate the phase current at a desired value to achieve constant torque generation. Two techniques can be employed here: hysteresis current control and pulse-width modulation (PWM) control [6]. Above base speed and in the face of a large back-EMF, it is not possible to achieve the desired current level anymore. The SRG is deemed to operate in single-pulse mode in this case. In this mode the current takes the shape of a single pulse whose characteristics are determined jointly by the time instants at which the phase is switched on and off.

In addition to regulating the current below base speed one may also opt for using the single-pulse mode. This will result in higher phase currents and higher saturation levels, but the switching losses are reduced. Because the single-pulse operation is more efficient than hysteresis and PWM control techniques [14], and because the noise is lower in single-pulse mode compared to the other modes due to reduced switching action [13], the SRG in the

range extender will be operated in single-pulse mode in the entire speed range.

The single-pulse mode is explained with the help of Table 2.1 and Figures 2.2 and 2.5. Let $\theta_{\rm on}$ and $\theta_{\rm off}$ be the electrical rotor angles at which the switches in Figure 2.5 are turned on and off, respectively. Moreover, let $\theta_{\rm cond}$ be the conduction interval that is defined by

$$\theta_{\rm cond} = \theta_{\rm off} - \theta_{\rm on} \tag{2.17}$$

which identifies duration in which the switches remain closed.

At high shaft speeds the back-EMF $u_{\rm e}$ attains large values that cause the phase current $i_{\rm ph}$ to increase slowly. Because of the large time needed to build up the current in the phase, the conduction angle is larger at high speeds than at low speeds. However, once the switches are opened to demagnetize the phase, $i_{\rm ph}$ will continue to increase in the case when $u_{\rm e}$ is larger $U_{\rm DC}$. Since one has no influence on the current once the switches are turned off, one has to properly choose $\theta_{\rm on}$ and $\theta_{\rm off}$ such that the current does not behave in an undesired manner after turn off. This is one major difference between SRGs and SRMs as in SRMs only $\theta_{\rm on}$ is responsible for controlling the peak current [30]. The phase current during one generation cycle at high shaft speeds is shown in Figure 2.6. The different stages are depicted in Figure 2.7.

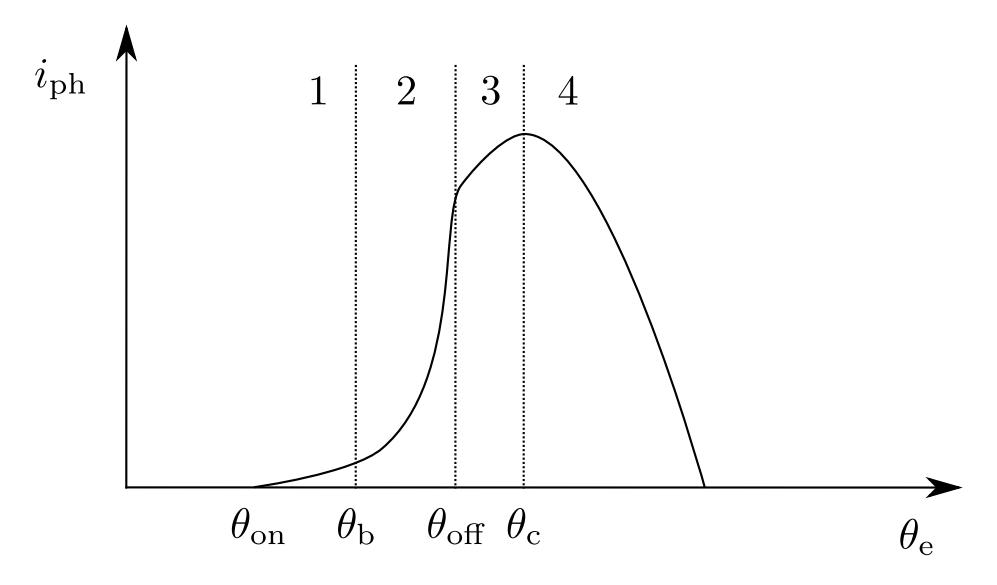


Figure 2.6: Typical Phase Currents at High Shaft Speeds

At low speeds $i_{\rm ph}$ builds up quickly because $u_{\rm e}$ is small. Therefore, small conduction intervals $\theta_{\rm cond}$ are needed to have proper excitation. And once the switches are opened, $i_{\rm ph}$ starts to decrease immediately because $U_{\rm DC}$ is larger than $u_{\rm e}$. A typical phase current waveform at low speeds is shown in Figure 2.8.

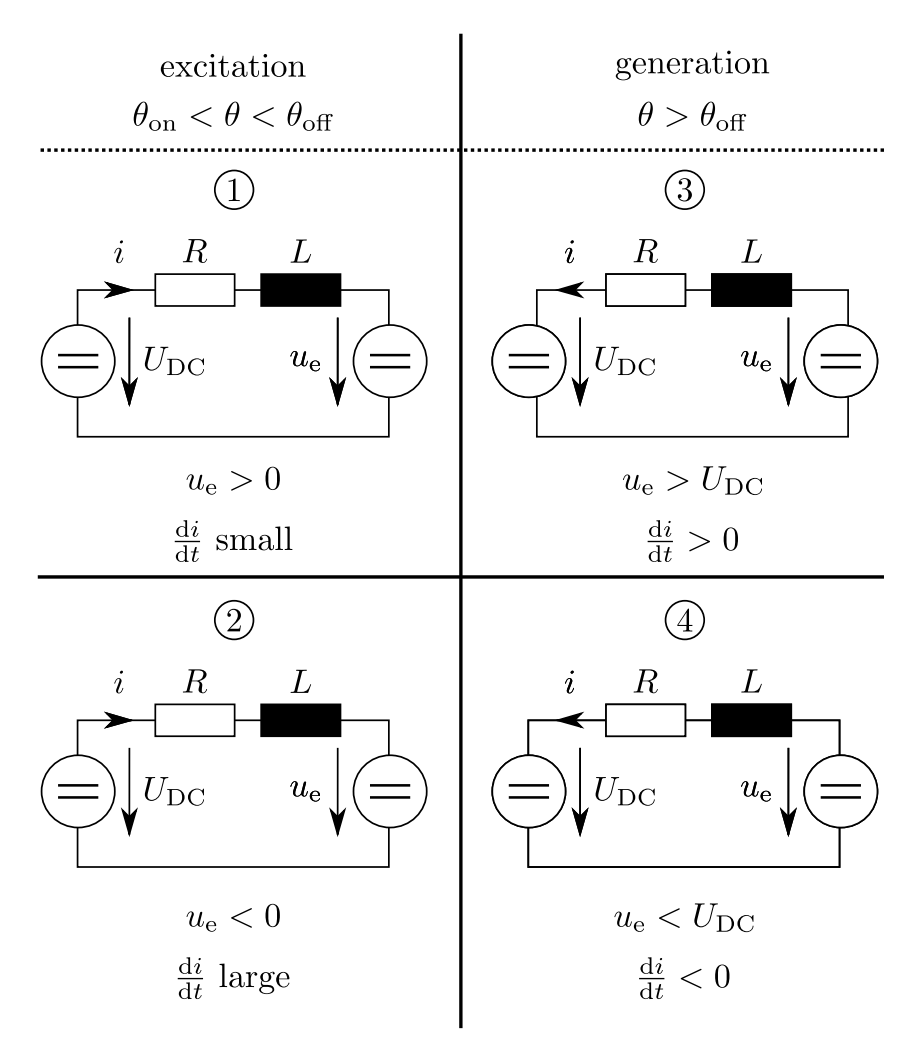


Figure 2.7: Different Stages of an Electrical Cycle

2.2.2.1 Excitation Penalty

Since the SRG excites itself, it is important to minimize the excitation energy as much as possible to achieve a desired generation level [21]. For this purpose a parameter called the excitation penalty ϵ is defined by

$$\epsilon = \frac{I_{\text{exc}}}{I_{\text{gen}}} \tag{2.18}$$

where $I_{\rm exc}$ and $I_{\rm gen}$ are the rms excitation and generation current, respectively. The excitation current is equal to the phase current when the switches in an AHB converter are conducting. Likewise, when the diodes are conducting, the generation current is equal to the phase current. Minimization of ϵ could also be the goal of an optimization process, as it leads to improvement of the power factor [15].

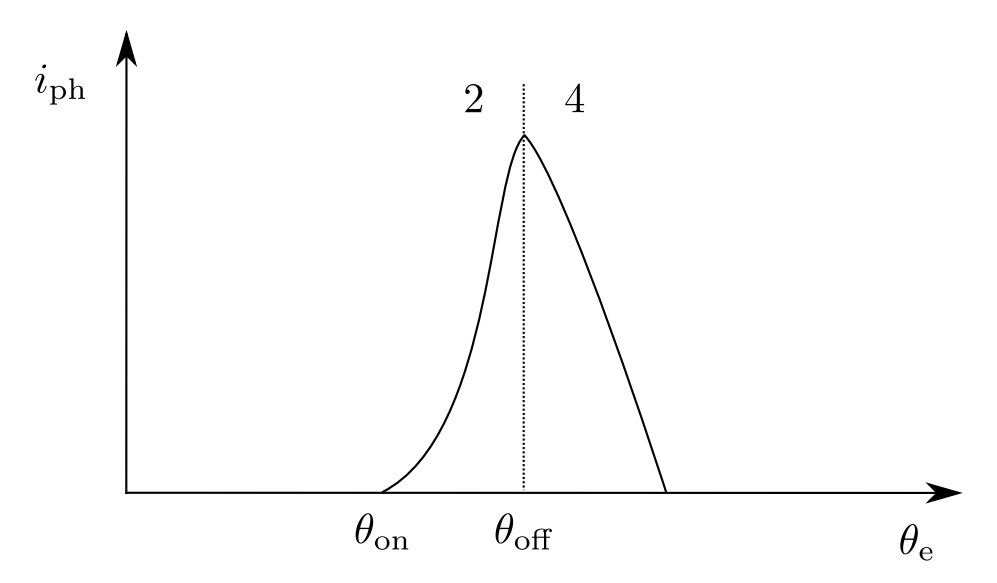


Figure 2.8: Typical Phase Currents at Low Shaft Speed

2.2.3 Multi-phase Machines

The concepts developed for the single-phase SRG are readily applicable to multi-phase SRGs because the phases are electrically and magnetically independent [10]. One has to consider the spatial location of each phase when deciding the relative angle of each phase with respect to the shaft angle. For example in the machine shown in Figure 2.1, there is a difference of 22.5° mechanical between both phases. Therefore, the relative electrical angle θ_e^i of the ith phase is calculated from the shaft angle θ_m by

$$\theta_{\rm e}^{\rm i} = N_r(\theta_{\rm m} - 22.5^{\circ}({\rm i} - 1))$$
 (2.19)

The asymmetric half-bridge (AHB) converter shown in Figure 2.5 can also be used to drive multi-phase SR machines. Shown in Figure 2.9 is a two-phase AHB converter that is compatible with the SR machine in Figure 2.1.

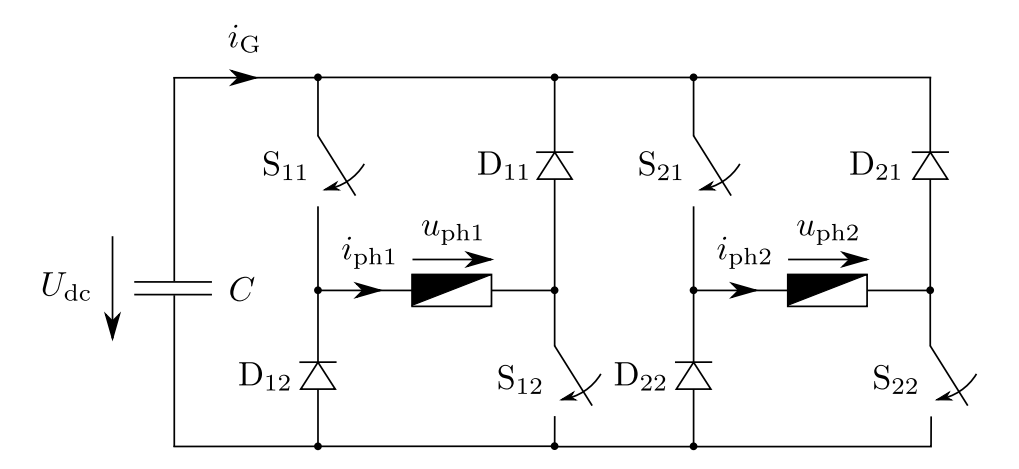


Figure 2.9: Two-phase Asymmetric Half-bridge Converter

To determine the total machine current $i_{\rm G}$, one must know whether each phase is in excitation, demagnetization or free-wheeling. If the variable m represents the state of the phase that is defined as follows

$$m = \begin{cases} 1 & \text{excitation} \\ 0 & \text{free-wheeling} \\ -1 & \text{demagnetization} \end{cases}$$
 (2.20)

then the total machine current is equal to

$$i_{\rm G} = m_1 i_{\rm ph1} + m_2 i_{\rm ph2} + \dots {2.21}$$

In addition, the total machine torque $T_{\rm G}$ is the algebraic sum of each phase torque.

$$T_{\rm G} = T_{\rm ph1} + T_{\rm ph2} + \dots$$
 (2.22)

It is worth to mention that not all SR machine configurations can start from all rotor positions. For example, in the SR machine shown in Figure 2.1, there exists two rotor positions from which the machine cannot start from standstill. Those positions are the aligned position of each phase, as illustrated in Figure 2.1-a for phase 1. For both phases at the two shown positions, $dL/d\theta$ is equal to zero. Hence, torque cannot be generated according to Equation (2.15). To overcome this problem machines with higher phase numbers can be used, but this will be at the expense of higher number of connections and more power electronic devices. Another solution is to use a machine with a stepped gap, in which there will be positive $dL/d\theta$ for at least one phase at any rotor position [21].

2.2.4 Converter Topologies

Switched reluctance machines can operate in motoring or generating modes by energizing the phase in the regions of increasing or decreasing phase inductance, respectively (Equation (2.15)). Since only uni-directional currents are required in both modes, converters used in SR drives are simpler than conventional converters used in AC synchronous and induction drives, which require positive and negative currents to create rotating magnetic fields [10].

So far only the asymmetric half-bridge (AHB) converter (Figure 2.9) has been considered in the analysis of the SR machine. This converter allows simple and independent operation of the phases, and does not permit shoot-through faults since the phase winding is always in series with the two switches. Because this converter contain many devices per phase (two switches and two diodes), variants of this topology exist which have fewer devices per phase [3]. However, this reduction in component count might lead to increased conduction losses or reduced control flexibility [3].

Generally, any SR drives converter must be capable of phase excitation and demagnetization. The major difference that distinguishes existing topologies is the way the magnetic energy is recovered at the end of each electrical cycle [3, 10]. Apart from transferring the

energy to the source as in the AHB converter, the energy could also be transferred to an additional capacitor, to a winding that is closely coupled with the phase winding, or to a resistor [3].

Capacitive-based energy recovery converters transfer the demagnetization energy to a capacitor, causing its voltage to rise beyond the initial voltage, which is the DC-link voltage. Later, this recovered energy will be used to excite the next phase as the capacitor is connected in parallel with the phase. The turn-on time is faster in this case than in AHB converters, because the capacitor voltage is higher than the DC-link voltage.

Magnetic-based energy recovery converters transfer the energy from the phase winding to another winding. This energy could then be transferred to the source or to another phase winding. One disadvantage of such type is the need of snubber circuits because the windings can never be completely magnetically coupled. However, this type allows for higher rates of change in currents because the demagnetization energy is converted to magnetic energy [3].

In contrast to capacitive- and magnetic-based energy recovery converters, dissipative-based converters do not utilize the demagnetization energy but rather let it dissipate in a resistor at the end of the electrical cycle. As a result, the demagnetization energy is converter into thermal energy. This type of converters has low efficiencies, but requires fewer components than capacitive- or magnetic-based converters. Other SR drive converter topologies exist and the reader is referred to [3] for more details.

2.2.5 Losses in Switched Reluctance Drive Systems

Because the rotor does not carry any current, a SR machine is more efficient than an induction machine. However, the high peak currents and high frequency render power electronic (PE) converters in SR drive systems less efficient than those in induction and synchronous machines drive systems [33]. Losses in a SR drive system are generated in the phase windings, in the iron core of the machine, and in the PE converter.

2.2.5.1 Copper Losses

The phase resistance R_{ph} dissipates power due to the flow of the phase current i_{ph} in the copper material. This power is directly proportional to R_{ph} and to the square of the rms phase current $I_{ph,rms}$. The average copper loss dissipation in one phase $P_{\text{copper},ph}$ is

$$P_{\text{copper,ph}} = \overline{p_{\text{copper,ph}}} = \frac{1}{T} \int_{0}^{T} p_{\text{copper,ph}} dt = \frac{1}{T} \int_{0}^{T} R_{\text{ph}} i_{\text{ph}}^{2} dt = R_{\text{ph}} I_{\text{ph,rms}}^{2}$$
(2.23)

The total copper losses P_{copper} in a SR machine are sum of those in every phase.

$$P_{\text{copper}} = P_{\text{copper,ph1}} + P_{\text{copper,ph2}} + \dots \tag{2.24}$$

2.2.5.2 Iron Losses

Losses in ferrite material are generated when a time-changing flux ϕ is applied to the material. These losses include hysteresis and core losses, and are calculated per volume using Steinmitz equation for sinusoidal flux waveforms. The Steinmitz equation is

$$p_{\rm Fe} = k f^{\alpha} \hat{B}^{\beta} \tag{2.25}$$

where the parameters α , β and k are known as Steinmitz parameters and \hat{B} is the peak flux density. The flux density B is equal to

$$B = \frac{\phi}{A} \tag{2.26}$$

where ϕ is the flux that travels through area A. The flux ϕ is related to the flux-linkage ψ by the number of winding turns w.

$$\phi = \frac{\psi}{w} \tag{2.27}$$

Because flux waveforms in SR machine are not sinusoidal [21], Equation (2.25) cannot be applied to calculate the iron losses in SR machines. For this reason there has been many attempts to adapt the Steinmitz equation for non-sinusoidal flux waveforms. The most successful method so far [7] is the improved Generalized Steinmitz equation (iGSE) developed by [32]. The iGSE relies on the peak-to-peak flux density, and makes use of the same parameters used in Equation (2.25).

$$p_{\rm Fe} = \frac{1}{T} \int_0^T k_{\rm i} \left| \frac{\mathrm{d}B}{\mathrm{d}t} \right|^{\alpha} (\Delta B)^{\alpha - \beta} \mathrm{d}t$$
 (2.28)

where

$$k_{\rm i} = \frac{k}{(2\pi)^{\alpha-1} \int_0^{2\pi} |\cos\theta| 2^{\beta-\alpha} d\theta}$$
 (2.29)

The Steinmitz parameters can be calculated from the loss curves and data fitting. Manufacturers of ferrite material usually provide the loss curves for sinusoidal flux densities at various frequencies.

A recursive algorithm that applies Equation (2.28) by splitting flux-waveforms into major and minor loops has been developed by [32] and is made available on the internet. The algorithm is implemented as a Matlab function that accepts flux density waveform and Steinmitz parameters as inputs, and returns the loss per volume.

When it comes to iron loss calculation in SR machines, the challenge is the determination of the flux in the different machine parts. Since most of the losses occur in the rotor [17], it is difficult to estimate the flux in the different rotor sections since they are not only a function of time but also depend on the rotor position. Search coils could be used to measure the flux in different machine sections [7], but this method needs experimental setups and, therefore, not suitable at early design stages when the system has not been implemented yet. Another method is to use finite-element simulation tools. However, these tools are also not practical for they require a lot of time [7]. To solve these problems, the flux in the different machine sections could be constructed from the phase flux-linkages that are readily available by Equation (2.3) [17]. This method assumes that the entire phase flux flows in the core, so leakage fluxes are totally neglected. Consequently, this method has the least accuracy. Nonetheless, it provides fast results, and can, therefore, be applied in mass simulations, optimization processes and online control systems.

2.2.5.3 Friction Losses

Friction losses include those due to the friction of the bearings and due to the air friction. They are a function of the cubic of the speed [8].

2.2.5.4 Converter Losses

The average converter losses P_{conv} include the conduction losses P_{cond} and the switching losses P_{switch} .

Conduction Losses

Consider Figure 2.10, which shows a one-phase AHB converter with voltage drops across the devices. The product of the current through a semiconducting device and the voltage drop across it constitute the conduction loss dissipated by the device. In a one-phase asymmetric half-bridge (AHB) converter, the phase current $i_{\rm ph}$ always flows through two devices at the same time. Therefore, conduction losses in a one-phase AHB converter is the product of the $i_{\rm ph}$ and the total voltage drop of both devices $U_{\rm n}$.

$$P_{\text{cond,ph}} = \overline{p_{\text{cond,ph}}} = \frac{1}{T} \int_{0}^{T} p_{\text{cond,ph}} dt = \frac{1}{T} \int_{0}^{T} U_{\text{n}} i_{\text{ph}} dt$$
 (2.30)

If each switch has a voltage drop $U_{\rm nS}$ and each diode has a voltage drop $U_{\rm nD}$, then $U_{\rm n}$ is equal to

$$U_{\rm n} = \begin{cases} 2U_{\rm nS} & S_1 \& S_2 \text{ conducting} \\ 2U_{\rm nD} & D_1 \& D_2 \text{ conducting} \\ U_{\rm nS} + U_{\rm nD} & (S_1 \& D_1) \parallel (S_2 \& D_2) \text{ conducting} \end{cases}$$
(2.31)

The total conduction losses P_{conv} of a multi-phase converter is the sum of conduction losses in all phases.

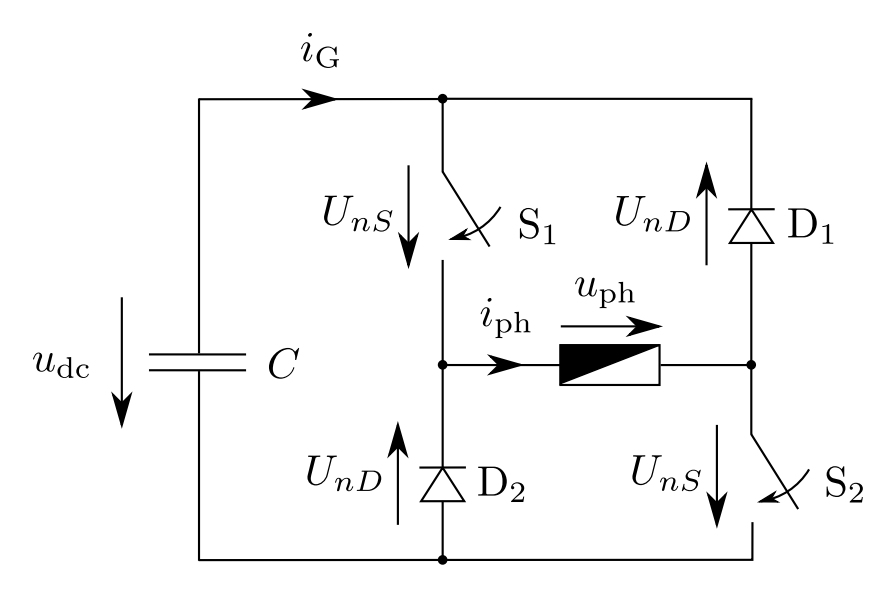


Figure 2.10: One-phase Asymmetric Half-bridge Converter with Realistic Devices

$$P_{\text{cond}} = P_{\text{cond,ph1}} + P_{\text{cond,ph2}} + \dots \tag{2.32}$$

Switching Losses

The act of switching a semiconductor device on or off generates losses because the current through the device and the voltage across it cannot change instantaneously [22]. Figure 2.11 shows the current through the switches and diodes during one electrical cycle. When the switches in the AHB converter are turned on, the phase current starts to build up from zero. This means that the turn-on losses of the switches are zero. The switches, however, are turned off while the phase current is flowing through them. Hence, turn-off losses are generated in the switches. Once the switches are turned off the current commutates to the diodes. The diodes behave like ideal switches at turn-on [22]. Hence, the diodes turn-on losses are neglected. And since the diodes carry the current until it becomes zero, there are no reverse recovery losses generated by the diodes because they are not forced into reverse bias while they are carrying current. As a result, only the turn-off losses of switches are considered in the simulations.

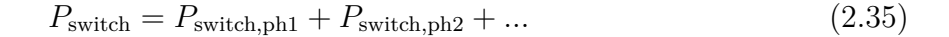
Manufacturers of power electronic switches provide datasheets that include the turn-off energy E_{off} dissipated by the switch as a function of current at the moment of turn-off. To get the dissipated power, E_{off} is multiplied by the switching frequency of the device. In a one-phase AHB converter there are two switches that turn off once every electrical cycle. Therefore, the switching frequency is equal to the electrical frequency f_{e} . For a constant shaft speed n and using Equation (2.2), f_{e} is equal to

$$f_{\rm e} = N_{\rm r} \frac{n}{60} \tag{2.33}$$

The switching losses in one phase are therefore

$$P_{\text{switch,ph}} = 2f_{\text{e}}E_{\text{off}}$$
 (2.34)

To obtain the total switching losses in multi-phase AHB converters, the switching losses in all phases are summed.



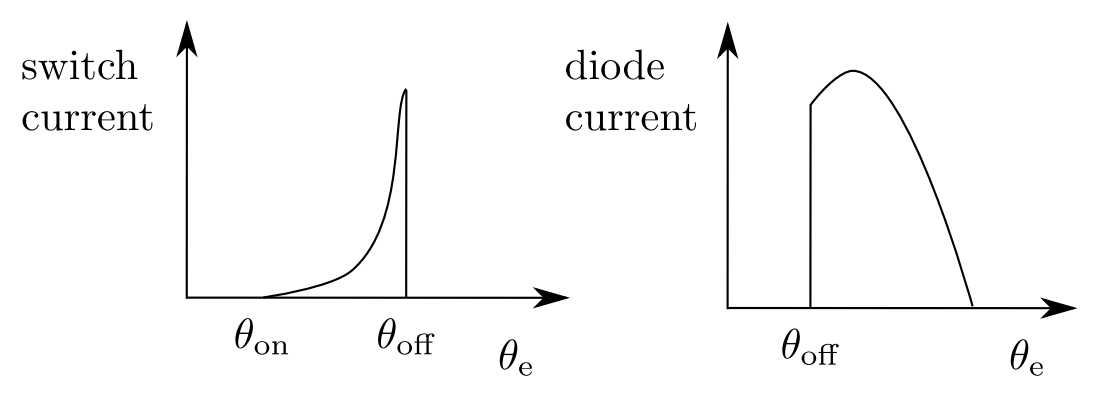


Figure 2.11: Switch and Diode Currents during One Electrical Cycle

2.2.6 Acoustic Noise in Switched Reluctance Drive Systems

One major disadvantage of SR machines are their electromagnetic noise, which are generated due to the operating principles on which SR machines work on. Because a SR machine has a doubly-salient structure with concentrated windings, strong radial forces are generated whenever a rotor tooth comes into proximity with a stator tooth [13]. In addition, the phase currents in a SR machine are not sinusoidal but look like pulses that include many harmonics. These harmonics are also existent in the radial forces, and so they contribute to the acoustic behavior of the SR machine [13].

In a SR machine with linear magnetic characteristics, the radial stator tooth force F is equal to

$$F = \frac{L(\theta)i^2}{2l_{\text{gap}}} \tag{2.36}$$

where L is the phase inductance, θ is the rotor position, i is the phase current, and $l_{\rm gap}$ is the air gap length between a stator and rotor tooth. From this equation it is understandable that the radial force, and hence acoustic noise level, is greater near the aligned position and smaller near the unaligned position. Therefore, an acoustically-optimized control strategy would change the turn-on angles such that the phases conduct near the aligned position. Based on this principle, the early single-pulse control strategy has been developed and applied to switched reluctance motors [13]. This strategy, however, creates higher torque ripples and degrades efficiency.

2.2.7 Control of Switched Reluctance Generators

The existing SRG control strategies are surveyed next. Attention has been put on strategies that control the SRG in single-pulse mode. Some strategies make use of open control systems, while others use closed-loop techniques to increase reliability and improve the performance.

In [5] a state-feed back controller is implemented to control the DC-link voltage and minimize the voltage ripple. The system resembles the range extender system except for the load where a DC current source is used instead of a DC voltage source. Maps are first generated for the DC-link current as a function of the turn-on and conduction angles with the DC-link voltage as a third parameter. Then these maps are used in the control system in which the controller output is the required average DC-link current. Next, for a given turn-on angle and DC-link voltage and DC-link current, the conduction angle is determined from the maps.

Also in [20] maps are created for the generated power as a function of turn-on and conduction angles, and shaft speed. From these maps it has been observed that there are many combinations of control angles that results in the same power at a specific speed. It is decided that the combinations that lead to minimum rms current are chosen because minimization of rms current implies maximizing efficiency. Next these combinations are used in an open-loop control system to control the SRG. The controller simply determines by look-up tables the appropriate angles depending on the power and speed.

In [30] it is suggested that if the SRG is supplying a system with a stiff voltage source, like the batteries in automotive applications, then it is not necessary to control the power by a closed-loop system because the operation cannot become unstable. In addition, minimization of rms current is also used in efficiency optimization since it leads to minimum copper and conduction losses, and minimum peak flux and, hence, minimum iron losses. The control strategy resembles the one presented in [20].

An open- and a closed-loop control systems are used in [28] to control the SRG. It is claimed that for every power and speed values, there exists an optimum turn-off angle that corresponds to maximum system efficiency. Consequently, this angle is determined by a look-up table depending on the speed and power. The turn-on angle is then controlled by a closed-loop controller to achieve the desired power. Closed-loop control is suggested to be important for the operation of the SRG because it accounts for any differences between the simulation model and the real system. It is also shown that small changes in the control angles do not lead to large variations in efficiency.

Since current control is lost in single-pulse mode at high speeds (Section 2.2.2), the authors in [14] propose flux control for optimum operation of the SRG in this case. A closed-loop controller is implemented to regulate the DC-link voltage at maximum efficiency. The controller uses information of the shaft speed and DC-link voltage error to determine the optimum control angles. Some parameters used in the controller are determined experimentally, which makes this method not suitable at early design stages.

Contrary to the claims proposed in [20, 30] that minimizing rms current means maximizing efficiency, it is shown in [12] that this is not the case. In fact, it is shown through simulations that the turn-on angles for maximum efficiency are larger than those for minimum rms current. Furthermore, conduction angles that correspond to better efficiencies are smaller than those associated with minimum rms currents.

2.3 Genetic Algorithms

A genetic algorithm (GA) is an optimization and search tool that is inspired by the natural selection mechanism, where the "member" with the best qualities survives the current generation, makes it to the next generation, and produce offspring that carry some of its qualities [16]. A GA can be used, for example, in the optimization of the control parameters of a SR drive system according to certain criteria (see Section 4.1).

Each member in this process is represented by a chromosome that is a string of bits, and these bits carry information that tells how good or fit the chromosome is. In other words, the information stored in the chromosome yields a value called the "fitness value", and the higher the fitness value, the better the chromosome is.

A GA process starts by a group of chromosomes called a "population", which could be randomly generated or user-defined. The fitness value of each member is evaluated to see how good each chromosome is. Based on the calculated fitness values, the better chromosomes will then be chosen as parents to produce the offspring for the next generation. Offspring are created using two operations called "crossover" and "mutation", which are key features in the way genetic algorithms work. After the offspring have been created, they are introduced into the population to replace some or all the previous members. After that the process starts all over from the beginning by evaluating each chromosome, determining the new parents, creating another generation of offspring, replacing the old generation and so on. The process keeps on repeating until it is terminated by one of many criteria. For example, it can be stopped after a maximum number of generations have been produced, or until a pre-defined fitness value has been achieved. The three major operations in a GA algorithm, namely parent selection, offspring creation, and replacement are explained next.

2.3.1 Parent Selection

Parent selection can be accomplished by many schemes. The most popular one is the Roulette Wheel Selection scheme [16]. In this scheme, the higher the fitness value of a chromosome, the more likely it will be selected as a parent. To demonstrate how this scheme works consider the population shown in Figure 2.12, which is comprised of 5 members whose fitness are directly proportional to the portion of the area they occupy. If this population rotates like a roulette wheel, then it is most likely to stop at member number 2, which spans the largest area of the population. This is how the roulette wheel selection schemes works. The

member with highest fitness value will most like be chosen as a parent to create an offspring.

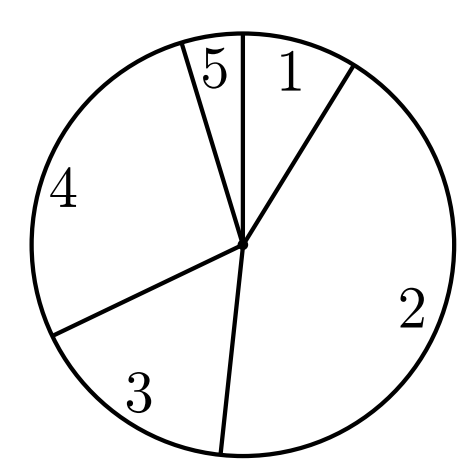


Figure 2.12: Roulette Wheel Parent Selection Scheme

2.3.2 Offspring Creation

Offspring are created using two operations, which are crossover and mutation. They can be accomplished by different ways. The decision to use which method is problem dependant [16]. They are introduced next.

2.3.2.1 Crossover

Crossover works by swapping parts of two chromosomes. There are many types of crossover. One type is called the one-point crossover. In this type a random point is chosen a long the length of the chromosome, and parts of the two chromosomes beyond this point are swapped. Another type is called the multi-point crossover, in which more than one portion of two chromosomes are swapped. Furthermore, the uniform crossover can be applied. In this type a randomly-generated mask is created, whose length is equal to the chromosomes length. The bits of the chromosomes are swapped if the corresponding bit in the mask is "1", and left intact if the bit is "0". Figure 2.13 shows the different types of crossover.

The probability of crossover determines how often the swapping occurs. For example, in the uniform crossover, having a "1" in the mask does not automatically imply that the corresponding bits of the parents are exchanged. The exchange rather has a probability of occurrence.

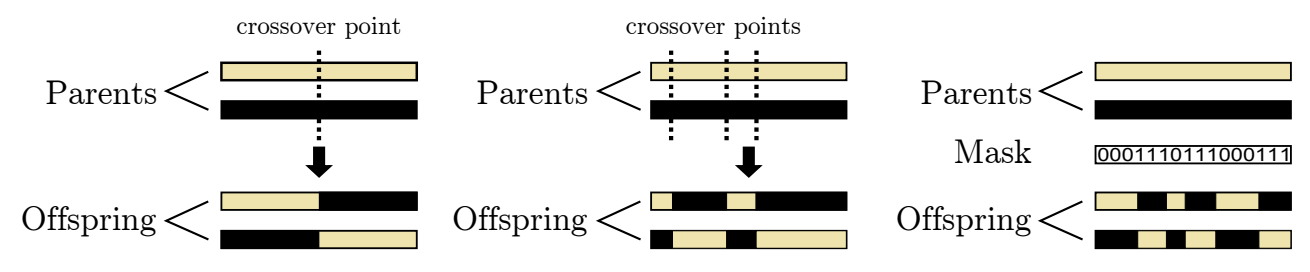


Figure 2.13: Crossover

2.3.2.2 Mutation

The other GA process that has an impact on the newly-created offspring is mutation. Unlike crossover, mutation operates on a single chromosome. In mutation, one of the bits of the chromosome is randomly chosen, and its value is toggled. Mutation is depicted in Figure 2.14. Other mutation mechanisms sets or resets the bit instead of toggling its value.

Like crossover, there is a probability of occurrence of mutation. This means that not all offspring experience mutation. The probability value is small so as not to increase the randomness in the process [16].



Figure 2.14: Mutation

2.3.3 Replacement

The offspring are created to replace the previous generation. Several strategies can be adopted. One strategy is to let the offspring replace the entire old population. Another is to select a few of the fittest old chromosomes and have them in the next generation. One can also have the parents be replaced by the offspring directly [16].

A model of the range extender system is presented in this chapter. The model is used in a MATLAB/Simulink environment to carry out simulations and optimization processes. With the help of mathematical formulation and generic block diagrams, each main part of the range extender system shown in Figure 3.1 will be modelled separately. Afterwards, the power flow and losses in the system are determined to asses the performance and efficiency.

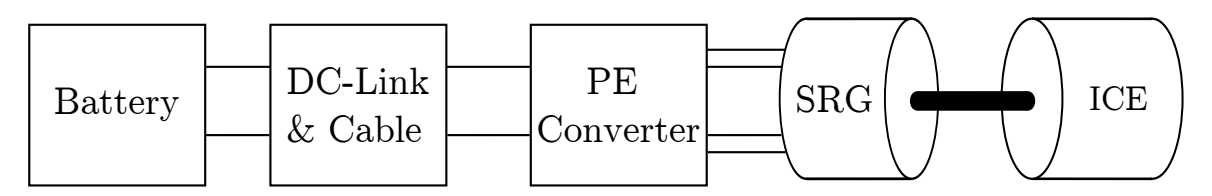


Figure 3.1: Overview of Range Extender System

3.1 Switched Reluctance Generator

The switched reluctance generator (SRG) considered in this work is a 2-phase SRG with an asymmetric rotor. It has 8 stator teeth and 4 rotor teeth. A cross sectional view of the SRG is shown in Figure 3.2.



Figure 3.2: Cross-sectional view of the SRG used in the Model

A Simulink model of a SRG has been developed at ISEA that accepts the phase voltage $u_{\rm ph}$ and the mechanical angle $\theta_{\rm m}$ as inputs, and produces the phase current $i_{\rm ph}$, the phase torque $T_{\rm ph}$ and the stator tooth radial force F as outputs. An overview of a one-phase SRG model is shown in Figure 3.3.

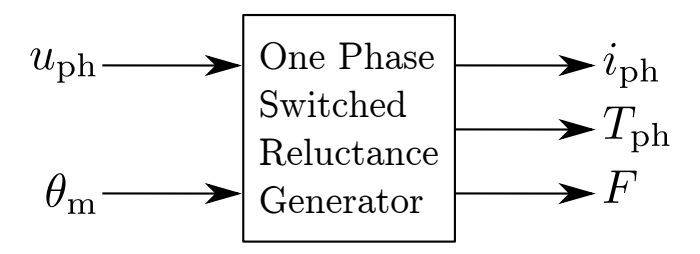


Figure 3.3: Overview of a One-phase SRG Model

Using the finite-element simulation software FLUX2D, the magnetization characteristics $\psi(\Theta, \theta_e)$ can be obtained for discrete values of Θ and θ_e . However, for modeling purposes the inverse magnetization characteristics $\Theta(\psi, \theta_e)$ are needed, which are obtained by rearranging the $\psi(\Theta, \theta_e)$ matrix.

$$\Theta = f(\phi, \theta_{\rm e}) \tag{3.1}$$

The phase torque $T_{\rm ph}$ and tooth radial force F can also be calculated using FLUX2D depending on Θ and $\theta_{\rm e}$.

$$T_{\rm ph} = f(\Theta, \theta_{\rm e}) \tag{3.2}$$

$$F = f(\Theta, \theta_{\rm e}) \tag{3.3}$$

In Simulink Θ , $T_{\rm ph}$ and F are implemented by two-dimensional lookup tables. These tables are loaded first with two input vectors of equally-spaced values and one output matrix. For any set of inputs, an output value is calculated by interpolating the output matrix. Some of the FLUX2D results are shown in Figures 3.4 to 3.6.

A block diagram of the SRG model implementation based on Equations (2.3), (2.19), (2.27) and (3.1) to (3.3) is illustrated in Figure 3.7. Although the diagram depicts the implementation for one phase, it is identical for the other phases except for the difference in the $\theta_{\rm m}$ to $\theta_{\rm e}$ converter as demonstrated in Equation (2.2). The generator torque $T_{\rm G}$ and current $i_{\rm G}$ are obtained using Equations (2.20) to (2.22).

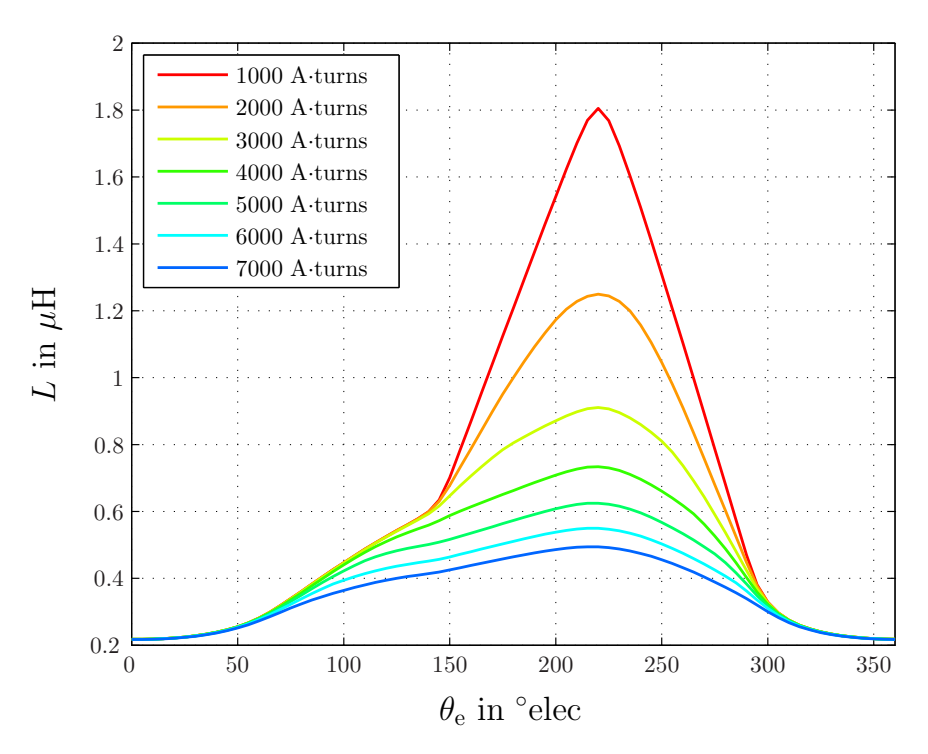


Figure 3.4: Phase Inductance as a Function of Electrical Angle and MMF

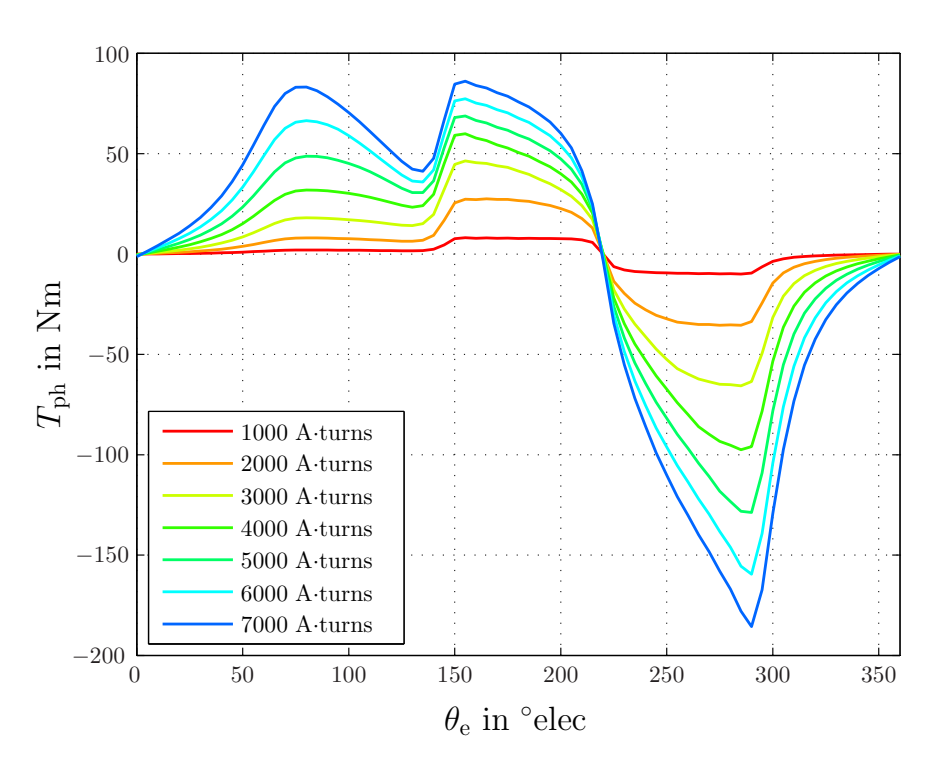


Figure 3.5: Phase Torque as a Function of Electrical Angle and MMF

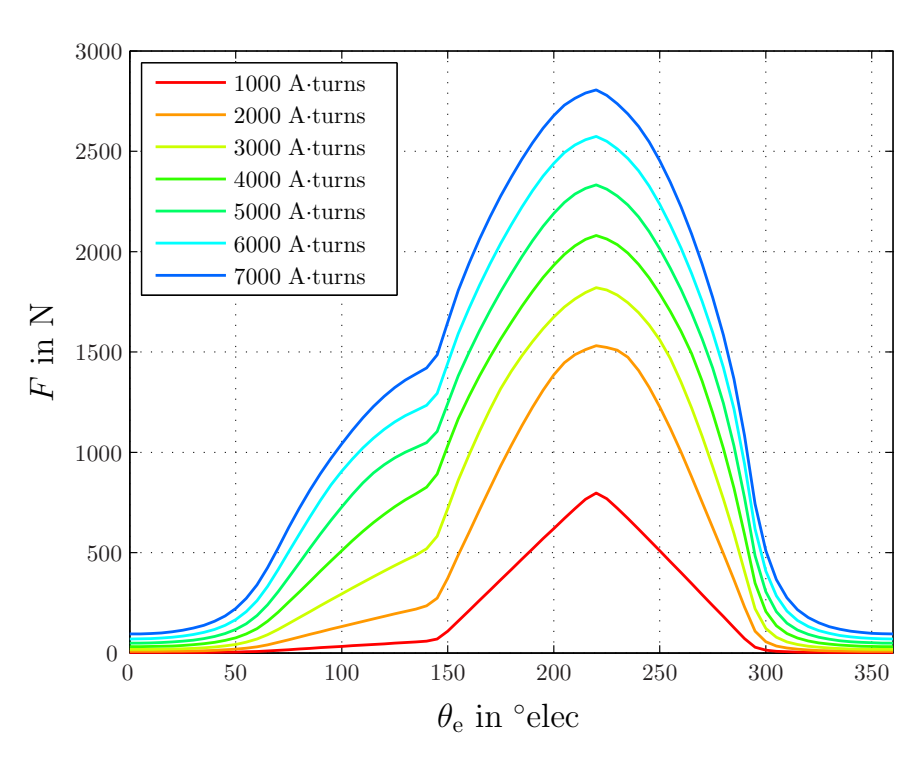


Figure 3.6: Tooth Radial Force as a Function of Electrical Angle and MMF

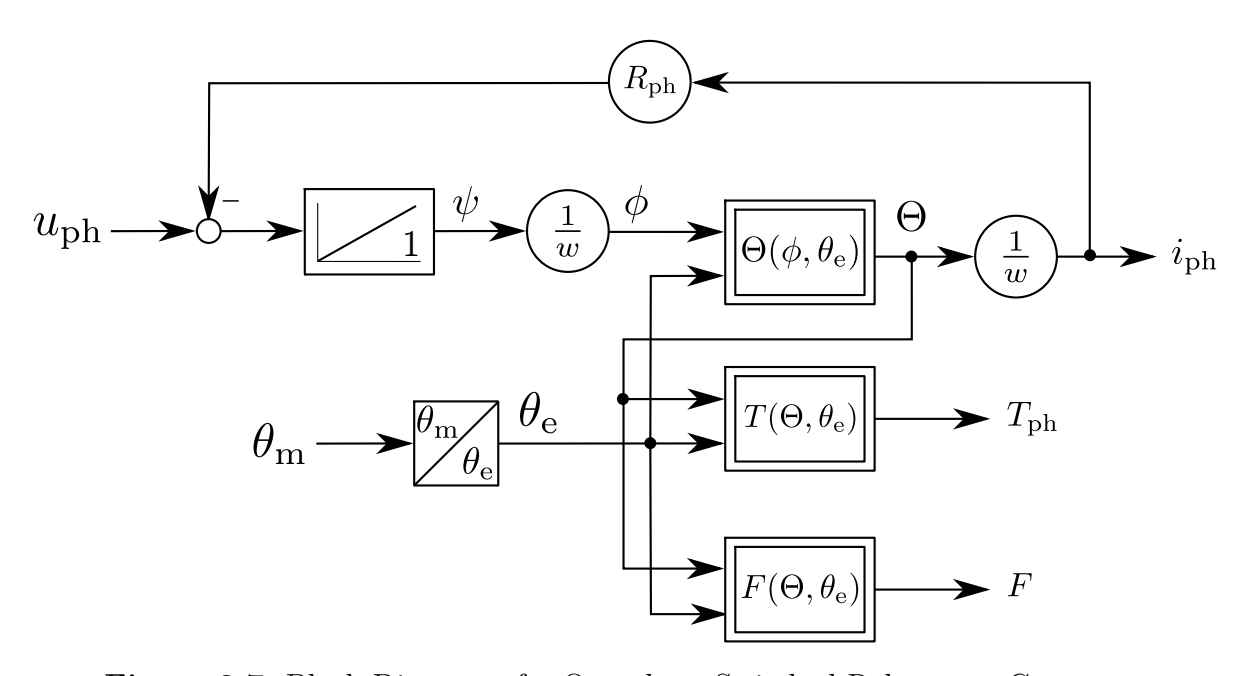


Figure 3.7: Block Diagram of a One-phase Switched Reluctance Generator

3.2 Power Electronics Converter

An Asymmetric Half-bridge topology is chosen as the power electronic (PE) converter. The converter model accepts the DC-link voltage $u_{\rm C}$, the shaft angle $\theta_{\rm m}$, the turn-on angle $\theta_{\rm on}$ and the turn-off angle $\theta_{\rm off}$ as inputs, and produces the phase voltage $u_{\rm ph}$ as an output. On overview of the block-diagram implementation is shown Figure 3.8, and a one-phase asymmetric half-bridge converter is shown in Figure 2.5 on page 8.

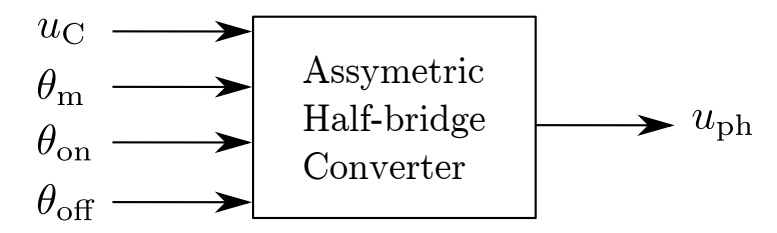


Figure 3.8: Overview of Power Electronic Converter Model

In an AHB converter the switches must be rated for the DC-link voltage, which is 300 V. For a 20-kW system, the average current amounts to 70 A. These specifications are too high for power MOSFETS to meet. Consequently, IGBTs will be used in the PE converter. In particular, the SEMiX 2s modules by Semikron are used. Each module contains an IGBT with an inverse diode in addition to a free-wheeling diode. More details can be found in [26, 27].

The operation of the asymmetric half-bridge topology with ideal semiconductor devices has been explained in Chapter 2. Now the devices are assumed to be more realistic with a voltage drop appearing across each switch (U_{nT}) and each diode (U_{nD}) . This implies that u_{ph} is no longer equals to u_{C} in magnitude due to the presence of U_{nT} and U_{nD} . In this case,

$$u_{\rm ph} = \begin{cases} u_{\rm C} - 2U_{\rm nT} & T_1 \& T_2 \text{ conducting} \\ -U_{\rm nT} - U_{\rm nD} & (T_1 \& D_1) \parallel (T_2 \& D_2) \text{ conducting} \\ -u_{\rm C} - 2U_{\rm nD} & D_1 \& D_2 \text{ conducting} \end{cases}$$
(3.4)

Since the voltage drop across the devices does not change much with respect to current, and since their values are very small compared to the DC-link voltage, constant values are used for $U_{\rm nT}$ and $U_{\rm nD}$. Values of 0.9 V and 1 V are assigned to $U_{\rm nT}$ and $U_{\rm nD}$, respectively [26, 27].

3.3 DC-link

The DC-link comprises a capacitance, and is connected to the battery through a cable. The cable is represented by series combination of a resistance and an inductance. A circuit diagram is shown in Figure 3.9.

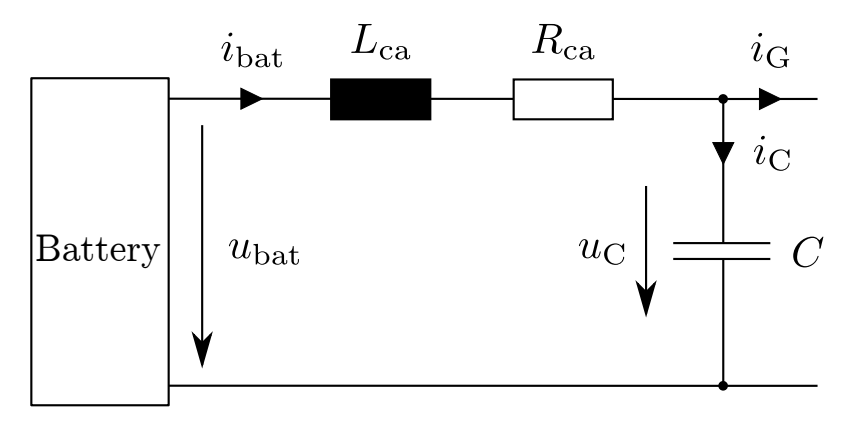


Figure 3.9: DC-link Circuit Diagram

The DC-link is a second-order system. To model such system two differential equations are needed. Applying Kirchhoff's Voltage and Current Laws results in the following set of differential equations.

$$u_{\text{bat}} = L_{\text{ca}} \frac{\mathrm{d}i_{\text{bat}}}{\mathrm{d}t} + R_{\text{ca}}i_{\text{bat}} + u_{\mathrm{C}}$$
(3.5)

$$i_{\text{bat}} - i_{\text{G}} = i_{\text{C}} = C \frac{\mathrm{d}u_{\text{C}}}{\mathrm{d}t} \tag{3.6}$$

A block diagram of the DC-link is shown in Figure 3.10. Note that the battery current i_{bat} is an output because it is needed to determine the battery terminal voltage. Further details are explained in Section 3.4.

A starting value of 1 mF is assumed for the capacitance. The cable inductance varies between 1 and 5 μ H. Thus, an intermediate value of 3 μ H is assumed. The cable resistance is equal to 1 m Ω , which is accurate enough for short cables.

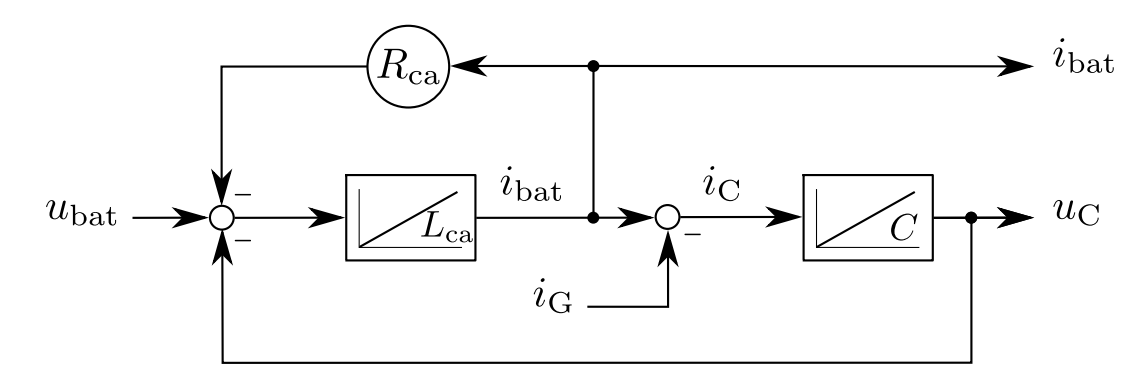


Figure 3.10: Block Diagram of the DC-link

3.4 Battery

To study the charging performance of the range extender a battery model is used. The input to the battery model is the battery current i_{bat} , and the output is the battery terminal voltage u_{bat} . Two battery models are used in this work: a real battery model and an ideal battery model. Both models are explained in the following subsections.



Figure 3.11: Overview of Battery Model

3.4.1 Real Battery Model

A model of a LiFePO₄ battery pack is used in investigating the performance of the range extender when connected to a real battery. This model has been used in implementing an operation strategy for a range extender depending on the driving range, battery power and driving profile [25]. The model is a series and parallel connections of LiFePO₄ cells, and permits the variation of the number of series cells and parallel branches in order to meet the capacity and voltage requirements. A list of the important parameters of the cell is given in Table 3.1.

Table 3.1: Parameters of LiFePO₄ Cell by A123 Systems [1]

Data	Value
Nominal Voltage	3.3 V
Nominal Capacity	1.1 Ah
Recommended standard charge method	1.5A to $3.6V$ CCCV, 45 mins
Recommended fast charge method	5A to 3.6V CCCV, 15 mins
Voltage Limits at 25°C	2 - 3.6 V

To size the battery pack, i.e. determine the number of cells in series and the number of parallel branches, the voltage and capacity must be determined first. The nominal voltage of the battery is 300 V. Hence, the number of cells that have to be connected in series is

$$n_{\text{series}} \ge \frac{U_{\text{bat}}}{U_{\text{cell}}} = \frac{300 \,\text{V}}{3.3 \,\text{V}} \simeq 91$$
 (3.7)

The number of parallel branches is determined from the desired capacity of the battery pack and the capacity of one branch.

$$E_{\text{branch}} = n_{\text{series}} \cdot U_{\text{cell}} \cdot E_{\text{cell}} = 330.33 \,\text{Wh}$$
 (3.8)

A capacity of 27 kW is assumed for the battery pack. Therefore, the minimum number of required parallel branches is

$$n_{\text{parallel}} \ge \frac{E_{\text{bat}}}{E_{\text{branch}}} = \frac{27 \,\text{kWh}}{330.33 \,\text{Wh}} \simeq 82$$
 (3.9)

The battery cell model is in fact an electrical model consisting of a DC source, a series resistor and a parallel combination of a resistor and a capacitor. Each of these components has values that depend on the state of charge (SOC), and are determined by electrochemical impedance spectroscopy [4]. Impedance-based models provide enough accuracy for simulation of batteries, and can be adapted to any battery technology [4]. The electrical model of a battery cell is shown in Figure 3.12.

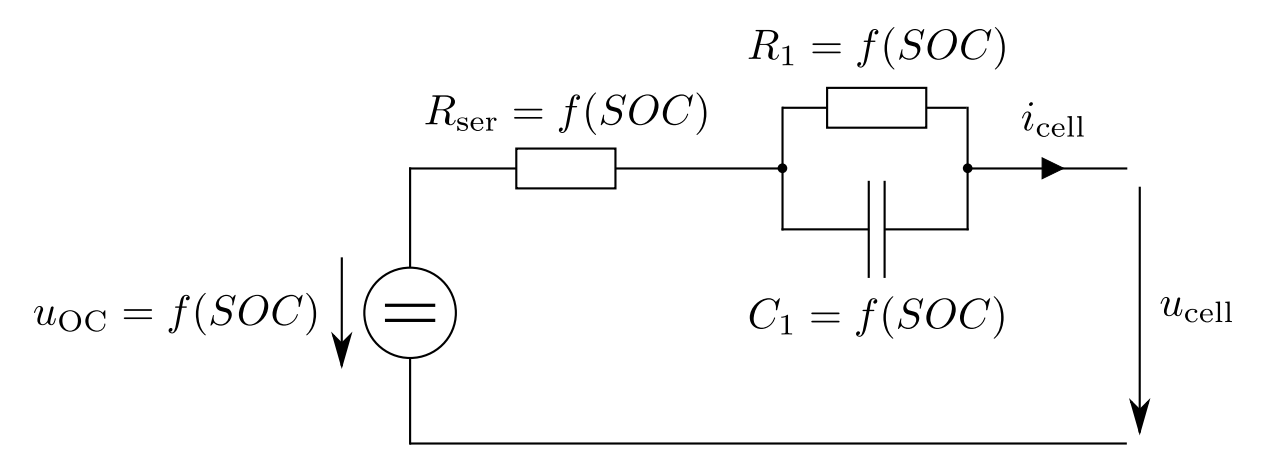


Figure 3.12: Electrical Model of a Battery Cell

3.4.2 Ideal Battery Model

An ideal battery model will be used initially in the optimization process. The reason for this is to avoid having a stiff design for a specific battery technology. As shown in Figure 3.13, this model consists of an ideal DC voltage source and a series resistor.

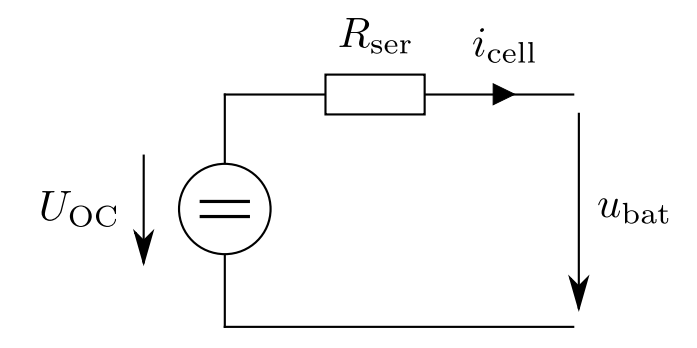


Figure 3.13: Electrical Model of an Ideal Battery

The open-circuit voltage $U_{\rm OC}$ is 300 V and the series resistance $R_{\rm ser}$ is 50 m Ω , which is close to the series resistance of the Thevenin equivalent of the battery pack after neglecting the capacitive element in the cell model.

3.5 Internal Combustion Engine

A four-stroke, one-cylinder internal combustion engine (ICE) acts as a prime mover for the SRG. The torque and power capability of the ICE are tabulated in Table 3.2.

ac and I ower capability of the internal ex						
	Speed in rpm	Torque in Nm	Power in kW			
	2000	25.4	5.3			
•	2500	26.6	6.9			
	3000	24.8	7.8			
•	3500	24.9	9.7			
	4000	26.1	11.0			
	4500	25.9	12.2			
	5000	26.6	13.9			
	5500	27.8	16.0			
	6000	30.9	19.4			
	6250	30.7	20.1			
	6500	30.5	20.8			
	6750	30.8	21.8			
	7000	31.3	23.0			
	7250	31.4	23.8			
	7500	30.5	24.0			
	7750	30.0	24.3			
	8000	29.3	24.5			
	8250	28.7	24.8			
	8500	28.0	25.0			

Table 3.2: Torque and Power Capability of the Internal Combustion Engine

A Simulink model is implemented to estimate the instantaneous engine torque T_E based on the crankshaft angle γ_{cs} and the shaft speed n. Figure 3.14 shows an overview of the implementation in Simulink.

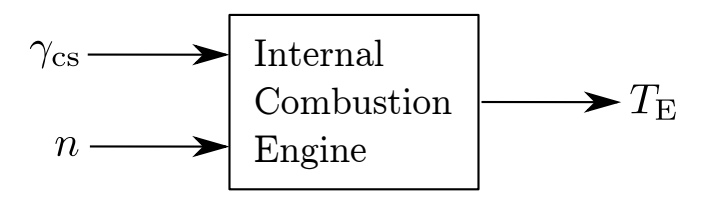


Figure 3.14: Internal Combustion Engine Model

The ICE instantaneous torque $T_{\rm E}$ can be obtained using empirical formulas [19]. Such formulas are not available at this early stage of system design. Therefore, $T_{\rm E}$ is approximated

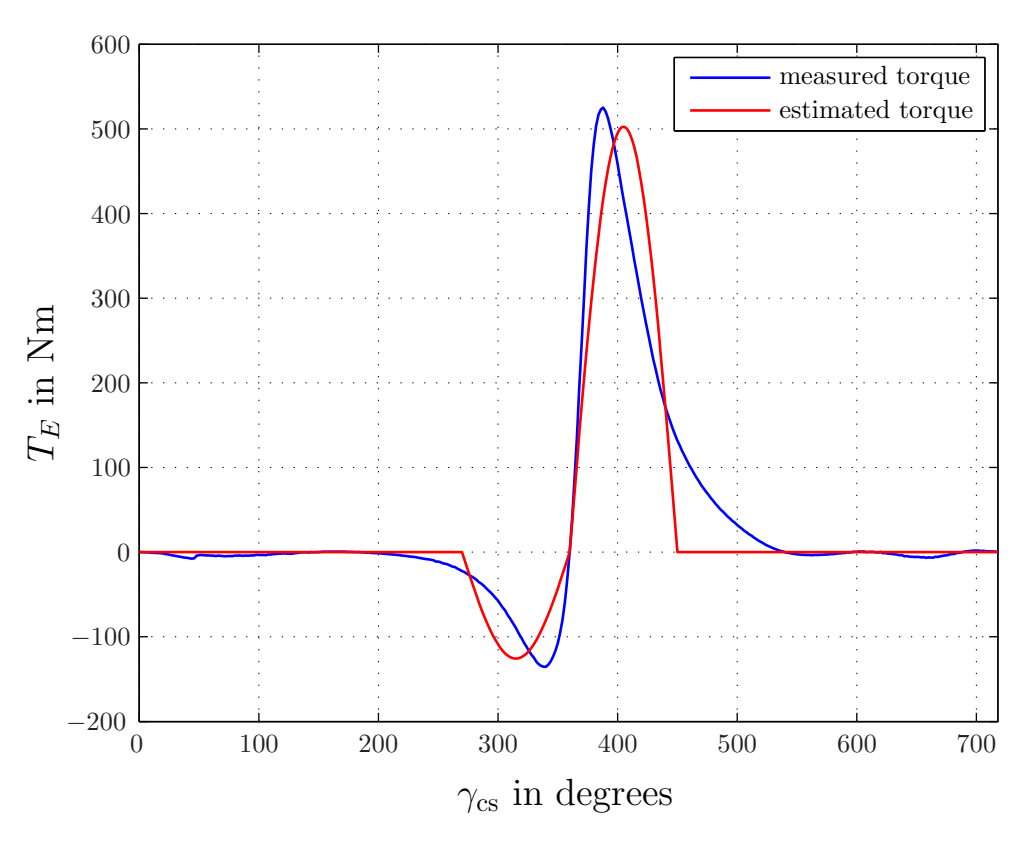


Figure 3.15: Measured and Estimated Engine Torque at 7750 rpm

using two half sine waves. Figure 3.15 shows the measure $T_{\rm E}$ at 7750 rpm as provided by the project partner (blue curve), and the estimated $T_{\rm E}$ (red curve) with respect to $\gamma_{\rm cs}$.

The key to torque estimation is to determine the amplitudes of the positive and negative half sine waves that would result in the same average torque as in Table 3.2 over one crankshaft period. As shown in Figure 3.16, it is assumed that the torque is zero when γ_{cs} is between 0 and 270°, and between 450° and 720°. For angles between 270° and 360° the torque is represented by a negative half sine wave, which correspond to the compression process, and for angles between 360° and 450° a positive half sine wave is used to represent the torque production in an internal combustion engine.

The average torque $\overline{T_E}$ over one crankshaft period is

$$\overline{T_{\rm E}} = \frac{1}{4\pi} \int_0^{4\pi} T_{\rm E} \, \mathrm{d}\gamma_{\rm cs}
= \frac{1}{4\pi} \left(\int_{1.5\pi}^{2\pi} A_1 \sin(2\gamma_{\rm cs}) \, \mathrm{d}\gamma_{\rm cs} + \int_{2\pi}^{2.5\pi} A_2 \sin(2\gamma_{\rm cs}) \, \mathrm{d}\gamma_{\rm cs} \right)
= \frac{1}{4\pi} (-A_1 + A_2)$$
(3.10)

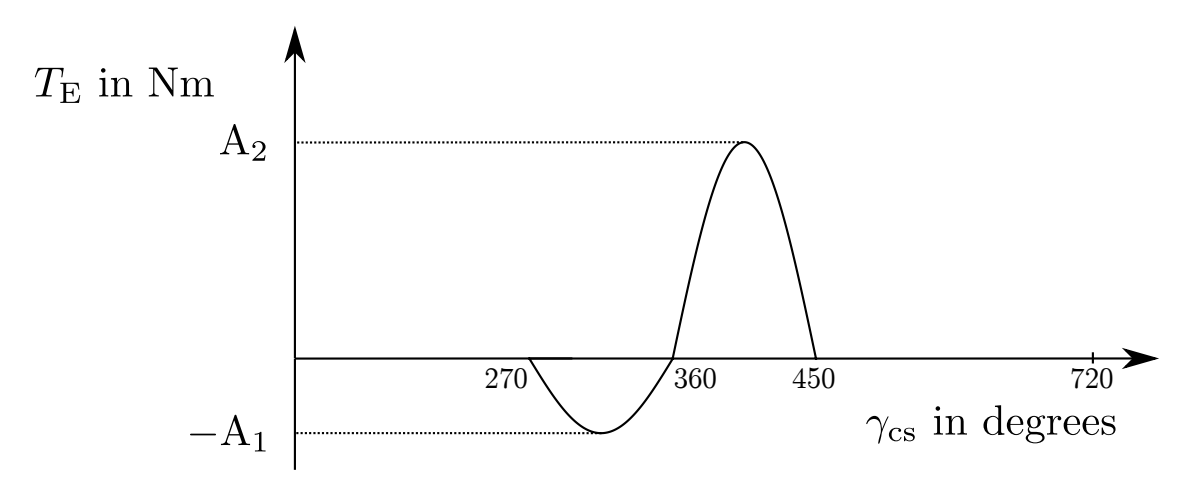


Figure 3.16: Estimated Instantaneous Engine Torque

Equation (3.10) shows that $\overline{T_E}$ depends on two parameters: A_1 and A_2 . Between 180° and 360° the ICE is in the compression phase where negative torque is produced to compress the air and fuel mixture. From Figures 3.15 and 3.16 the average compression torque produced by the ICE is

$$\overline{T_{\text{comp}}} = \frac{1}{\pi} \int_{\pi}^{2\pi} T_{\text{comp}} = \frac{1}{\pi} \int_{1.5\pi}^{2\pi} A_1 \sin(2\gamma_{\text{cs}}) d\gamma_{\text{cs}} = -\frac{A_1}{\pi} \Longrightarrow A_1 = -\pi \cdot \overline{T_{\text{comp}}}$$
(3.11)

Once A_1 is determined, A_2 can be calculated from Equation (3.10). Hence,

$$A_2 = 4\pi \cdot k_{\rm th} \cdot \overline{T_{\rm E}} + A_1 \tag{3.12}$$

Note that the factor $k_{\rm th}$ represents how wide the throttle is open. Its value could be anything from 0 to 1. A value of 1 or 0 means that the throttle is either completely open or completely closed, respectively. This factor scales the average torque $T_{\rm E}$ produced by the engine, and is used to operate the engine more efficiently since internal combustion engines are more efficient for a $k_{\rm th}$ value that is slightly less than 1 [25].

At 7750 rpm $\overline{T_{\rm comp}}$ is equal to $-40\,{\rm Nm}$. This value is considered to be equal for all speeds to ease the analysis.

Figure 3.17 shows the Simulink implementation for crankshaft angles between 270° and 360°, and Figure 3.18 shows the implementation for crankshaft angles between 360° and 450°. For all other angles, the instantaneous torque $T_{\rm E}$ is zero as demonstrated in Figure 3.16.

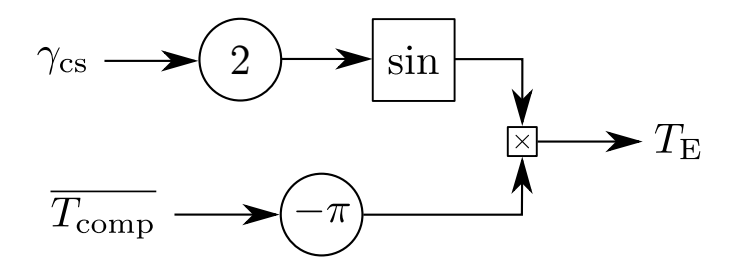


Figure 3.17: Torque generation for crankshaft angles between 270° and 360°

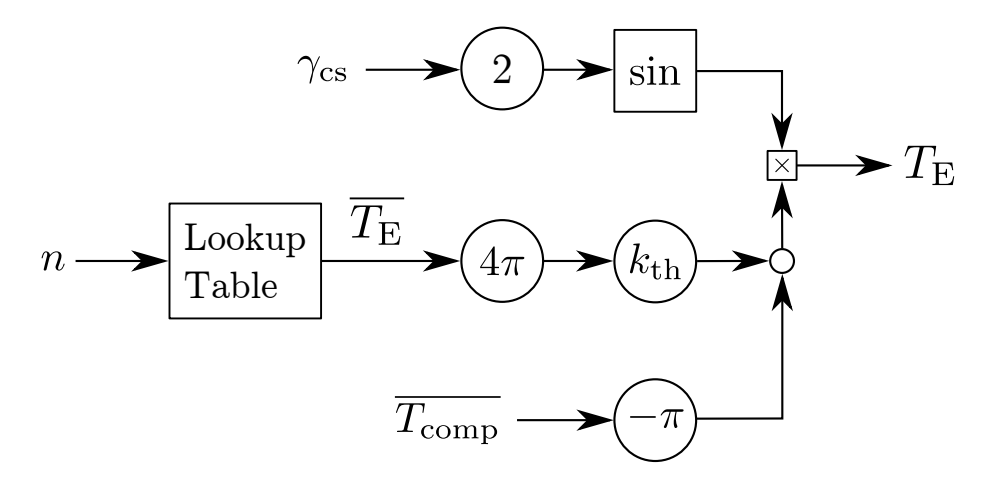


Figure 3.18: Torque generation for crankshaft angles between 360° and 450°

3.6 Mechanical System

The mechanical system models the interaction between the engine torque $T_{\rm E}$ and the SRG torque $T_{\rm G}$ to determine the shaft speed $\omega_{\rm m}$. Using Newton's Second Law,

$$T_{\rm E} + T_{\rm G} - T_{\rm friction} = J \frac{\mathrm{d}\omega_{\rm m}}{\mathrm{d}t}$$
 (3.13)

where J is the total inertia that includes the shaft, engine and rotor inertias, and T_{friction} is the friction torque, which is proportional to the cubic of shaft speed with c_{w} being the constant of proportionality.

$$T_{\text{friction}} = c_{\text{w}}\omega^3$$
 (3.14)

To find the shaft angle $\theta_{\rm m}$ a simple integration is applied to $\omega_{\rm m}$.

$$\theta_{\rm m} = \int \omega_{\rm m} dt \tag{3.15}$$

A block diagram that illustrates the implementation of Equations (3.13) and (3.15) is shown in Figure 3.19. The crankshaft angle $\gamma_{\rm cs}$ is obtained from $\theta_{\rm m}$ by counting from 0° to 720° instead of from 0° to 360°, which are the limits for $\theta_{\rm m}$.

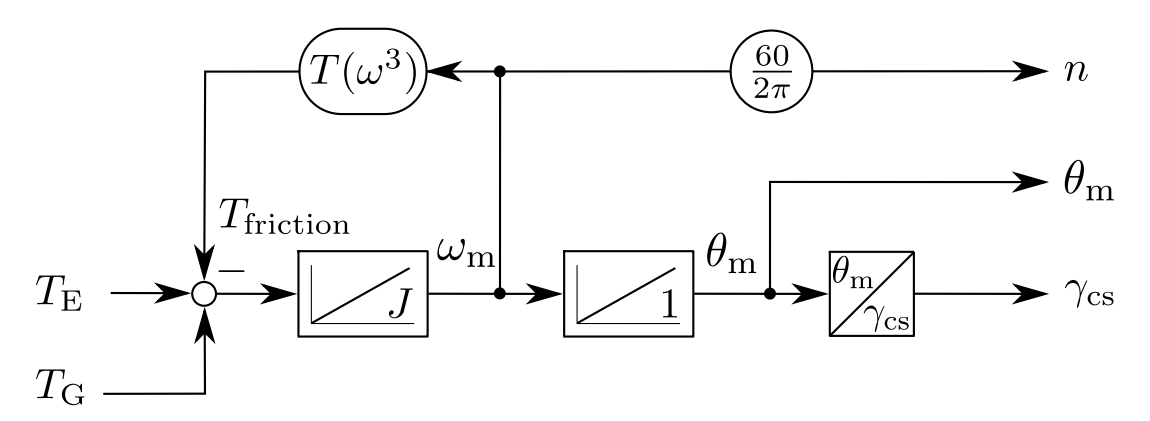


Figure 3.19: Mechanical System Model

3.7 Power, Losses and Efficiency Calculations

To assess the performance of the range extender system, it is important to estimate the various losses that occur starting from the engine down to the battery. The power flow in the system is shown in Figure 3.20. The different types of power shown in the figure are:

- P_{mech} : mechanical power supplied by the ICE
- P_{friction} : losses due to air friction
- $P_{\rm G}$: electrical power generated by the SRG
- P_{core} : losses in the core due to hysteresis and eddy currents
- P_{copper} : ohmic losses in the phase windings
- \bullet $P_{\rm conv}$: losses in the power electronic converter including switching and conduction losses
- P_{cable} : ohmic losses in the cable
- P_{bat}: electric power delivered to the battery

It is important to mention that Figure 3.20 shows the average power flow, and not the instantaneous. Precisely, power is momentarily drawn from the battery when a phase is excited.

In the following subsections the determination of each of the aforementioned powers is explained with the help of Figure 3.21.

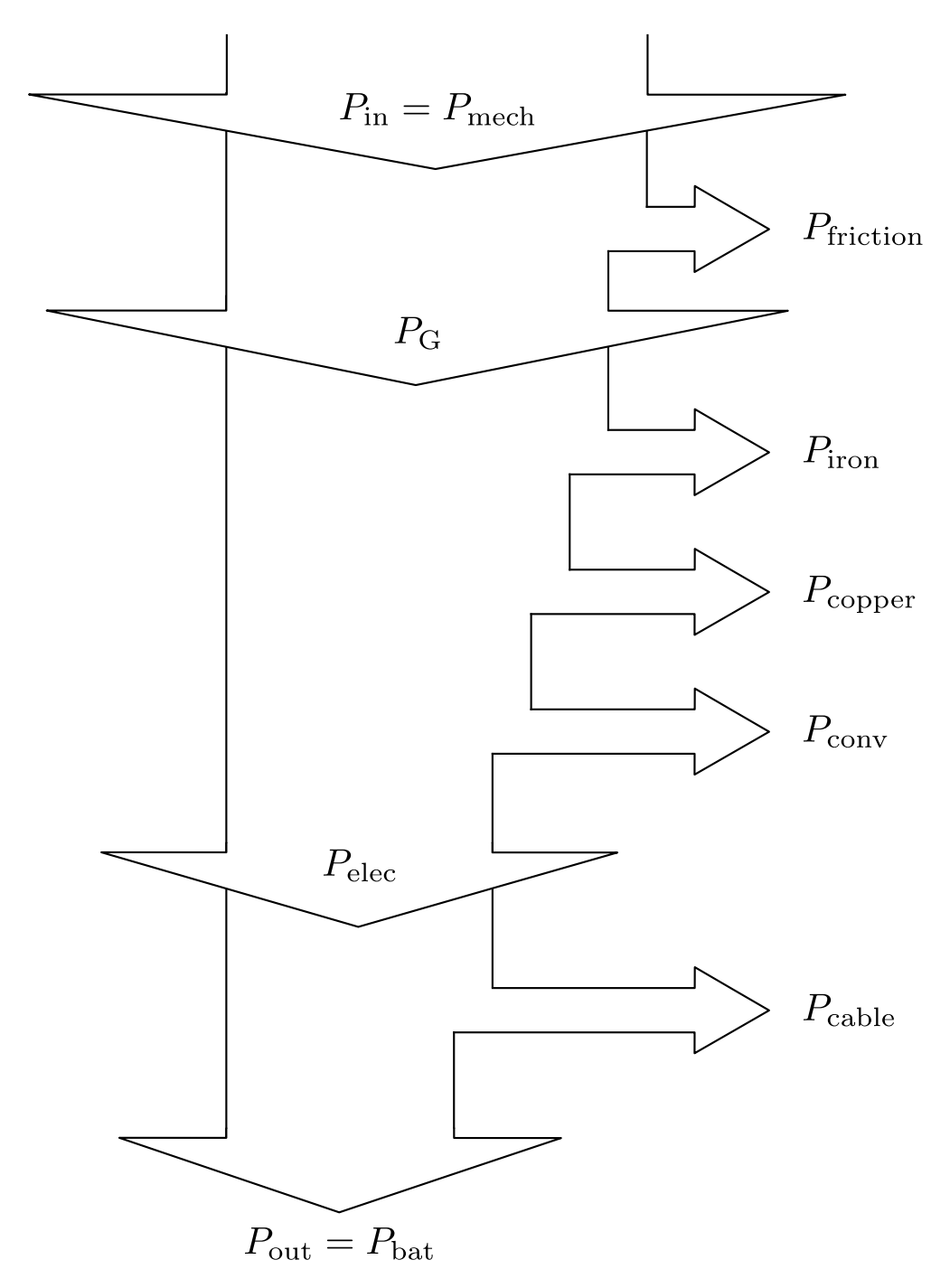


Figure 3.20: Average Power Flow in the Range Extender System

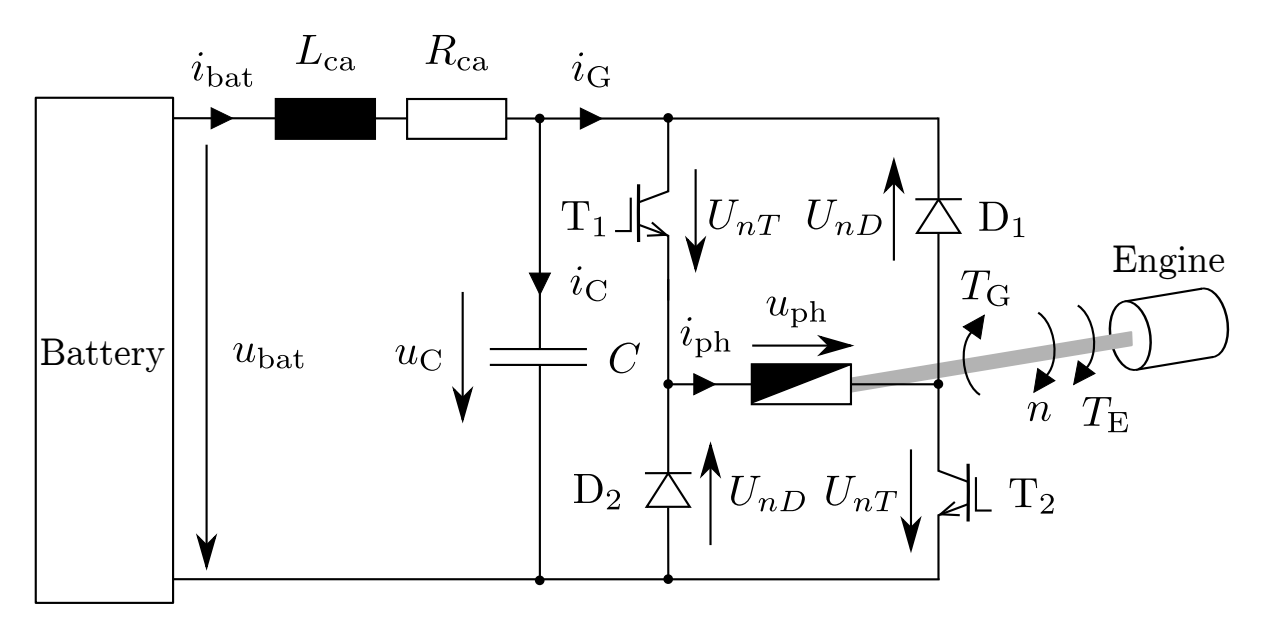


Figure 3.21: Diagram showing Complete Electrical System and ICE

3.7.1 Power Calculations

The instantaneous mechanical power p_{mech} supplied by the engine is the product of the instantaneous torque T_{E} and speed ω_{m} . Therefore, the average mechanical power P_{mech} is

$$P_{\text{mech}} = \overline{p_{\text{mech}}} = \frac{1}{T} \int_{0}^{T} p_{\text{mech}} dt = \frac{1}{T} \int_{0}^{T} T_{\text{E}} \cdot \omega_{\text{m}} dt$$
 (3.16)

The instantaneous electrical power $p_{\rm elec}$ is the power that is passed to the DC-link, i.e. it is the product of the DC-link voltage $u_{\rm C}$ and the generator current $i_{\rm G}$. Hence, the average electrical power $P_{\rm elec}$ is

$$P_{\text{elec}} = \overline{p_{\text{elec}}} = \frac{1}{T} \int_{0}^{T} p_{\text{elec}} dt = \frac{1}{T} \int_{0}^{T} u_{\text{C}} i_{\text{G}} dt$$
 (3.17)

The output of the range extender system is the battery charging power p_{bat} . This power is the product of the battery voltage u_{bat} and battery current i_{bat} .

$$P_{\text{bat}} = \overline{p_{\text{bat}}} = \frac{1}{T} \int_{0}^{T} p_{\text{bat}} dt = \frac{1}{T} \int_{0}^{T} u_{\text{bat}} i_{\text{bat}} dt$$
 (3.18)

3.7.2 Iron Losses

In this subsection the methodology to estimate the iron losses in the SRG is explained. First, the flux waveforms in the machine sections are determined. Next, the Steimitz parameters for the considered ferrite material are calculated. Finally, the losses are found by applying the improved Generalized Steinmitz Equation (iGSE).

3.7.2.1 Determination of Flux

To calculate iron losses the flux paths in machine must be determined first. In this analysis it is assumed that the rotor is always in the aligned position, so there is minimum reluctance in the magnetic circuit. The flux paths at the aligned position of each phase are shown in Figure 3.22. From this figure one can construct flux waveforms in the different machine sections. As illustrated in Figure 3.23, the machine is partitioned into eight stator poles (SP's), eight stator yoke sections (SY's), four rotor poles (RP's) and four rotor yoke sections (RY's).

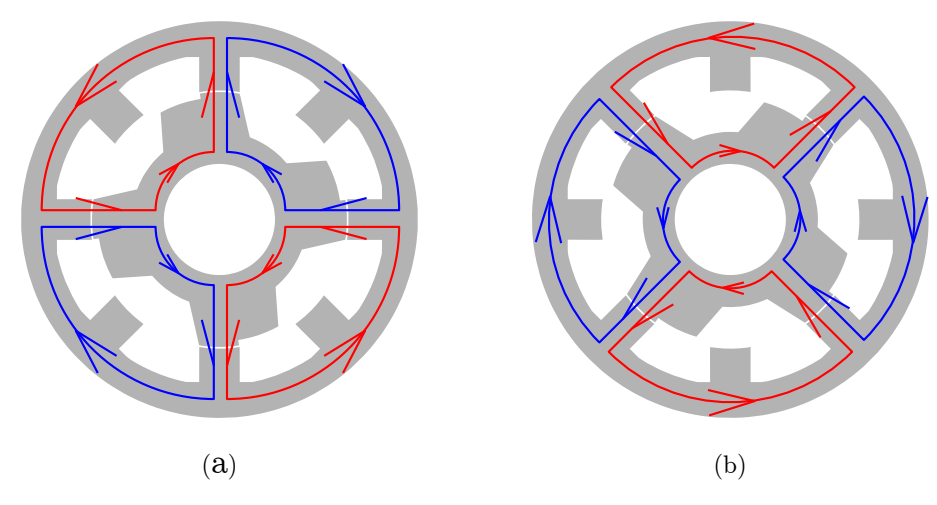


Figure 3.22: Flux Paths at the Aligned Position of: a) Phase 1 and b) Phase 2

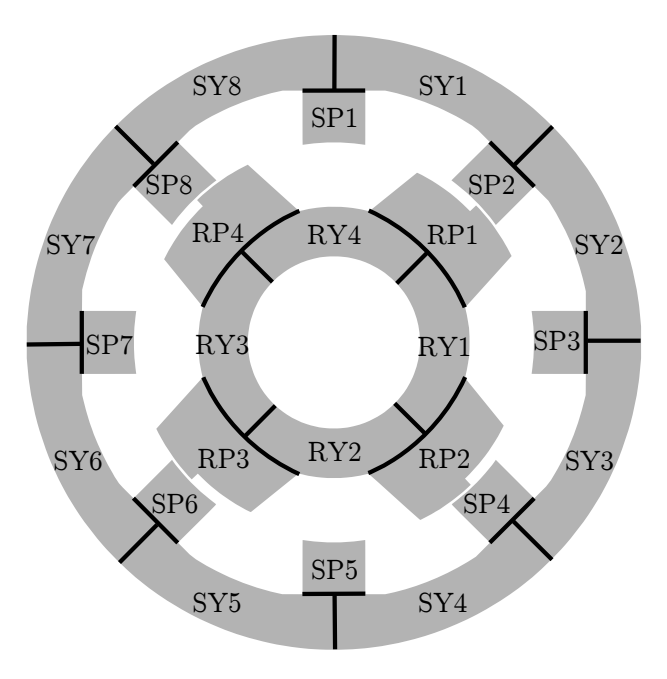


Figure 3.23: Partitioning of the SRG into Different Sections

Stator Pole Sections

In each stator pole the flux is equal to either the phase flux or zero. Figure 3.24 shows the flux in SP1 when both phases are energized. From the figure it is clear that when phase 1 is on, the flux in SP1 is equal to the phase flux, and when phase 2 is on, there is no flux. This is also true for SP3, SP5 and SP7. However, attention must be paid to the flux direction. Assuming the direction is positive when the flux is going out of the center, the flux in all stator poles can be calculated from the following equation.

$$\phi_{\text{SPn}} = \begin{cases} \phi_{\text{ph1}} & \text{for } n = 1, 5\\ -\phi_{\text{ph1}} & \text{for } n = 3, 7\\ \phi_{\text{ph2}} & \text{for } n = 2, 6\\ -\phi_{\text{ph2}} & \text{for } n = 4, 8 \end{cases}$$
(3.19)

The flux in each SP has a frequency equal to the electrical frequency $f_{\rm e}$. During one mechanical revolution the flux waveform in SP1 is shown in Figure 3.28 on page 41.

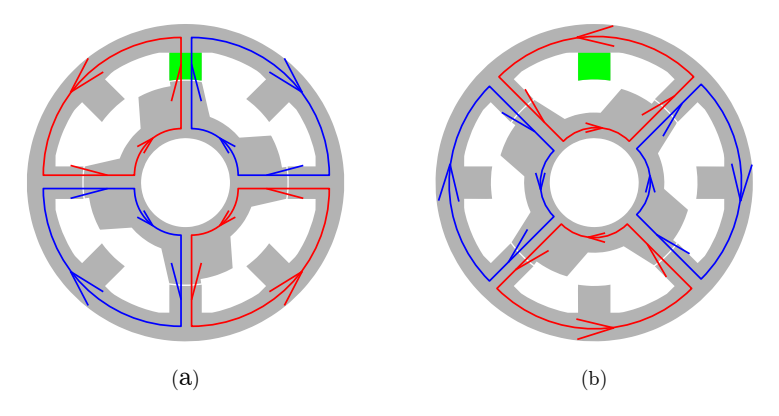


Figure 3.24: Flux in SP1 at the Aligned Position of: a) Phase 1 and b) Phase 2

Stator Yoke Sections

At any instant in time the flux in each stator yoke section (SY) is equal to half the phase flux. In Figure 3.25 two SY are highlighted, SY1 and SY6. When phase 1 is on, the flux in SY1 is equal to $\phi_{\rm ph1}/2$ and its direction is counter clockwise (CW). When phase 2 is on, the flux is also equal to $\phi_{\rm ph1}/2$ but the direction is clockwise (CCW). For SY6 the flux magnitude is equal to that in SY1. However, the direction is always CW. Thus, some SY sections experience flux reversal while others don't. Let a CCW direction be positive, then the flux in SY1 ϕ_{SY1} and SY6 ϕ_{SY6} sections are

$$\phi_{\text{SY1}} = \begin{cases} -\phi_{\text{ph1}} & \text{if phase 1 is active} \\ \phi_{\text{ph2}} & \text{if phase 2 is active} \end{cases}$$
 (3.20)

$$\phi_{\text{SY1}} = \begin{cases} -\phi_{\text{ph1}} & \text{if phase 1 is active} \\ \phi_{\text{ph2}} & \text{if phase 2 is active} \end{cases}$$

$$\phi_{\text{SY6}} = \begin{cases} -\phi_{\text{ph1}} & \text{if phase 1 is active} \\ -\phi_{\text{ph2}} & \text{if phase 2 is active} \end{cases}$$
(3.20)

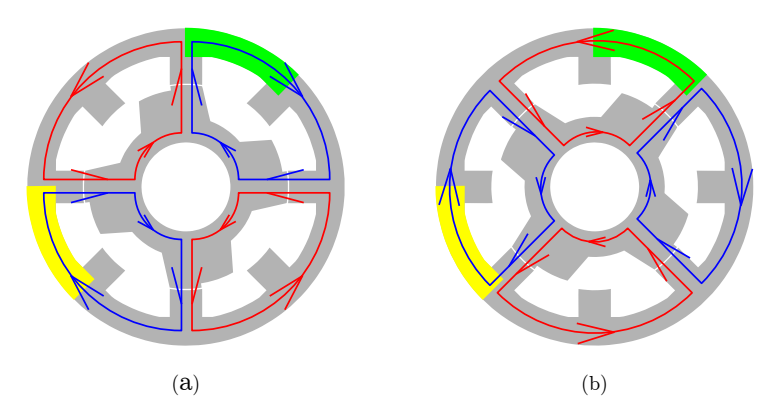


Figure 3.25: Flux in SY1 and SY6 at the Aligned Position of: a) Phase 1 and b) Phase 2

The flux frequency is equal to f_e in SY sections with flux reversal, and is equal to $2f_e$ in the sections in which the flux direction does not reverse.

Similar analysis can be applied to find the flux in other SY sections. The flux waveform in SY1 is shown in Figure 3.28 on page 41 for one mechanical period.

Rotor Pole Sections

The flux in the stator sections depend only on the phase fluxes. This is not the case for the rotor sections. Since the rotor position changes with time, flux in the rotor sections also depend on the rotor position. Figure 3.26 shows how the flux in RP1 varies as the rotor completes a half mechanical revolution. It is clear that one must know what stator pole is being aligned with what rotor pole. For example, if RP1 is aligned with SP1, ϕ_{RP1} is equal to ϕ_{SP1} , and if it is aligned with SP7, ϕ_{RP1} is equal to ϕ_{SP7} . This is also the case for all other RP sections. Therefore, determining the opposite SP at every moment is the way to obtaining the flux in any RP section. If the jth SP is opposite to the nth RP, then the flux in the nth RP ϕ_{RPn} is

$$\phi_{\rm RPn} = \phi_{\rm SPj} \tag{3.22}$$

Due to the dependency on the rotor position, $\phi_{\rm RPn}$ has a frequency equal to twice the mechanical frequency $f_{\rm m}$, which is equal to $f_{\rm e}/N_{\rm r}$. Figure 3.28 shows the flux waveform in RP1 during one mechanical revolution.

Rotor Yoke Sections

For the RY sections, the flux in each one ϕ_{RYn} is equal in magnitude to $0.5\phi_{\text{RPn}}$, and its direction depends on whether the flux is CW or CCW. Considering Figure 3.27, which shows the variations of flux in RY1, it is clear that if ϕ_{RP1} is positive (out of the center), then the direction of ϕ_{RY1} is CCW, and vice versa. Therefore, the flux in the nth RY section ϕ_{RYn} is

$$\phi_{\text{RYn}} = \phi_{\text{RPn}} \tag{3.23}$$

taking the CCW direction as positive. Contrary to SY sections, all RY sections experience flux reversal. Also, the flux frequency is equal to $2f_{\rm m}$ in each RY section. A typical flux waveform in RY1 is shown in Figure 3.28.

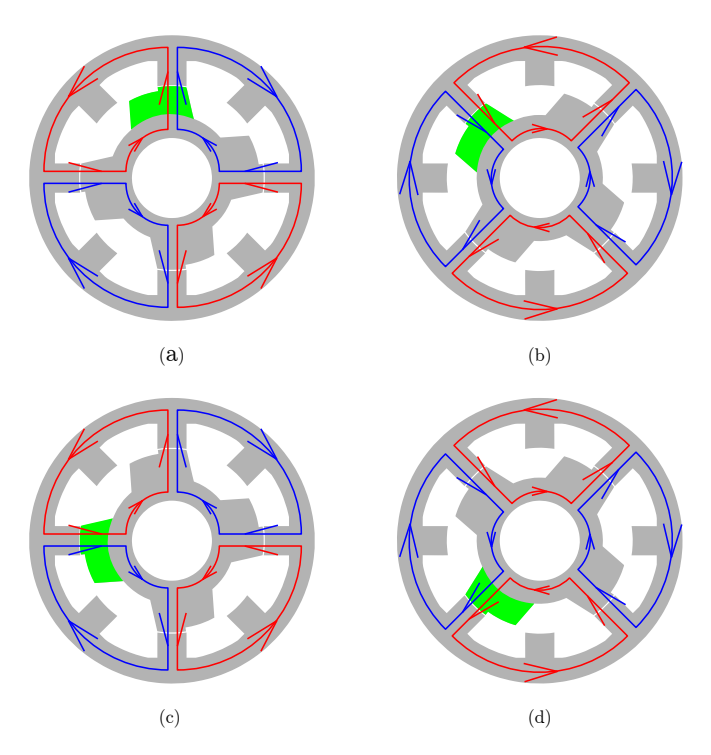


Figure 3.26: Flux in RP1 during a Half Mechanical Revolution

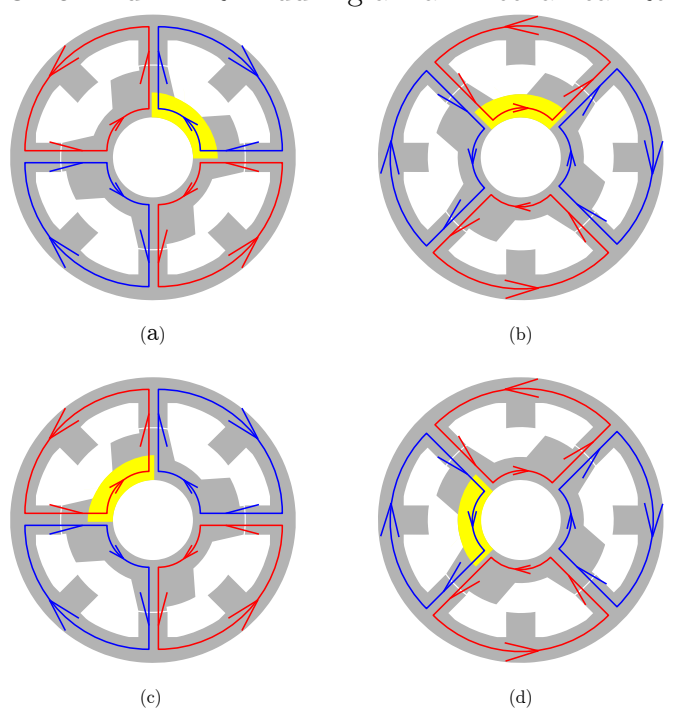


Figure 3.27: Flux in RY1 during a Half Mechanical Revolution

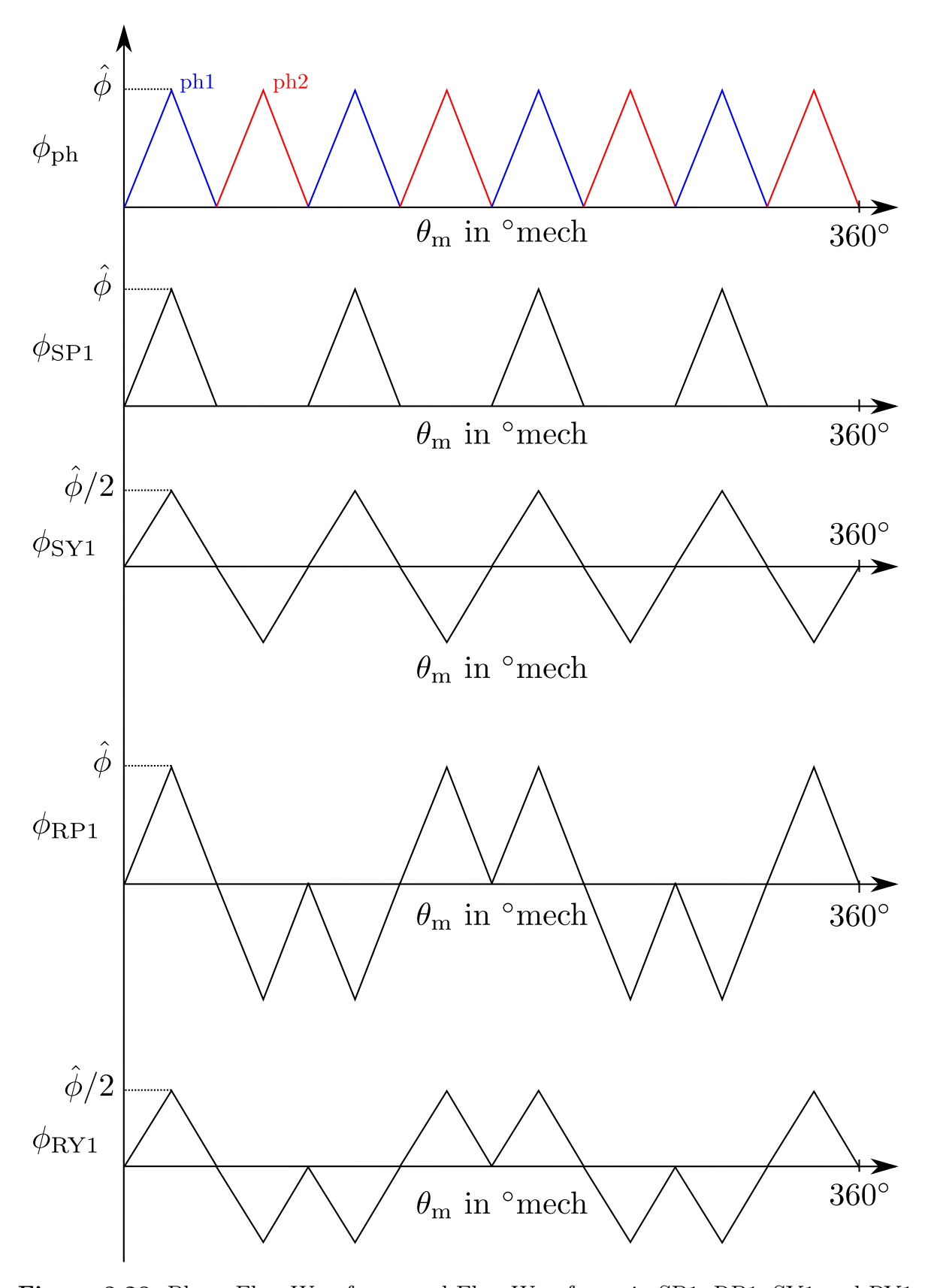


Figure 3.28: Phase Flux Waveforms and Flux Waveforms in SP1, RP1, SY1 and RY1

3.7.2.2 Calculation of Flux Densities

Once the flux ϕ in all machine sections is found, the flux density is calculated by dividing the flux by the area through which it flows.

$$B = \frac{\phi}{A} \tag{3.24}$$

The stator and rotor dimensions are shown in Figure 3.29, and the values are tabulated in Table 3.3. With the help of Figure 3.29, Equation (3.24), and Table 3.3, the flux densities in all machine sections are determined.

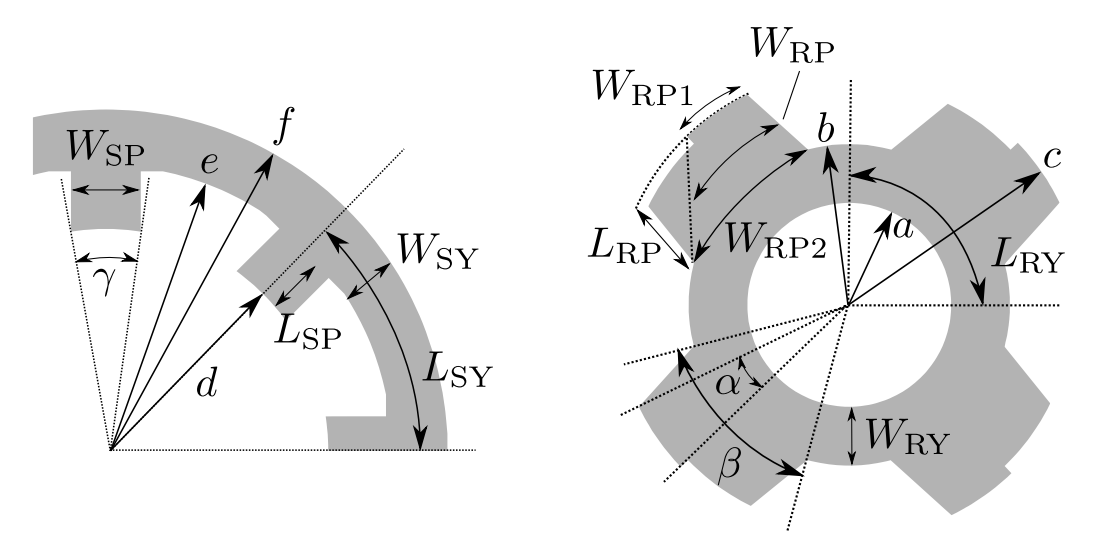


Figure 3.29: Stator and Rotor Dimensions

Table 3.	3: Values of	t Dimens	ions in F	igure 3.29
	Dimension	Value	Unit	
	_	20.0606		

Dimension	Value	Unit
a	30.8696	mm
b	48.557	mm
\mathbf{c}	70.6662	mm
d	71.6662	mm
e	92.0623	mm
f	110	mm
α	18	degrees
β	60	degrees
γ	18	degrees

In a stator pole (SP), the flux density B_{SP} is

$$B_{\rm SP} = \frac{\phi_{\rm SP}}{A_{\rm SP}} = \frac{\phi_{\rm SP}}{W_{\rm SP}L_{\rm s}} \tag{3.25}$$

where $W_{\rm SP}$ is the SP width and $L_{\rm s}$ is the stack length, which can be seen as the *depth* of the machine in Figure 3.29. The width is equal to

$$W_{\rm SP} = \frac{2\pi}{360^{\circ}} d\gamma \tag{3.26}$$

For a stator yoke (SY) section, the flux density B_{SY} is

$$B_{\rm SY} = \frac{\phi_{\rm SY}}{A_{\rm SY}} = \frac{\phi_{\rm SY}}{W_{\rm SY}L_{\rm s}} \tag{3.27}$$

where

$$W_{\rm SY} = f - e \tag{3.28}$$

The flux density in a rotor pole B_{RP} is found by

$$B_{\rm RP} = \frac{\phi_{\rm RP}}{A_{\rm RP}} = \frac{\phi_{\rm RP}}{W_{\rm RP}L_{\rm s}} \tag{3.29}$$

To simplify calculations, W_{RP} is taken to be the average of W_{RP1} and W_{RP2}

$$W_{\rm RP} = \frac{W_{\rm RP1} + W_{\rm RP2}}{2} \tag{3.30}$$

where

$$W_{\rm RP1} = \frac{2\pi}{360^{\circ}} c\alpha \tag{3.31}$$

and

$$W_{\rm RP2} = \frac{2\pi}{360^{\circ}} b\beta \tag{3.32}$$

In every rotor yoke (RY) section, the flux density B_{RY} is equal to

$$B_{\rm RY} = \frac{\phi_{\rm RY}}{A_{\rm RY}} = \frac{\phi_{\rm RY}}{W_{\rm RY}L_{\rm e}} \tag{3.33}$$

where

$$W_{\rm RY} = b - a \tag{3.34}$$

3.7.2.3 Steinmitz Parameters

The Steinmitz parameters can be calculated from the specific loss of the ferrite material using curve fitting. The material used in the model is M330-35A by Cogent [9]. The specific power loss depending on the frequency and flux density is shown in Table 3.4.

A tool has been developed at ISEA that calculates Steinmitz parameters from the specific loss data. Using the tool and the values in Table 3.4, the parameters are calculated and are shown in Table 3.5

-• ~	Pecin				cy in F		iauciia
		50	100	200	400	1000	2500
	0.1	0.03	0.04	0.1	0.27	1.30	5.44
	0.2	0.08	0.18	0.43	1.15	4.84	19.5
	0.3	0.16	0.38	0.92	2.45	10.0	40.9
	0.4	0.27	0.63	1.55	4.13	16.7	69.5
	0.5	0.39	0.92	2.30	6.16	24.9	107
Ε	0.6	0.52	1.24	3.16	8.58	34.9	154
	0.7	0.66	1.61	4.13	11.4	46.9	213
Flux Density in	0.8	0.82	2.01	5.23	14.5	61.3	287
ısit	0.9	1.00	2.46	6.45	18.2	78.3	373
Эег	1.0	1.19	2.96	7.83	22.3	98.4	476
×	1.1	1.42	3.52	9.37	27.0	122	
-lr	1.2	1.67	4.17	11.1	32.4		
ш	1.3	1.99	4.95	13.2	38.7		
	1.4	2.42	5.93	15.7	46.2		
	1.5	2.93	7.13	18.6	54.7		
	1.6	3.47					
	1.7	3.90					
	1.8	4.23					

Table 3.4: Specific Loss of M330-35A Ferrite Material in W/kg

Table 3.5: Steinmitz Parameters of M330-35A Ferrite Material

Parameter	Value	Unit
$\alpha_{ m st}$	1.6714	_
$eta_{ m st}$	2.1592	_
$k_{ m st}$	0.00098367	W/kg

3.7.2.4 Calculation of Iron Losses

Once the flux density waveforms in all machine sections and the Steinmitz parameters are obtained, the specific iron losses in the particular machine section can be calculated using the improved Generalized Steinmitz Equation (iGSE) (see Equations (2.28) and (2.29)). To do that the algorithm developed by [32] is used, which is available as a Matlab script. The algorithm, however, returns the losses per mass as specified by the unit of k. Thus, multiplication of the returned values by the mass is necessary. With the help of Figure 3.29, the volume of each stator pole (SP), stator yoke (SY), rotor pole (RP) and rotor yoke (RY) section is

$$V_{\rm SP} = L_{\rm SP} W_{\rm SP} L_{\rm s} \tag{3.35}$$

$$V_{\rm SY} = \frac{\pi}{8} (f^2 - e^2) L_{\rm s} \tag{3.36}$$

$$V_{\rm RP} = L_{\rm RP} W_{\rm RP} L_{\rm s} \tag{3.37}$$

$$V_{\rm SY} = \frac{\pi}{4} (b^2 - a^2) L_{\rm s} \tag{3.38}$$

where

$$L_{\rm SP} = e - d \tag{3.39}$$

$$L_{\rm RP} = c - b \tag{3.40}$$

The density of M330-35A is 7650 kg/m³. Taking into account that the iron material is laminated, the density is therefore

$$\rho = 7650(0.97) = 7421 \,\frac{\text{kg}}{\text{m}^3} \tag{3.41}$$

3.7.3 Converter Losses

The conduction losses are calculated using Equations (2.30) and (2.31) with $U_{\rm nS}$ and $U_{\rm nD}$ equal to 1 and 0.9 V, respectively [26, 27].

The switching losses are the turn-off losses of the IGBTs only (see Section 2.2.5.4). In order to calculate the turn-off losses the characteristics shown in Figure 3.30 are used [26, 27]. The turn-off energy is a function of the IGBT current at the moment the IGBT is turned off.

$$E_{\text{off}} = f(I_{\text{off}}) \tag{3.42}$$

where

$$I_{\text{off}} = i_{\text{ph}}|_{\theta = \theta_{\text{off}}} \tag{3.43}$$

Once E_{off} is obtained, the switching losses are calculated using Equations (2.33) to (2.35).

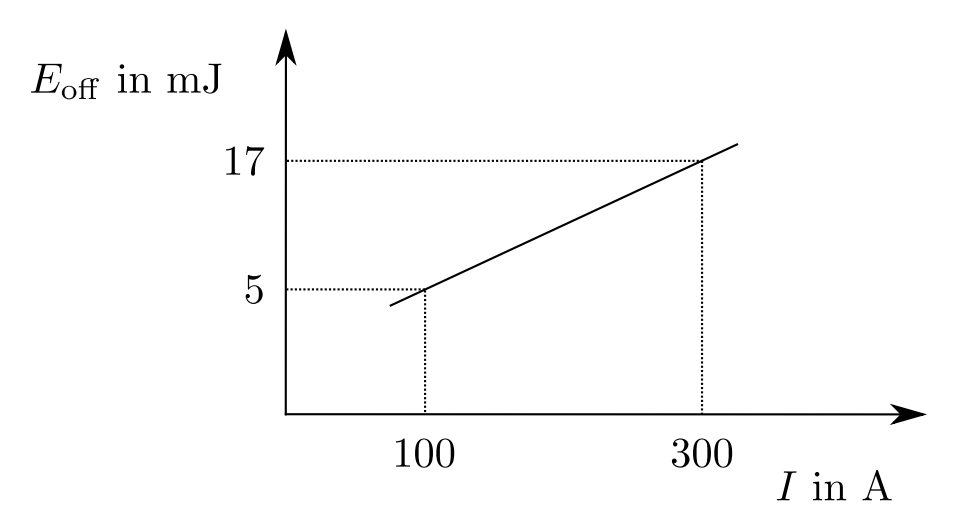


Figure 3.30: Relationship between IGBT Current and Switching Losses

3.7.4 Ohmic Losses

Ohmic losses include the losses in the copper material of the phase winding P_{copper} and in the cable P_{cable} . P_{copper} is calculated using Equations (2.23) and (2.24). Using a similar approach and considering Figure 3.21, P_{cable} is equal to

$$P_{\text{cable}} = \overline{p_{\text{cable}}} = \frac{1}{T} \int_{0}^{T} p_{\text{cable}} dt = \frac{1}{T} \int_{0}^{T} R_{\text{ca}} i_{\text{bat}}^{2} dt = R_{\text{ca}} I_{\text{bat,rms}}^{2}$$
(3.44)

3.7.5 Friction Losses

Since Friction losses are proportional to the cubic of speed, the highest friction losses are obtained at the highest operating speed. According to PC-SRD calculations, these losses amount to approximately 10 W at 7500 rpm. Because 10 W is very small compared to other losses in the system, and because the friction losses depend only on the speed and, hence, do not change with the control angles, it is decided to neglect them in the efficiency calculations.

3.7.6 Efficiency

The efficiency η of the range extender system is calculated by

$$\eta = \frac{P_{\text{out}}}{P_{\text{in}}} \tag{3.45}$$

Considering Figure 3.20 and neglecting air friction losses P_{friction} , η is equal to

$$\eta = \frac{P_{\text{bat}}}{P_{\text{G}}} \tag{3.46}$$

Since

$$P_{\rm G} = P_{\rm elec} + P_{\rm iron} + P_{\rm copper} + P_{\rm conv} \tag{3.47}$$

system efficiency can also be calculated by

$$\eta = \frac{P_{\text{bat}}}{P_{\text{elec}} + P_{\text{iron}} + P_{\text{copper}} + P_{\text{conv}}}$$
(3.48)

4 Optimization and Analysis

This chapter presents the methodology of optimizing the performance of the range extender system. Emphasis has been put on maximizing efficiency and minimizing the radial forces to develop operating strategies for the range extender at the maximum speed and nominal power. Sensitivity analysis due to changes in system parameters are observed for both optimized operating strategies. In addition, the effects of using a real battery model are explored.

4.1 Optimization Process

Optimization is carried out using a Genetic Algorithm (GA). It starts by generating a population of chromosomes randomly. Next, it evaluates how fit each chromosome is by calculating the fitness value from simulation results. After that, the parents are selected using the roulette wheel selection scheme, and the offspring are created using uniform crossover and mutation with probabilities of 0.9 and 0.1, respectively. The offspring then replace the weaker chromosomes from the previous generation, and the process starts all over once again. This process is repeated until a maximum number of generations have been produced. Figure 4.1 shows one cycle of the optimization process.

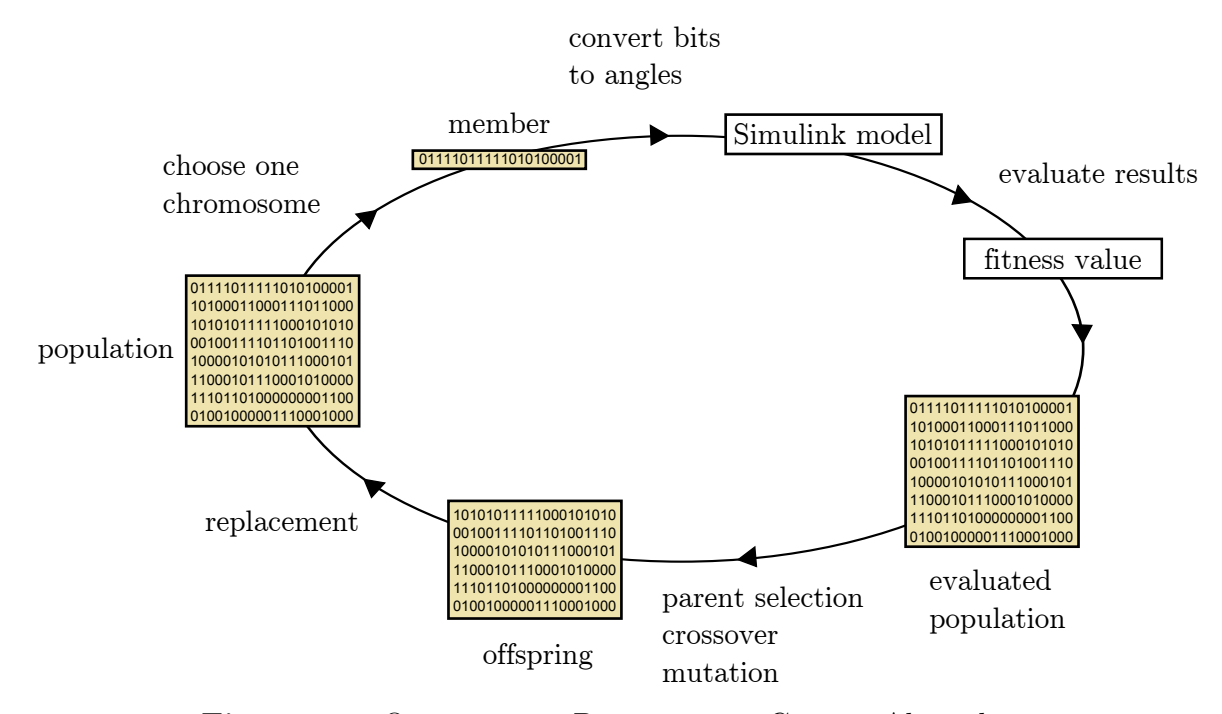


Figure 4.1: Optimization Process using Genetic Algorithms

4.1.1 Chromosome

Each chromosome in Figure 4.1 is a string of bits. These bits carry information for a certain turn-on angle θ_{on} , conduction angle θ_{cond} and free-wheeling angle θ_{fw} as shown in Figure 4.2. The first r bits represent θ_{on} , the next s bits are allocated for θ_{cond} , and the last t bits are for θ_{fw} .

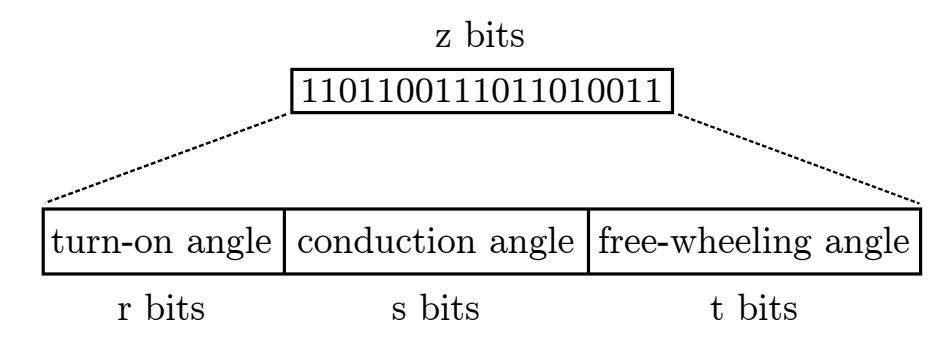


Figure 4.2: Breakdown of Information carried in a Chromosome

The length of the chromosome depend on the ranges of angles wherein the GA searches. If the GA is set to search in the range bounded by $\theta_{\text{on}}^{\min}$, $\theta_{\text{on}}^{\max}$, $\theta_{\text{cond}}^{\min}$, $\theta_{\text{cond}}^{\max}$, $\theta_{\text{fw}}^{\min}$, and $\theta_{\text{fw}}^{\max}$, then

$$r = \left\lceil \frac{\ln(\theta_{\text{on}}^{\text{max}} - \theta_{\text{on}}^{\text{min}} + 1)}{\ln 2} \right\rceil \tag{4.1}$$

$$s = \left\lceil \frac{\ln(\theta_{\text{cond}}^{\text{max}} - \theta_{\text{cond}}^{\text{min}} + 1)}{\ln 2} \right\rceil \tag{4.2}$$

$$t = \left\lceil \frac{\ln(\theta_{\text{fw}}^{\text{max}} - \theta_{\text{fw}}^{\text{min}} + 1)}{\ln 2} \right\rceil \tag{4.3}$$

and the total number of bits z is therefore

$$z = r + s + t \tag{4.4}$$

This means that as the ranges increase in size, the number of bits also increases. For that reason, it is advisable to specify search ranges as small as possible, since the number of combinations becomes fewer and, therefore, the chances of finding the best chromosome increase.

4.1.2 Fitness Value

The fitness value FV of a chromosome determines how good the chromosome is. It is calculated by

$$FV = \sum F_{\rm cr} W_{\rm cr} \tag{4.5}$$

with $F_{\rm cr}$ being the fitness of a certain criterion and $W_{\rm cr}$ is the weight of that criterion. Examples of criteria in an optimization process include power, efficiency, rms current, maximum

radial force and so on. The criterion fitness $F_{\rm cr}$ could be anything from 0 to 1. If it is equal to 1 then it means that the goodness of the criterion has been maximized, and if it is equal to 0, then the chromosome is bad when assessed according to that criterion. The fitness functions of different criteria are shown in Figure 4.3.

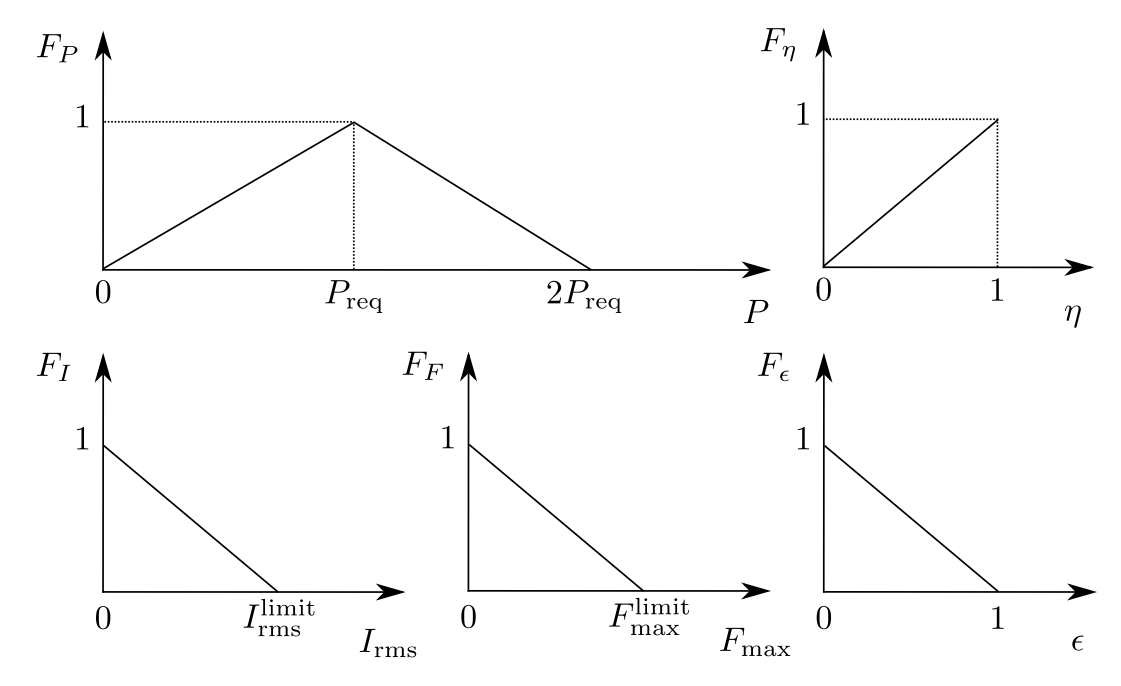


Figure 4.3: Fitness Functions of Different Criteria

The parameters $I_{\rm rms}^{\rm limit}$ and $F_{\rm max}^{\rm limit}$ shown in Figure 4.3 represent two values that are too big that cannot be achieved at rated operation. After investigating the range extender system, it is decided to use the following values for $I_{\rm rms}^{\rm limit}$ and $F_{\rm max}^{\rm limit}$ throughout the optimization process.

$$I_{\rm rms}^{\rm limit} = 400 \,\mathrm{A} \tag{4.6}$$

$$F_{\text{max}}^{\text{limit}} = 2000 \,\text{N} \tag{4.7}$$

Furthermore, the required power P_{req} is rounded to nearest hundred of Watts. So if 20 kW is desired, then 19.95 kW and 20.04 kW will result in the highest value for F_{power} .

Like the fitness, the weight parameter $W_{\rm cr}$ takes any value between 0 and 1. The higher $W_{\rm cr}$, the more emphasis is put on this particular criterion. Because achieving the desired power is of highest importance, the value $W_{\rm power}$ is much larger than those of other criteria.

4.2 Example of Optimized Range Extender Operation

In order to see the importance of optimization for the operation of the range extender system, three operating points are presented in which the SRG rotates at a fixed speed and generates electrical power according to Table 4.1. Each point has been optimized for two different criteria, which are maximizing efficiency η and minimizing the radial force F. The fitness value FV for each optimization process is calculated as follows with the help of Figure 4.3 and Equation (4.5).

$$FV_{\eta} = f(P,\eta) = F_{P}W_{P} + F_{\eta}W_{\eta}$$

$$= \left(1 - \left[\frac{1}{P_{\text{req}}}|P - P_{\text{req}}|\right]\right)(0.9) + \eta(0.1)$$
(4.8)

$$FV_F = f(P, F_{\text{max}}) = F_P W_P + F_F W_F$$

$$= \left(1 - \left[\frac{1}{P_{\text{req}}} |P - P_{\text{req}}|\right]\right) (0.9) + \left(1 - \frac{F_{\text{max}}}{F_{\text{max}}^{\text{limit}}}\right) (0.1)$$
(4.9)

Note that a weight of 0.9 has been allocated for the power, and 0.1 for the other criteria. The values of the system parameters are given in Table 4.2.

Table 4.1: Considered Operating Points

n in rpm	$P_{\rm G}$ in kW
7500	20.0
5000	12.5
3000	7.0

Table 4.2: Values of Parameters in the Range Extender System

Parameter	Value	Unit	Description
R_{wind}	0.0277	Ω	Winding Resistance
C	1	mF	DC-link Capacitance
R_{ca}	1	$\mathrm{m}\Omega$	Cable Resistance
$L_{ m ca}$	3	$\mu \mathrm{H}$	Cable Inductance
$R_{ m ser}$	50	$\mathrm{m}\Omega$	Series Resistance of Ideal Battery
$U_{\rm OC}$	300	V	Open-circuit Voltage of Ideal Battery

Operation at 7500 rpm and 20.0 kW

This is the rated operating point of the SRG. Figure 4.4 shows the phase current $i_{\rm ph}$, the DC-link voltage $u_{\rm C}$, the battery current $i_{\rm bat}$ and the radial force F for two optimized performances. Other results are tabulated in Table 4.3. A limit of 500-A is imposed on the phase current while optimizing for minimum radial force.

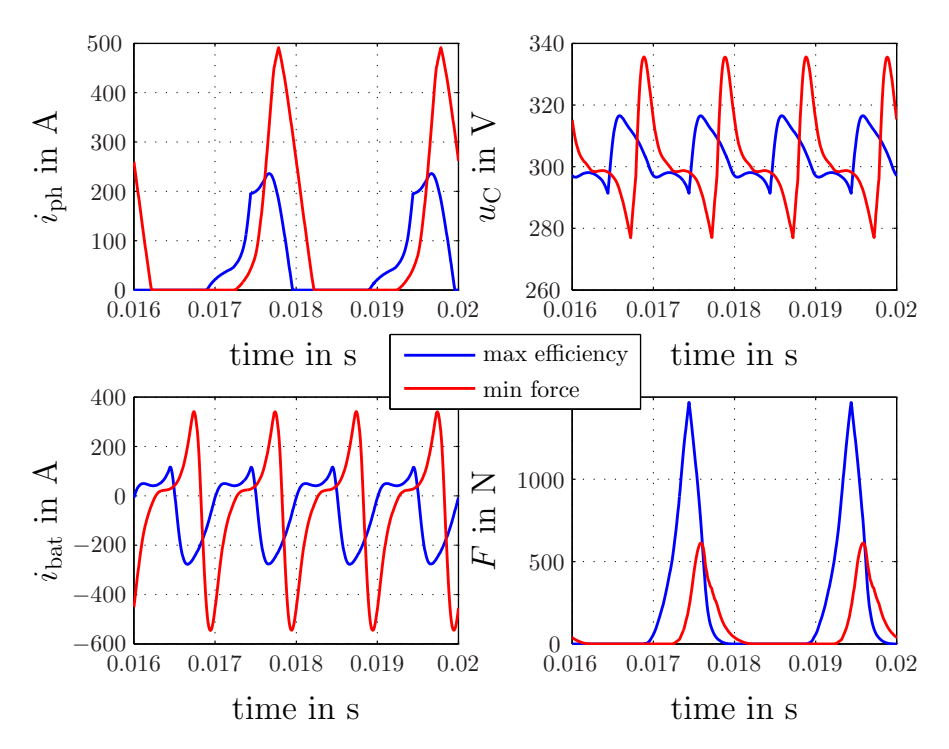


Figure 4.4: Comparison of Most Efficient and Minimum Radial Force Operating Point at 7500 rpm

Table 4.3: Results for the Cases shown in Figure 4.4

	Maximum Efficiency	Minimum Force
$\theta_{\rm on}$ in °elec	162	220
$\theta_{\rm off}$ in °elec	259	306
$P_{\rm G}$ in kW	20.0	20.0
P_{bat} in kW	19.6	19.3
η in percent	96.6	94.9
$I_{\rm rms}$ in A	142.9	225.0
$F_{\rm max}$ in N	1469	675.7

Obviously, there are advantages and disadvantage for each point. The most efficient performance has lower losses, lower peak currents and lower voltage ripple, while the other one has lower peak radial force. It can also be observed that the phase currents continue to increase in the most efficient performance after the switches are opened, resulting in an uncontrollable current peak.

Operation at 5000 rpm and 12.5 kW

At this operating point the back-EMF does not attain values higher the DC-link voltage. As a result, the peaks in the phase current are controllable. The different system variables are shown in Figure 4.5, and the results are given in Table 4.4.

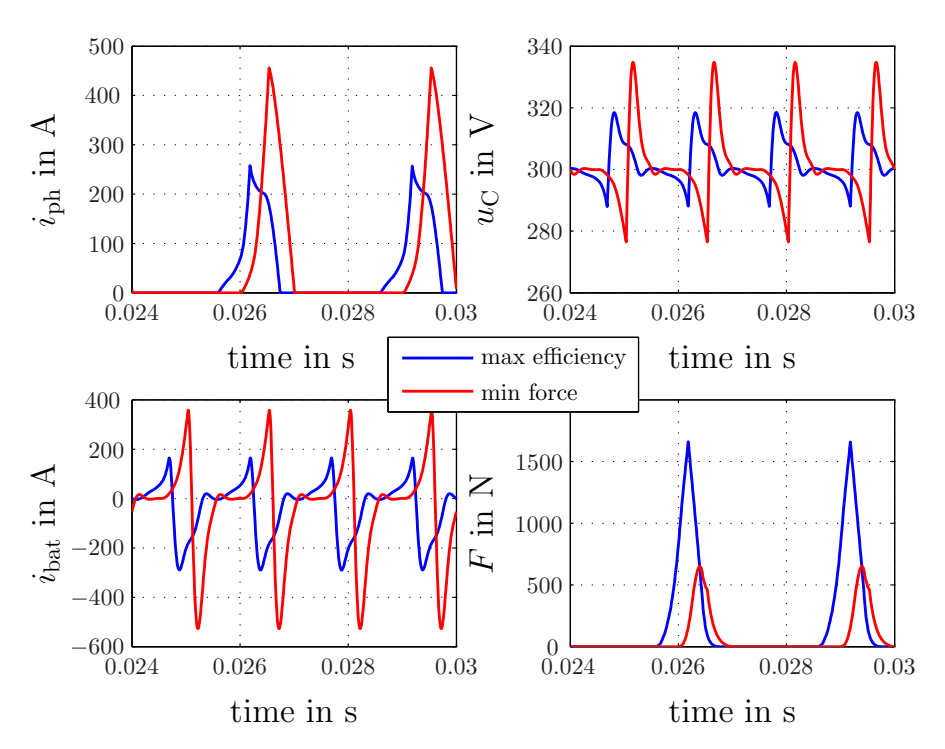


Figure 4.5: Comparison of Most Efficient and Minimum Radial Force Operating Point at 5000 rpm and 12.5 kW

Table 4.4: Results for the Cases shown in Figure 4.5

	Maximum Efficiency	Minimum Force
$\theta_{\rm on}$ in °elec	191	243
$\theta_{\rm off}$ in °elec	261	304
$P_{\rm G}$ in kW	12.5	12.5
P_{bat} in kW	12.2	11.9
η in percent	95.2	93.5
$I_{\rm rms}$ in A	123.6	197.7
F_{max} in N	1661	649.6

Note that the efficiency η is lower compared with the previous case. Also, the maximum values of the phase currents are close to those shown in Figure 4.5, which means that the thermal consequences are comparable.

Operation at 3000 rpm and 7.0 kW

The small back-EMF value at this operating point results in phase currents with high rates of increase. Plots of system variables and simulation results are shown in Figure 4.6 and Table 4.5, respectively.

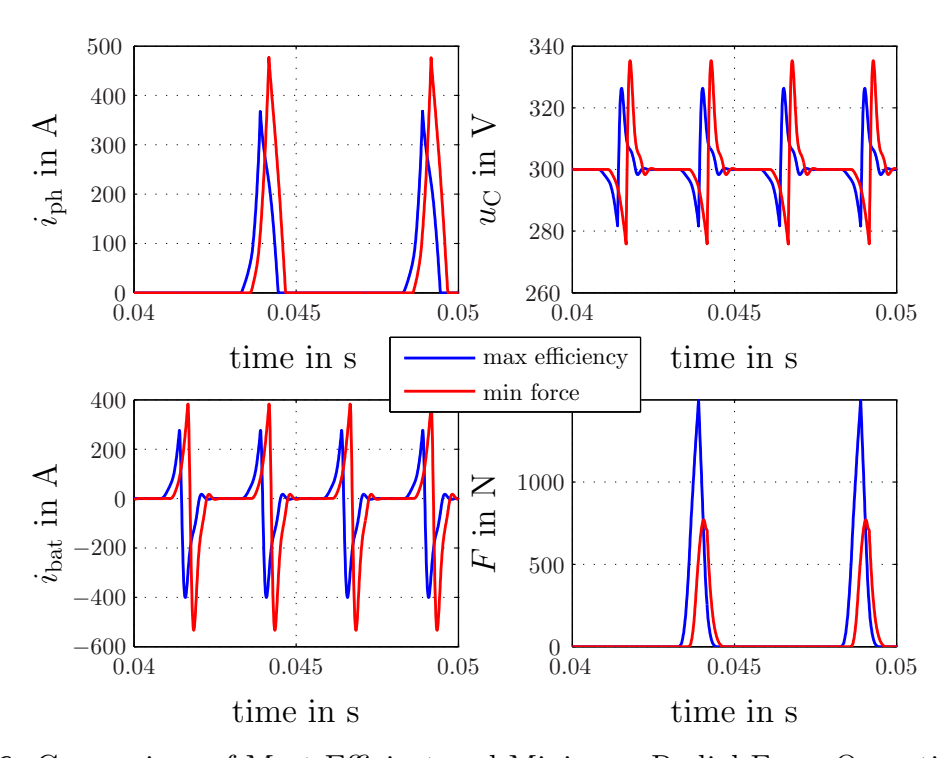


Figure 4.6: Comparison of Most Efficient and Minimum Radial Force Operating Point at 3000 rpm

Table 4.5:	Results	tor	the	Cases	shown	in	Figure	4.6
------------	---------	-----	-----	-------	-------	----	--------	-----

	Maximum Efficiency	Minimum Force
$\theta_{\rm on}$ in °elec	237	258
$\theta_{\rm off}$ in °elec	279	298
$P_{\rm G}$ in kW	7.0	7.0
P_{bat} in kW	6.8	6.6
η in percent	92.6	90.3
$I_{\rm rms}$ in A	126.1	163.0
$F_{\rm max}$ in N	1499	770.7

As a result, having the SRG operate at one speed while generating a specific power level may lead to undesirable behavior in the system variables. Therefore, it is important to optimize the performance of the range extender system according to the design specifications.

4.3 Optimization for Minimum Radial Forces

To optimize the acoustic behavior of SRGs, a control strategy will attempt to push $\theta_{\rm on}$ near the unaligned position as much as possible. In addition, it is possible to let the current free-wheel before demagnetizing the phase. Free-wheeling decreases the rate at which the current rises (Equation (3.4)), which allows to control the shape of the current waveform to obtain lower radial forces [13].

However, higher phase currents will be forced to achieve the desired power level near the aligned position. This will result in high current peaks that may cause thermal overloading of the power electronic devices. Therefore, setting up a limit on the phase current is necessary for a safe operation of the converter.

In Figure 4.7 phase currents and radial forces are plotted for different phase current limits at 7500 rpm. Several points can be deduced from the figure. Firstly, for a specific limit, introducing free-wheeling angles does not improve the radial forces considerably. This is expected as this is the rated operating point of the SRG. In addition, there is no considerable difference in the radial forces between the 400- and 500-A limits. However, the forces increase when a 300-A limit is imposed on the phase currents. Efficiency and voltage ripple are given in Table 4.6.

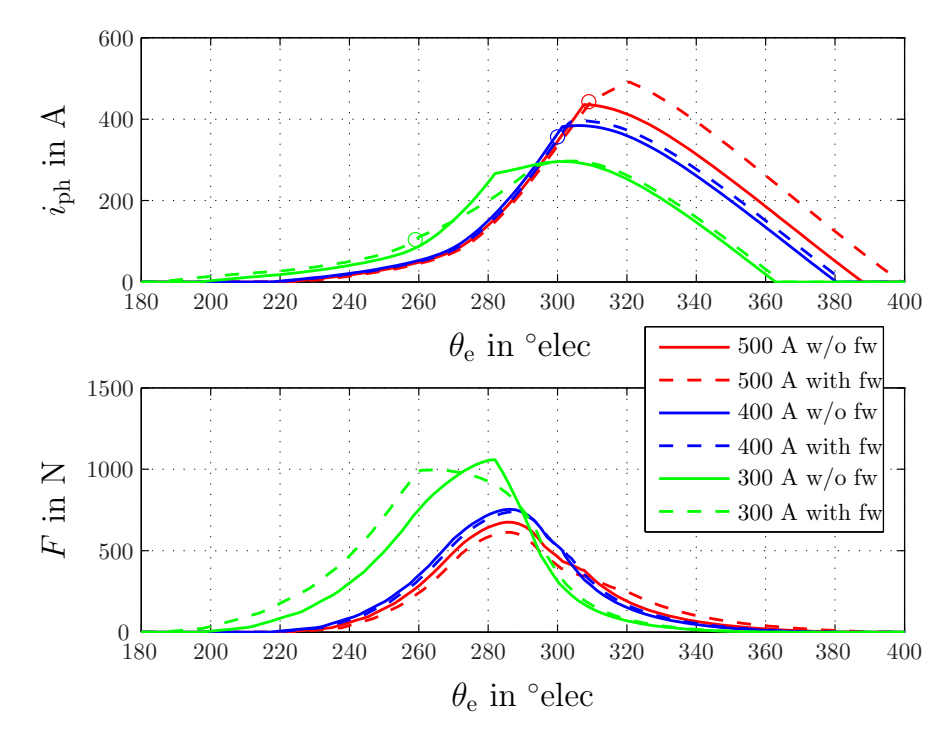


Figure 4.7: Phase Current and Radial Force for Different Phase Current Limits at 7500 rpm - Circles indicate Instants of Free-wheeling

		_		. I. I.			0
	500 A	limit	400 A	limit	300 A		
	w/o fw	with fw	w/o fw	with fw	w/o fw	with fw	
η in %	94.8	94.1	95.4	95.3	96.3	94.7	-
$U_{\rm r}$ in %	18.4	19.3	16.2	16.5	11.8	8.3	

Table 4.6: Efficiency and DC-link Voltage Ripple for the Cases in Figure 4.7

At low speeds demagnetization occurs rapidly due the small back-EMF compared to the DC-link voltage. Therefore, increasing the current peaks is necessary achieve a desired generation level. This has negative consequences on the radial force, as sharp current waveforms will cause sharp radial forces. However, free-wheeling results in lower rate of increase in the current, and, therefore, leads to smaller current peaks and improved radial forces. In Figure 4.8 the phase current and radial force are plotted for three phase current limits at 3000 rpm. Efficiency and voltage ripple are given in Table 4.7. Several points can be concluded from Figure 4.8 and Table 4.7. Firstly, with a 400-A limit, free-wheeling has bigger effect on the force compared with Figure 4.7. In addition, it is possible to meet the power requirement with a 300-A limit only when free-wheeling is introduced. An interesting outcome that can also be observed is that the free-wheeling interval is started around the aligned position. This could serve as a control strategy at low speeds to minimize the radial forces. Starting free-wheeling at the aligned position has two advantages. Firstly, less energy is drawn from the battery, since the back-EMF is used to build up the current. In addition, free-wheeling lets the current increase slowly around the aligned position where the radial forces are at maximum.

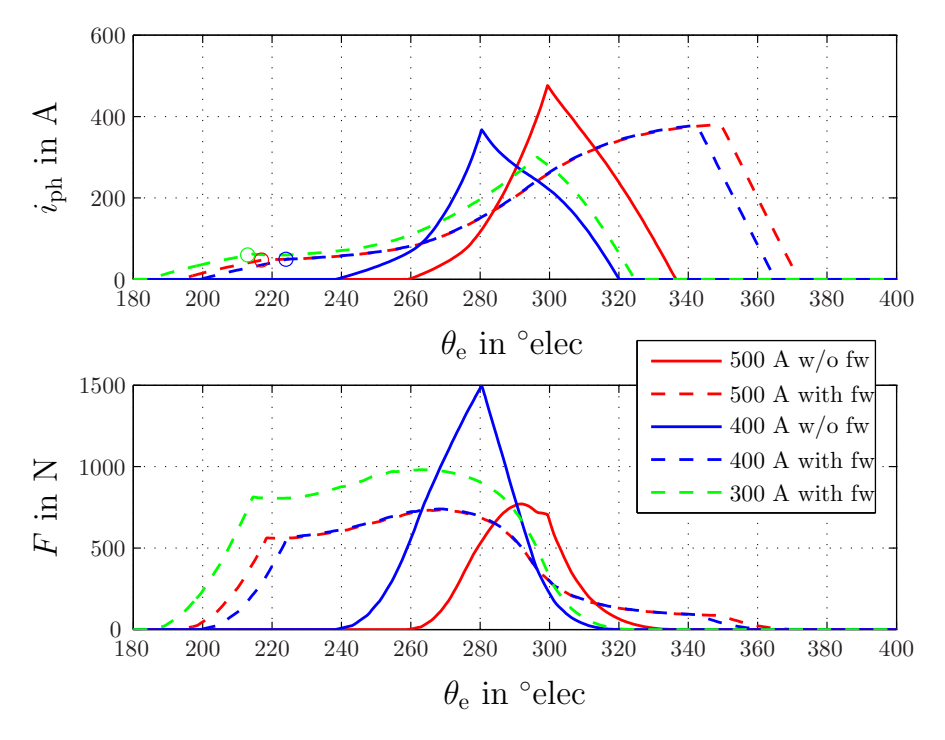


Figure 4.8: Phase Current and Radial Force for Different Phase Current Limits at 3000 rpm - Circles indicate Instants of Free-wheeling

			_				
	500 A	limit	400 A	limit	300 A limit		
	w/o fw with fw		w/o fw with fw		w/o fw	with fw	
η in %	90.3	89.8	92.6	90.7	_	94.3	
$U_{\rm r}$ in $\%$	19.6	7.9	14.8	7.9	_	7.1	

Table 4.7: Efficiency and DC-link Voltage Ripple for the Cases in Figure 4.8

4.3.1 Effects of Varying DC-link Capacitance

To meet the DC-link voltage ripple requirements increasing the DC-link capacitance C provides an easy and direct solution. So a variation in the capacitance size allows for a quick determination of the minimum size to meet the design specifications. The DC-link voltage $u_{\rm C}$ and battery current $i_{\rm bat}$ are plotted in Figure 4.9 for different capacitance sizes. The figure suggests that in order to have a voltage ripple of less than 8% a minimum capacitance of 5 mF is required.

The rate of change of the battery current i_{bat} is

$$\frac{di_{\text{bat}}}{dt} = \frac{1}{L_{\text{ca}}} (U_{\text{OC}} - u_{\text{C}} - (R_{\text{ser}} + R_{\text{ca}})i_{\text{bat}})$$
(4.10)

The increase in C leads to a smaller change in $u_{\rm C}$, and, therefore, a slower $i_{\rm bat}$ response (Equation (4.10)). Consequently, increasing C not only improves the voltage ripple, but also prevents the battery current from exceeding the charging limit. However, the bigger the capacitance, the larger the size of the capacitor is. Therefore, design requirement and available space must be considered when selecting the DC-link capacitance. Unlike $u_{\rm C}$ and $i_{\rm bat}$, DC-link capacitance variation has a negligible effect on the phase current.

4.3.2 Effects of Varying Cable Inductance

The cable inductance $L_{\rm ca}$ dictates how fast the battery current changes. Considering Equation (4.10), one can see that as $L_{\rm ca}$ increases, $i_{\rm bat}$ changes in a slower manner, and vice versa. And when $L_{\rm ca}$ increases, this allows the capacitor voltage $u_{\rm C}$ to attain higher levels, since it takes longer time for the current to be pushed to the battery. Figure 4.10 shows $i_{\rm bat}$ and $u_{\rm C}$ for different inductance values.

Setting up the cables properly minimizes their inductance. This results in lower peak battery currents and, hence, safer charging of the battery. It also results in smaller DC-link capacitance since the DC-link voltage ripples are also reduced. It should also be noted that phase currents do not change much with the cable inductance.

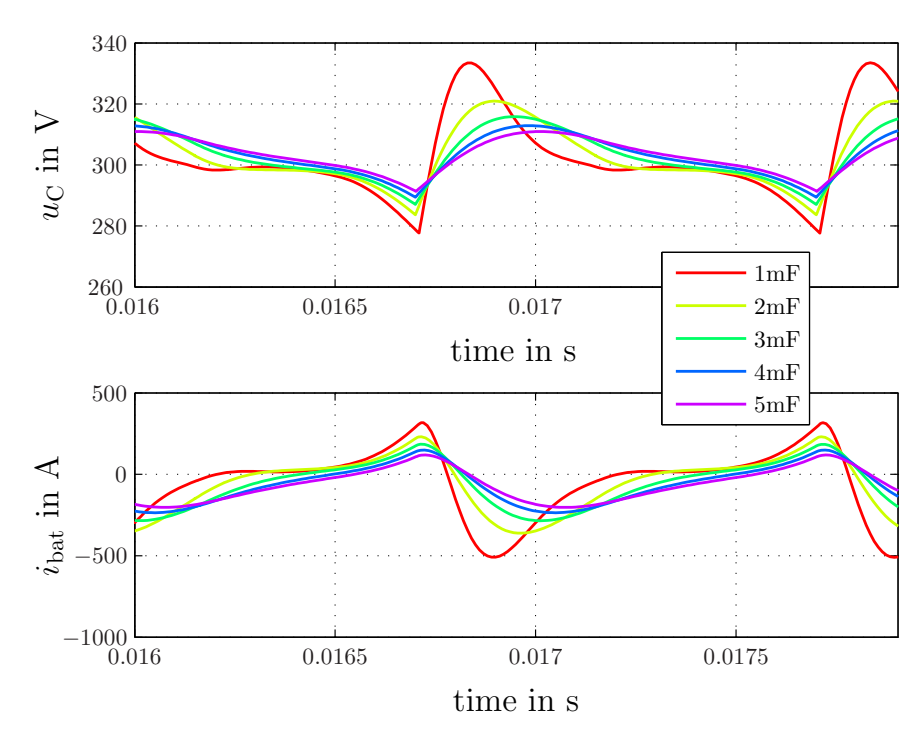


Figure 4.9: DC-link Voltage and Battery Current for Different DC-link Capacitances at 7500 rpm and Minimum Peak Radial Force Operation

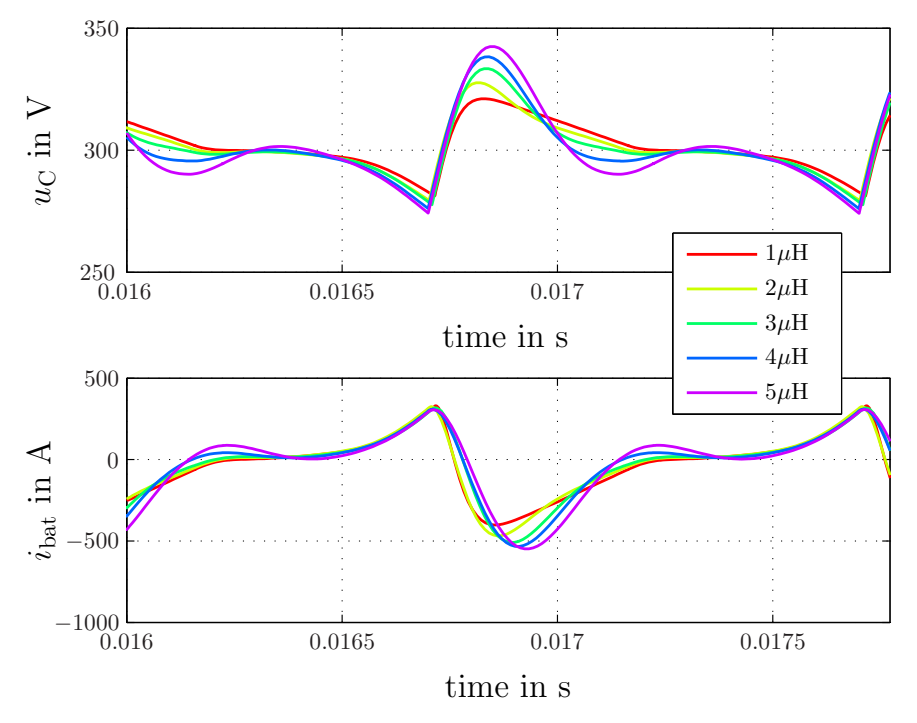


Figure 4.10: DC-link Voltage and Battery Current for Different Cable Inductances at 7500 rpm and Minimum Peak Radial Force Operation

4.3.3 Effects of Varying Battery Resistance

Changing the battery resistance $R_{\rm ser}$ affects the peak battery current $i_{\rm bat}$ largely. At $\theta > \theta_{\rm off}$, $i_{\rm bat}$ is still positive and there is a sudden increase in $u_{\rm C}$ due to the reverse polarity of $i_{\rm G}$. Since $u_{\rm C}$ is greater than $U_{\rm OC}$ at this moment, there is a negative net voltage across $L_{\rm ca}$ (Equation (4.10)), and $i_{\rm bat}$ starts to decrease. The rate of decline of $i_{\rm bat}$ also depend on $R_{\rm ser}$. When $i_{\rm bat}$ becomes negative, the smaller $R_{\rm ser}$, the more negative the voltage across $L_{\rm ca}$ is, and thus the faster $i_{\rm bat}$ will rise in the negative direction. This may cause problems to the batteries for they have a limit on the maximum allowed charging current. Figure 4.11 shows the DC-link voltage and battery current for different $R_{\rm ser}$ values. Despite these variations in $u_{\rm C}$ and $i_{\rm bat}$, the phase current does not change much with $R_{\rm ser}$.

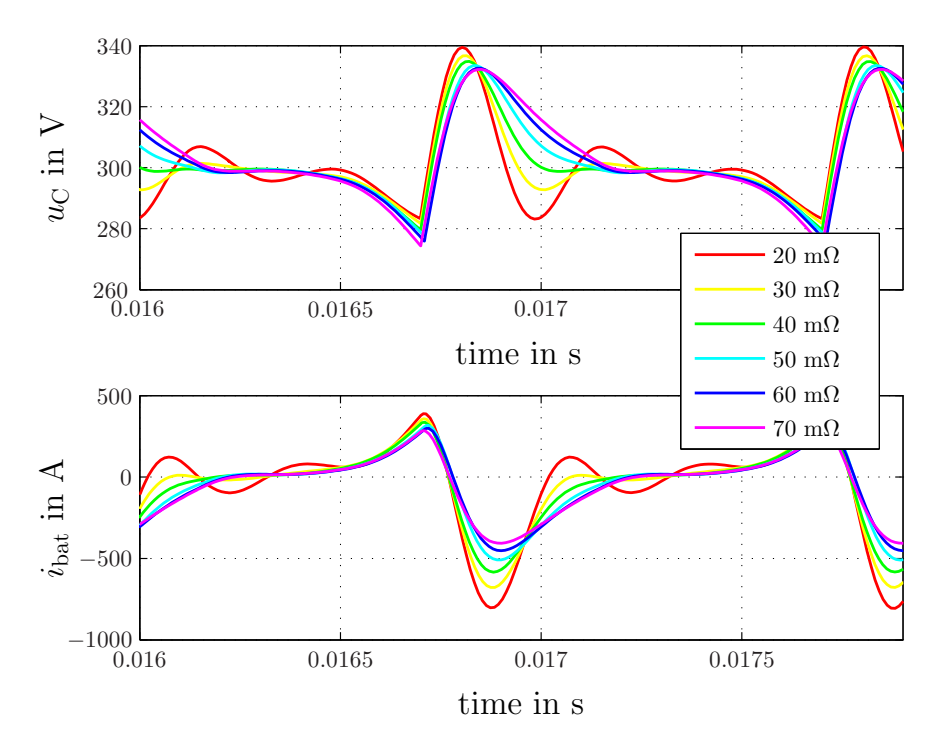


Figure 4.11: DC-link Voltage and Battery Current for Different Battery Series Resistances at 7500 rpm and Minimum Peak Radial Force Operation

4.3.4 Effects of Varying Battery Open-Circuit Voltage

As the open-circuit voltage of the battery $U_{\rm OC}$ is increasing due to charging, the average DC-link voltage $u_{\rm C}$ also increases. The increase in $u_{\rm C}$ leads to an increase in the phase currents, and this directly increases the torque and the radial forces. The DC-link voltage and battery current for different open-circuit voltages of an ideal battery are shown in Figure 4.12, and the generated power is given in Table 4.8.

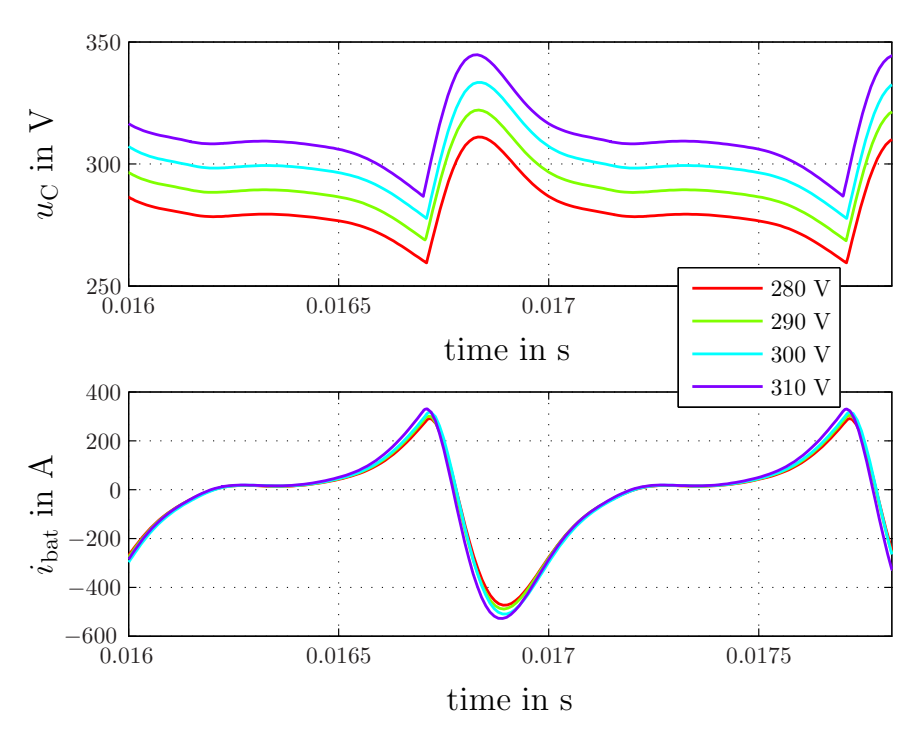


Figure 4.12: DC-link Voltage and Battery Current for Different Ideal Battery Open-circuit Voltage at 7500 rpm and Minimum Peak Radial Force Operation

Table 4.8: Ideal Battery Voltage Variations and Corresponding Generated Power

$U_{\rm OC}$ in V	$P_{\rm G}$ in kW
280	17.6
290	18.8
300	20.0
310	21.3

The variations in $P_{\rm G}$ will cause the mechanical system to decelerate as the voltage increases. Therefore, it is important to vary the control angles with the voltage, so the generated power does not change, and the shaft speed remains the same. The modified control angles are given in Table 4.9.

Table 4.9: Variations of Control Angles as Ideal Battery Voltage Changes to Meet Power Requirement at 7500 rpm

$U_{\rm OC}$ in V	$\theta_{\rm on}$ in °elec	$\theta_{\rm cond}$ in °elec
280	218	93
290	222	92
300	220	86
310	224	85

4.3.5 Using the Real Battery Model

The battery model consists 82 parallel branches, and each branch is a series connection of 91 cells (Section 3.4). According to Table 3.1, each cell can be charged by a maximum current of 5 A for a short time. Taking that into account, the battery pack charging current must not exceed 410 A.

In Figure 4.13 the radial force F and battery current i_{bat} for the ideal and real battery are shown. The battery state of charge (SOC) is set to 40% because this corresponds to an open-circuit voltage of 300 V, which is equivalent to that of the ideal battery. One can observe from the figure that optimizing using an ideal battery does not lead to differences in the force when a real battery model is used. However, there are differences in i_{bat} , which are mainly caused by the different series resistance of both models. In fact, the real battery model has a series resistance that is lower than $50 \, \text{m}\Omega$. This can also be anticipated considering the variations in the series resistance shown in Figure 4.11.

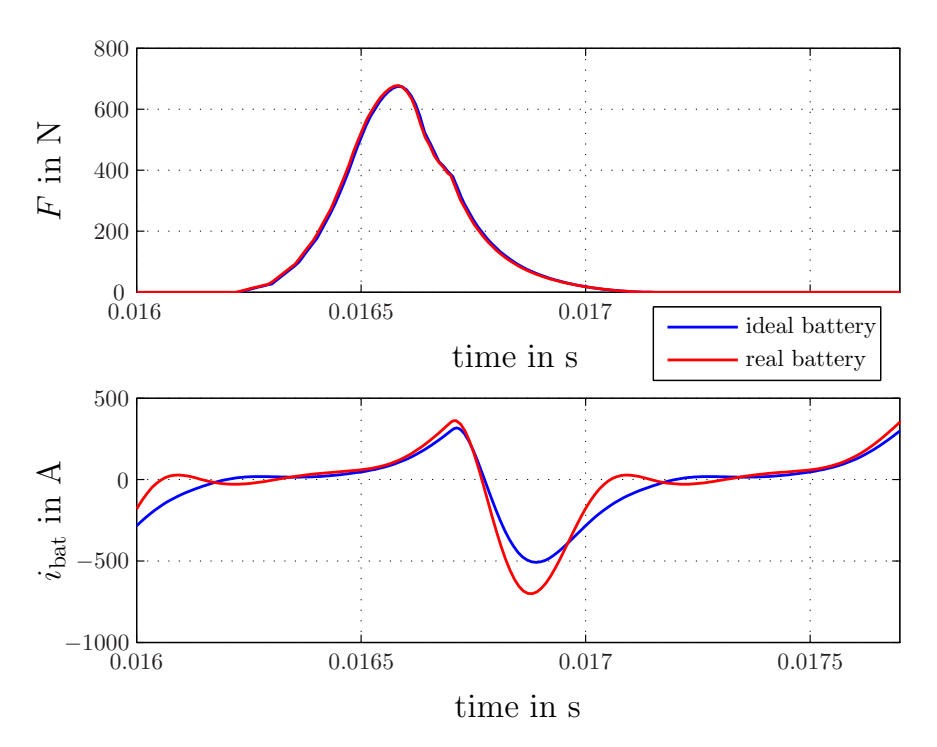


Figure 4.13: Radial Force and Battery Current for the Ideal and Real Battery Model

Despite the differences in i_{bat} between both models, the differences in i_{bat} for different SOCs are small. The battery current i_{bat} is shown in Figure 4.14 for different SOCs from 20 to 80%. The generated power varies from 19.5 kW at 20% SOC to 20.6 kW at 80% SOC. This implies that the control angles must be changed to maintain the same level of generation as the SOC varies. However, at all SOCs the charging current exceeds the limit. Therefore, an optimization process must take the limit into account for safe operation.

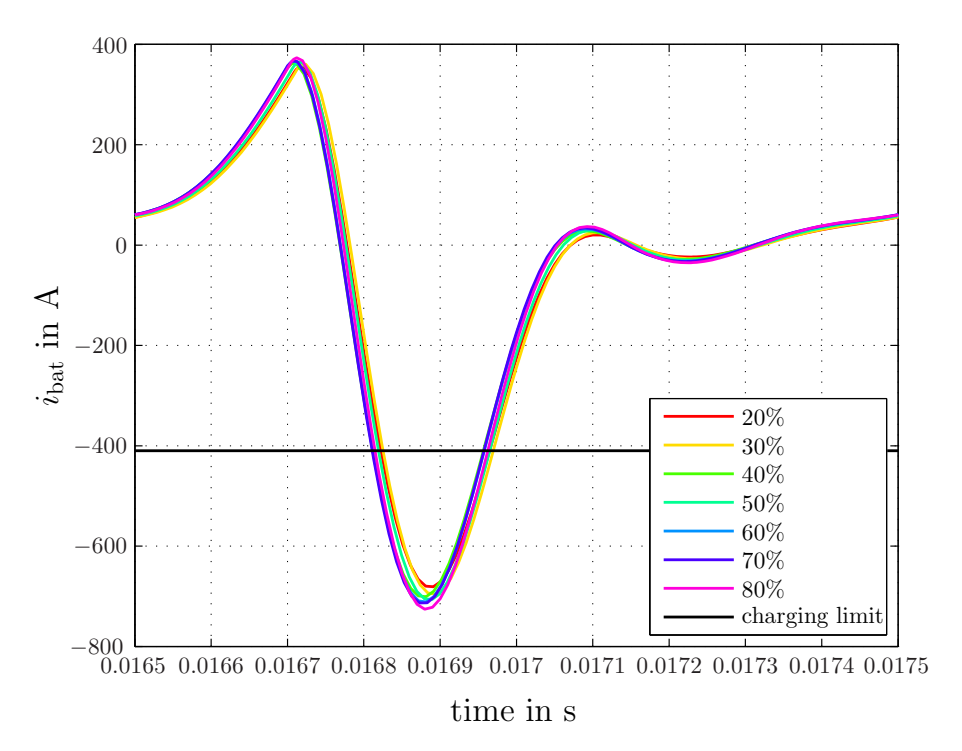


Figure 4.14: Battery Current for Different SOCs at 7500 rpm

Taking the battery charging limit into consideration, Figure 4.15 shows the battery current and radial force with and without free-wheeling angle control at 80% SOC in addition to those without any limitation. Simulation results are given Table 4.10. From the figure it is understandable that abiding by the charging limitation results in increased radial forces. Furthermore, free-wheeling helps in suppressing the forces more, and results in a better efficiency. Consequently, free-wheeling control results in an optimum operation considering the efficiency, the radial forces and the battery charging limit.

Table 4.10: Results for Cases shown in Figure 4.15

	w/o limiting	limiting w/o free-wheeling	limiting with free-wheeling
$\theta_{\rm on}$ in °elec	219	178	180
$\theta_{\rm fw}$ in °elec	_	_	251
$\theta_{\rm off}$ in °elec	303	268	298
$P_{\rm G}$ in kW	20.0	20.0	20.0
P_{bat} in kW	19.3	19.6	19.5
η in percent	95.1	96.6	96.6
$I_{\rm rms}$ in A	214.4	147.7	169.2
$F_{\rm max}$ in N	707.9	1328	941.0

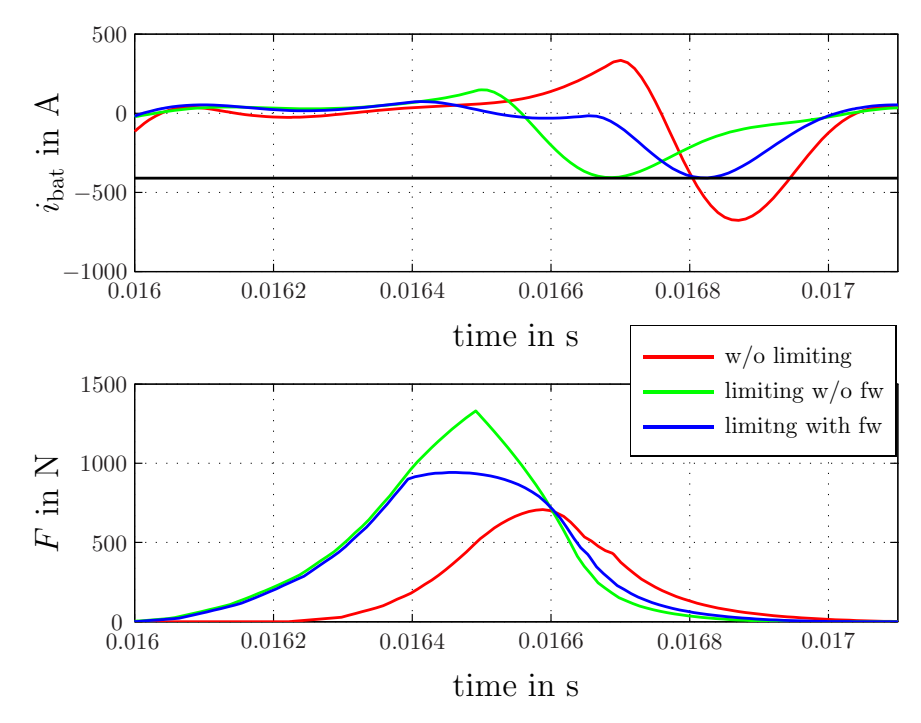


Figure 4.15: Battery Current and Radial Force at 80% SOC with Battery Current being Limited to Charging Limit

4.4 Optimization for Maximum Efficiency

Efficiency optimization aims to determine the optimum control angles for a specific operating point. In this section the influence of free-wheeling on maximizing efficiency is investigated. In addition, the effects of varying system parameters while operating at optimum, rated operating point are observed. Furthermore, strategies that aim to maximize efficiency and minimize rms current are compared. In addition, the differences between maximizing efficiency and minimizing excitation penalty are analyzed.

4.4.1 Influence of Free-wheeling on Efficiency

It might be intuitive that free-wheeling degrades efficiency because it allows for larger conduction periods, and, therefore, increases converter and copper losses. However, the phase voltage is reduced during free-wheeling, and this has an implication on the iron losses since a reduction in the phase voltage means lower rate of increase in the flux.

Shown in Figure 4.16 are the phase currents and phase fluxes for the most efficient performance at 7500 rpm. The results are given in Table 4.11. It is clear that free-wheeling produces lower iron losses as the peak flux value is reduced. On the other hand, the currents attain larger peak values, which result in higher converter and copper losses. Overall, the system efficiency increases.

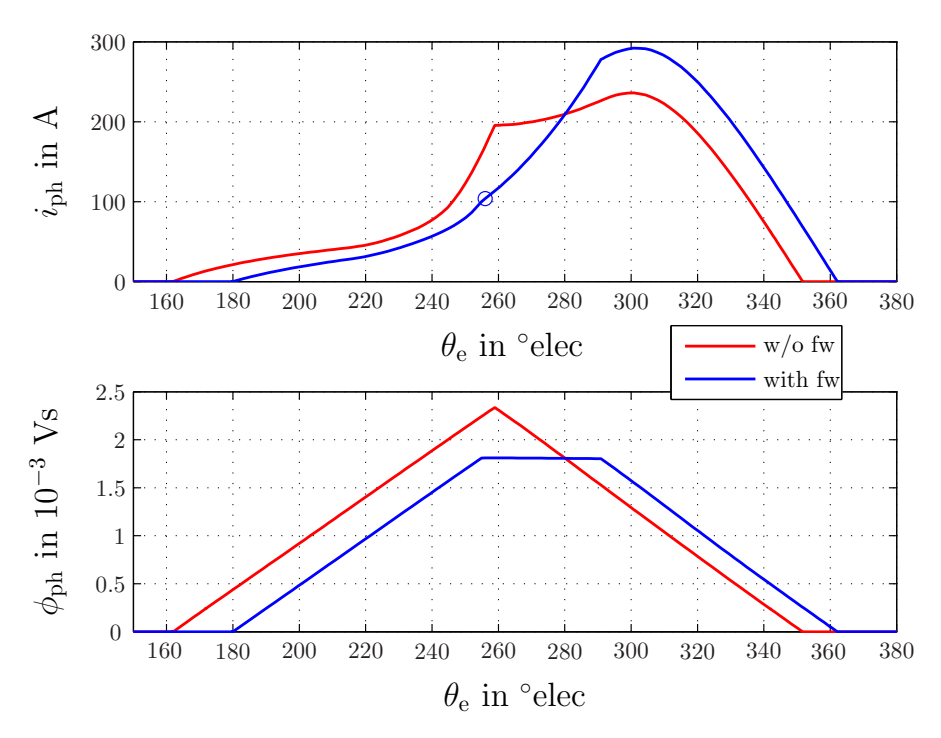


Figure 4.16: Phase Currents for Most Efficient Performance at 7500 rpm with and without Free-wheeling - Circle indicates Instant of Free-wheeling

Table 4.11: Results for the Cases shown in Figure 4.16

	without	with
	Free-wheeling	Free-wheeling
$P_{\rm G}$ in kW	20.0	20.0
P_{copper} in W	142	179
$P_{\rm conv}$ in W	253	268
P_{iron} in W	284	190
η in percent	96.6	96.8

At 3000 rpm the gain in efficiency is higher as the drop in iron losses outweighs the increase in the other losses by a bigger margin. The phase currents and fluxes are shown in Figure 4.17, and simulation results are given in Table 4.12.

Table 4.12: Results for the Cases shown in Figure 4.17

	without	with
	Free-wheeling	Free-wheeling
$P_{\rm G}$ in kW	7.0	7.0
P_{copper} in W	110	110
$P_{\rm conv}$ in W	150	188
P_{iron} in W	267	91
η in percent	92.6	94.5

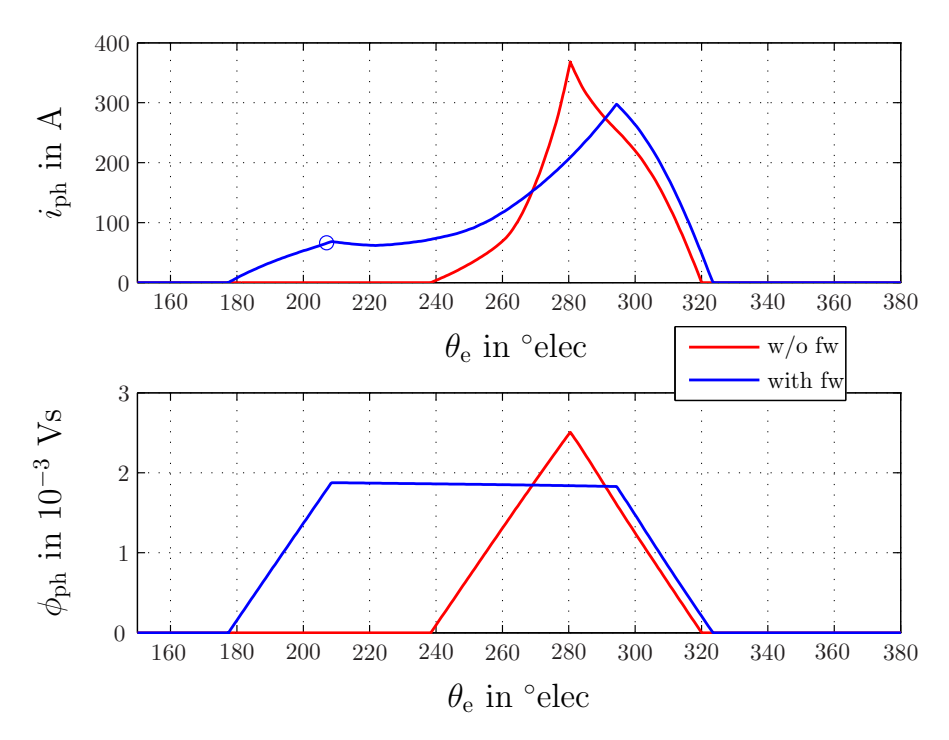


Figure 4.17: Phase Currents for Most Efficient Performance at 3000 rpm with and without Free-wheeling - Circle indicates Instant of Free-wheeling

4.4.2 Effects of Varying System Parameters

The effects of varying C, $L_{\rm ca}$, $R_{\rm ser}$ and $U_{\rm OC}$ have been analyzed in the previous section. The same changes apply when the control angles are chosen to maximize efficiency. However, phase currents in this case are wider and have lower peaks. This implies that the changes in $u_{\rm C}$ and $i_{\rm bat}$ are less drastic compared with the those in Section 4.3. From Figures 4.18 to 4.21, it can be seen that variations in C, $L_{\rm ca}$, $R_{\rm ser}$ and $U_{\rm OC}$ lead to lower amplitudes in $u_{\rm C}$ and $i_{\rm bat}$ compared with Figures 4.9 to 4.12.

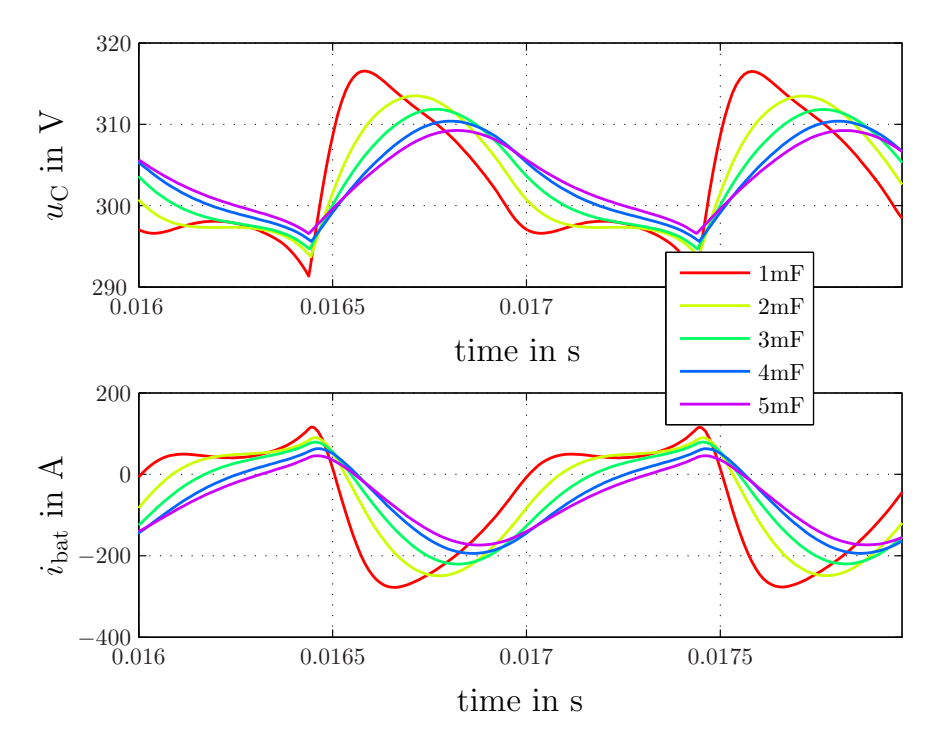


Figure 4.18: DC-link Voltage and Battery Current for Different DC-link Capacitances at 7500 rpm and Maximum Efficiency Operation

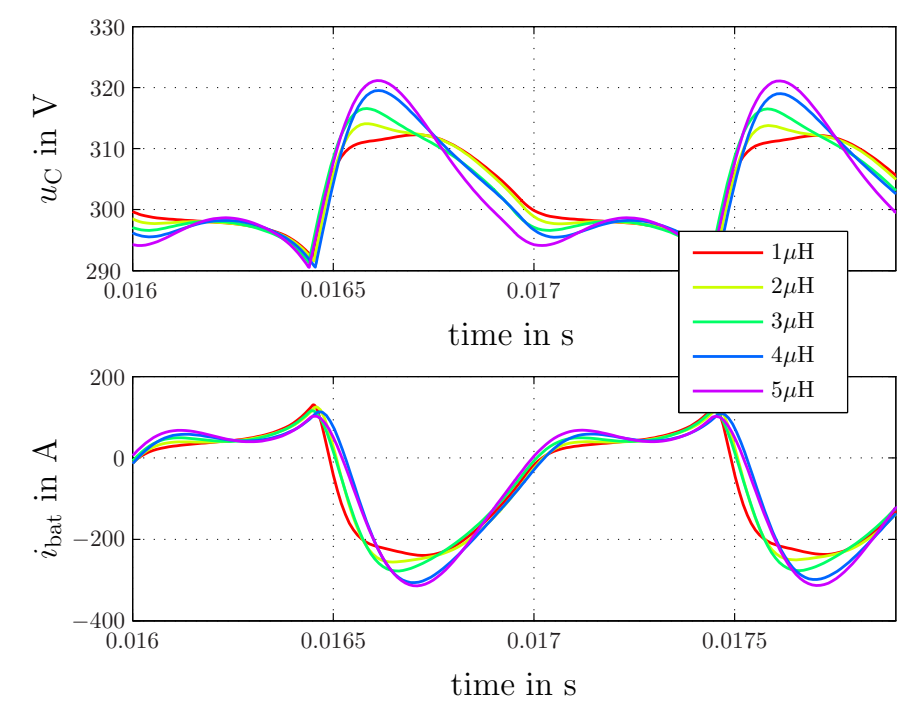


Figure 4.19: DC-link Voltage and Battery Current for Different Cable Inductances at 7500 rpm and Maximum Efficiency Operation

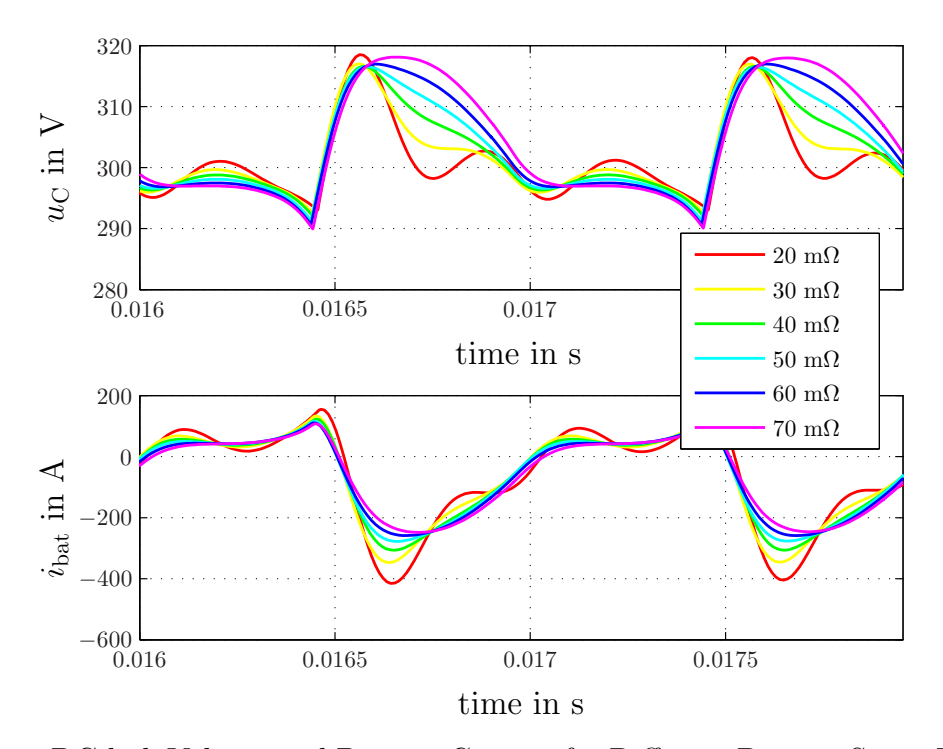


Figure 4.20: DC-link Voltage and Battery Current for Different Battery Series Resistances at 7500 rpm and Maximum Efficiency Operation

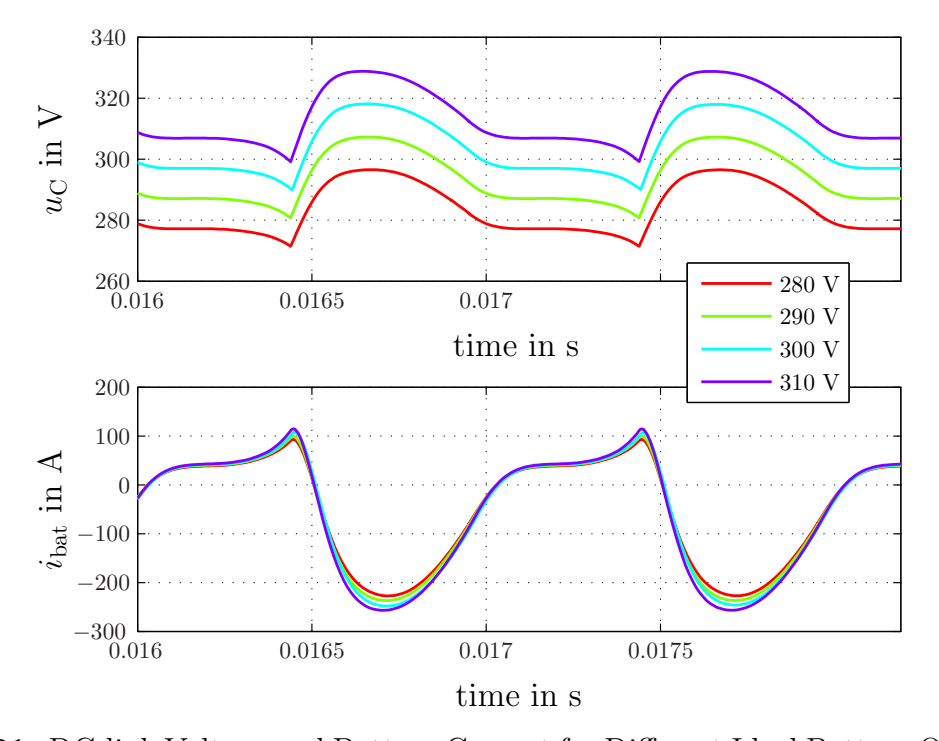


Figure 4.21: DC-link Voltage and Battery Current for Different Ideal Battery Open-circuit Voltage at 7500 rpm and Maximum Efficiency Operation

4.4.3 Using the Real Battery Model

Control angles that are optimized for efficiency result in phase currents with lower peaks compared with those optimized for minimum radial force. This is an advantage for the battery, because the chances of exceeding the charging limit are reduced. Figure 4.22 shows the battery current for different SOCs at 7500 rpm. Obviously, the current is always smaller than the limit.

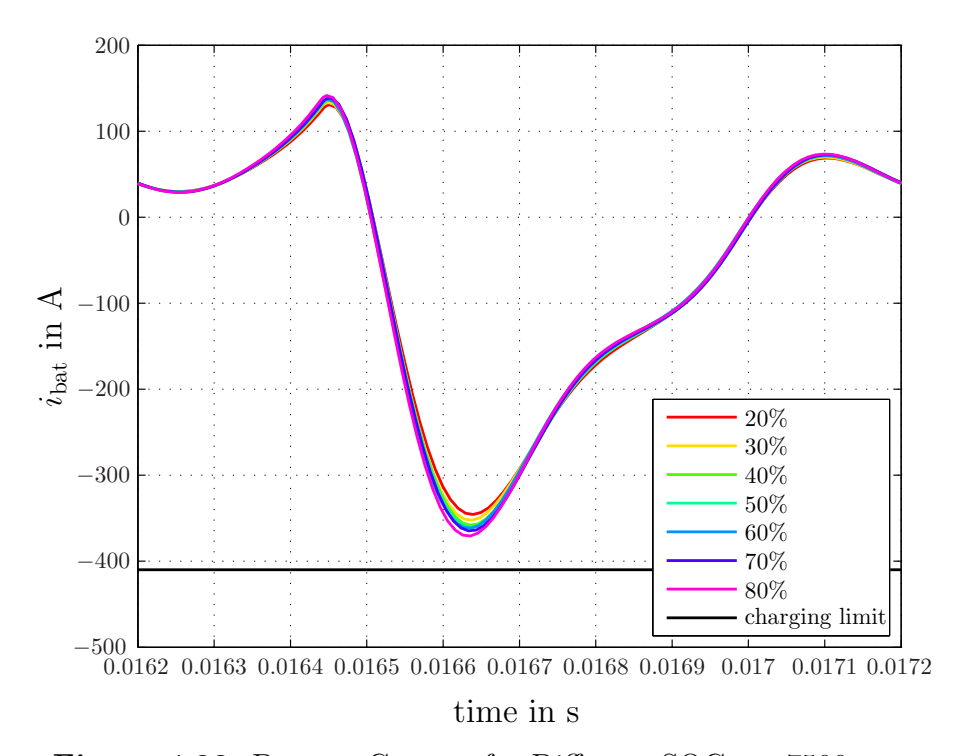


Figure 4.22: Battery Current for Different SOCs at 7500 rpm

4.4.4 Efficiency and RMS Current Optimization

Calculating efficiency requires the determination of all losses in the system. While it is easy to determine some of the losses like copper and converter losses, others such as iron losses require lengthy computations that make the optimization process slow. Since various losses depend on the current, minimizing the rms current leads to increased system efficiency [20, 30], and it can be computed in a faster manner compared to efficiency. Using Figure 4.3, the fitness value in an rms current minimization process FV_I is computed by

$$FV_{I} = f(P, I_{\text{rms}}) = F_{P}W_{P} + F_{I}W_{I}$$

$$= \left(1 - \left[\frac{1}{P_{\text{req}}}|P - P_{\text{req}}|\right]\right)(0.9) + \left(1 - \frac{I_{\text{rms}}}{I_{\text{rms}}^{\text{limit}}}\right)(0.1)$$
(4.11)

The operation of the SRG is optimized for the two criteria at shaft speeds equal to 3000, 4000, 5000, 6000 and 7500 rpm. At each speed the generated power is equal to the ICE power shown in Table 3.2. The turn-on and turn-off angles are shown in Figure 4.23. From the figure it can be concluded that both optimization processes yield angles that are equal or close to each other. Therefore, using the rms current as an efficiency indicator is reasonable.

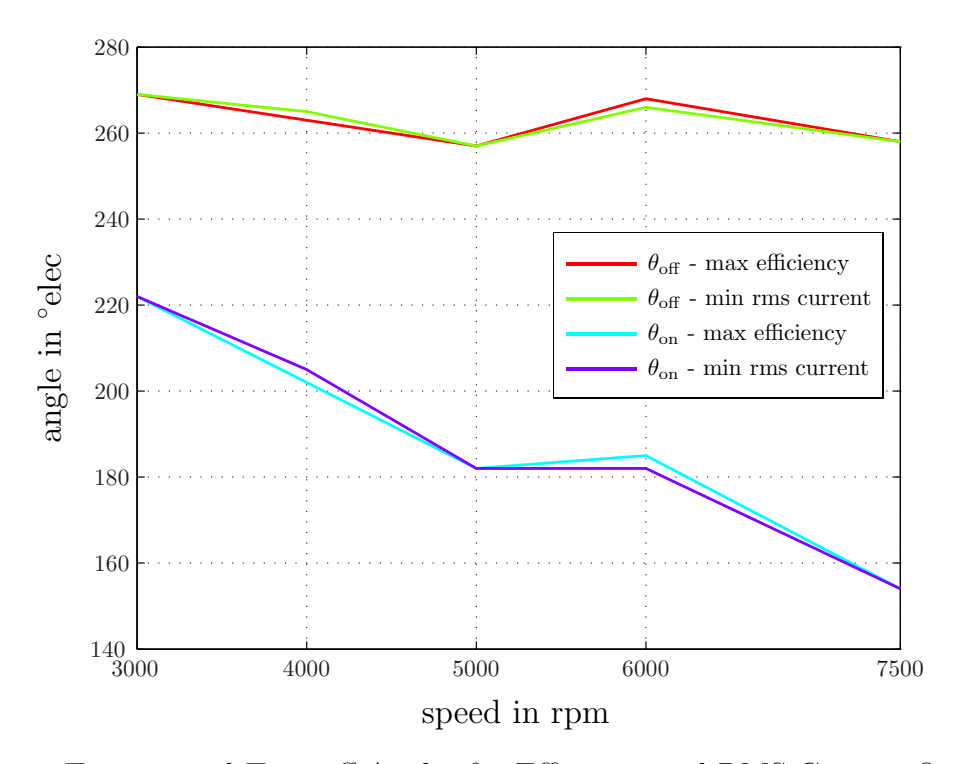


Figure 4.23: Turn-on and Turn-off Angles for Efficiency and RMS Current Optimization

4.4.5 Efficiency and Excitation Penalty Optimization

The excitation penalty ϵ , which is defined in Equation (2.18), tells how much energy is used for excitation compared to the generated energy. Minimizing ϵ can also be the goal of an optimization process in which the fitness value is calculated by

$$FV_{\epsilon} = f(P,\epsilon) = F_P W_P + F_{\epsilon} W_{\epsilon}$$

$$= \left(1 - \left[\frac{1}{P_{\text{req}}} |P - P_{\text{req}}|\right]\right) (0.9) + (1 - \epsilon)(0.1)$$
(4.12)

Optimizing the three operating points shown in Table 4.1 for minimum ϵ results in the same control angles as for maximum efficiency optimization. Therefore, the parameter ϵ provides good efficiency estimation, and it is easier to calculate compared to efficiency.

4.5 Summary of Efficiency and Radial Force Optimization Processes

In this chapter the performance of the range extender system has been optimized for maximizing efficiency and minimizing the peak radial forces. The effect of using free-wheeling has been analyzed for both optimizations. In addition, sensitivity analyses for changes in system parameters have been provided.

To reduce the radial forces the phase must conduct near the aligned position. This results in high current peaks that may damage the power electronic converter. Therefore, setting up a limit on the phase current seems reasonable. However, this will lead to increased radial forces. At 7500 rpm the trade-off between the peak current and peak radial force is not substantial for current limits of 500 and 400 A. But for a 300-A limit there is large increase in the radial force. Moreover, introducing free-wheeling at this speed does not reduce the peak radial force a lot. The reason for this is the large phase conduction period to meet the power requirement with the large back-EMF. As a result, there is not much room for free-wheeling because the generated power is simple zero as the phase current free-wheels. That is why a free-wheeling is introduced slightly before turning off the switches (Figure 4.7). At 3000 rpm the phase currents are characterized by smaller widths and larger peaks. Therefore, free-wheeling allows to widen the current pulses, and this results in lower current and force peaks (Figure 4.8).

Efficiency optimization aims at reducing the losses. While free-wheeling causes higher conduction and copper losses, it helps in reducing the iron losses because the total voltage across the phase while free-wheeling is low. For shaft speeds of 3000 and 7500 rpm trade-offs between the current-associated losses and iron losses that result in increased efficiency have been obtained with the use of free-wheeling (Figures 4.16 and 4.17 and Tables 4.11 and 4.12). Moreover, it has been found that both the rms current and excitation penalty are closely correlated to efficiency. As a results, an optimization process that is aimed to minimize either quantities will lead to control parameters that are equal or close to the optimum parameters.

So far the radial force has been analyzed in the time domain. While reducing the peak force seems logical, this may not necessarily lead to better harmonic content. In Figure 4.24 the frequency analysis of different optimization processes is shown. One can observe that force optimization reduce the lower harmonics, but the reduction is less than 10 dB. Furthermore, utilizing free-wheeling results in certain harmonics being suppressed more than without utilizing it. As a result, free-wheeling might not be the perfect solution for the noise problem, but it provides one more degree of freedom to alter shape of the phase current, and, consequently, improve the acoustic behavior of the SR machine. Despite that, free-wheeling angle angle control has already been proved to be superior to hysteresis current control with regard to the resultant acoustic response [13].

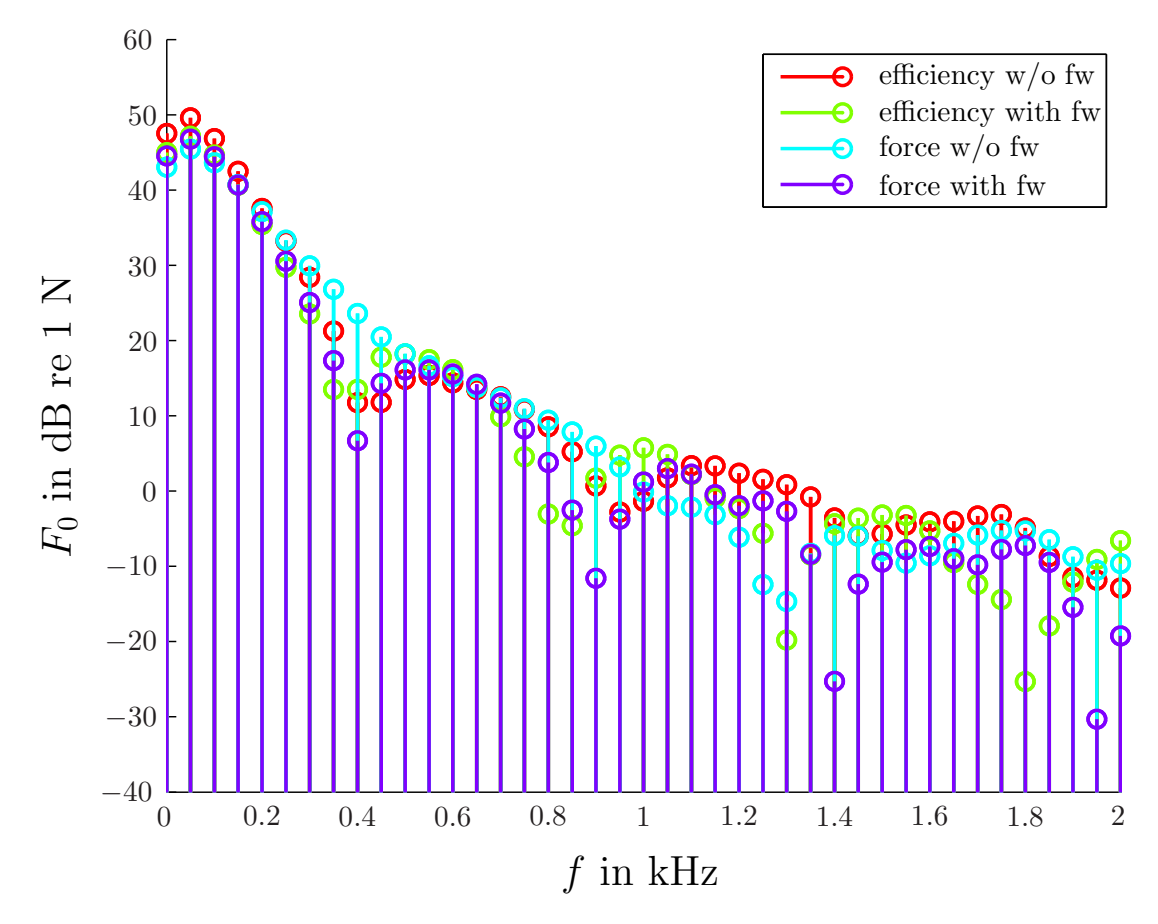


Figure 4.24: Harmonic Content of Radial Forces for Different Optimization Processes

5 Conclusions and Further Work

In this thesis a model of a range extender system has been developed in MATLAB/Simulink, and the model has been used to study and analyze the performance of the system. The model consists of an internal combustion engine, a switched reluctance generator (SRG), a power electronic converter, a DC-link and cable, and a battery pack. The SRG is set to operate in the single-pulse mode for a speed range between 3000 and 7500 rpm. After developing the model, the performance of the system has been optimized for two criteria, which are minimizing the peak radial force and maximizing efficiency. It has been shown that, in order to minimize the radial forces, free-wheeling angle control provides better performance at low speeds than at high speeds. In addition, free-wheeling achieves better efficiency for all speed ranges, as it reduces the iron losses. Furthermore, it has been proved that minimizing the rms current or the excitation penalty could be used as criteria for maximum efficiency optimization. The effects of using a real battery model has been investigated, and it has been shown that free-wheeling provides optimum performance with regard to efficiency, radial force behavior and battery charging limit.

There are many aspects that could be focused on for further development. For example, a through investigation of the existing converter topologies could be carried out to determine the most convenient topology for the range extender system. In addition, control and filtering techniques that aim to optimize the acoustic behavior of the SRG could be implemented. It has been shown in this work that the harmonic content in the radial forces cannot be altered substantially with simple variations of control parameters. Therefore, advanced control techniques must be adopted to achieve a better acoustic response. In addition, a comparison between different SRG configurations with regard to DC-link voltage and current ripples could done. Since a two-phase SRG results in high voltage and current ripples in the DC-link, generators with higher number of phases could be used to reduce the ripples at the expense of higher number of connections. Therefore, a trade-off between the number of phases and the ripples could be analyzed.

List of Figures

1.1	Block Diagram of Range Extender System	1
2.1	Cross-sectional View of a Switched Reluctance Machine	4
2.2	One-phase Switched Reluctance Machine	5
2.3	Equivalent Circuit Diagram of a One-phase Switched Reluctance Machine	6
2.4	Linear Variations of Phase Inductance with Rotor Position	7
2.5	One-phase Asymmetric Half-bridge Converter	8
2.6	Typical Phase Currents at High Shaft Speeds	9
2.7	Different Stages of an Electrical Cycle	10
2.8	Typical Phase Currents at Low Shaft Speed	11
2.9	Two-phase Asymmetric Half-bridge Converter	11
2.10	One-phase Asymmetric Half-bridge Converter with Realistic Devices	16
2.11	J	17
2.12	Roulette Wheel Parent Selection Scheme	20
	Crossover	21
2.14	Mutation	21
3.1	Overview of Range Extender System	22
3.2	Cross-sectional view of the SRG used in the Model	22
3.3	Overview of a One-phase SRG Model	23
3.4	Phase Inductance as a Function of Electrical Angle and MMF	24
3.5	Phase Torque as a Function of Electrical Angle and MMF	24
3.6	Tooth Radial Force as a Function of Electrical Angle and MMF	25
3.7	Block Diagram of a One-phase Switched Reluctance Generator	25
3.8	Overview of Power Electronic Converter Model	26
3.9	DC-link Circuit Diagram	27
3.10	Block Diagram of the DC-link	27
3.11	Overview of Battery Model	28
	Electrical Model of a Battery Cell	29
3.13	Electrical Model of an Ideal Battery	29
3.14	Internal Combustion Engine Model	30
3.15	Measured and Estimated Engine Torque at 7750 rpm	31
3.16	Estimated Instantaneous Engine Torque	32
3.17	Torque generation for crankshaft angles between 270° and 360°	33
3.18	Torque generation for crankshaft angles between 360° and 450°	33
3.19	Mechanical System Model	34
3.20	Average Power Flow in the Range Extender System	35
	Diagram showing Complete Electrical System and ICE	36

List of Figures 73

	Flux Paths at the Aligned Position of: a) Phase 1 and b) Phase 2	37
	Partitioning of the SRG into Different Sections	37
	Flux in SP1 at the Aligned Position of: a) Phase 1 and b) Phase 2	38
	Flux in SY1 and SY6 at the Aligned Position of: a) Phase 1 and b) Phase 2	39
3.26	Flux in RP1 during a Half Mechanical Revolution	40
3.27	Flux in RY1 during a Half Mechanical Revolution	40
3.28	Phase Flux Waveforms and Flux Waveforms in SP1, RP1, SY1 and RY1 $$	41
3.29	Stator and Rotor Dimensions	42
3.30	Relationship between IGBT Current and Switching Losses	45
4.1	Optimization Process using Genetic Algorithms	47
4.2	Breakdown of Information carried in a Chromosome	48
4.3	Fitness Functions of Different Criteria	49
4.4	Comparison of Most Efficient and Minimum Radial Force Operating Point at	
	7500 rpm	51
4.5	Comparison of Most Efficient and Minimum Radial Force Operating Point at	
	5000 rpm and 12.5 kW	52
4.6	Comparison of Most Efficient and Minimum Radial Force Operating Point at	۲.
4 7	3000 rpm	53
4.7	Phase Current and Radial Force for Different Phase Current Limits at 7500 rpm - Circles indicate Instants of Free-wheeling	54
4.8	Phase Current and Radial Force for Different Phase Current Limits at 3000	94
4.0	rpm - Circles indicate Instants of Free-wheeling	55
4.9	DC-link Voltage and Battery Current for Different DC-link Capacitances at	00
1.0	7500 rpm and Minimum Peak Radial Force Operation	57
4 10	DC-link Voltage and Battery Current for Different Cable Inductances at 7500	01
1.10	rpm and Minimum Peak Radial Force Operation	57
4 11	DC-link Voltage and Battery Current for Different Battery Series Resistances	01
1.11	at 7500 rpm and Minimum Peak Radial Force Operation	58
4.12	DC-link Voltage and Battery Current for Different Ideal Battery Open-circuit	
1.12	Voltage at 7500 rpm and Minimum Peak Radial Force Operation	59
4.13	Radial Force and Battery Current for the Ideal and Real Battery Model	60
	Battery Current for Different SOCs at 7500 rpm	61
	Battery Current and Radial Force at 80% SOC with Battery Current being	01
	Limited to Charging Limit	62
4.16	Phase Currents for Most Efficient Performance at 7500 rpm with and without	0_
1.10	Free-wheeling - Circle indicates Instant of Free-wheeling	63
4.17	Phase Currents for Most Efficient Performance at 3000 rpm with and without	
1.1.	Free-wheeling - Circle indicates Instant of Free-wheeling	64
4.18	DC-link Voltage and Battery Current for Different DC-link Capacitances at	0 1
1.10	7500 rpm and Maximum Efficiency Operation	65
4.19	DC-link Voltage and Battery Current for Different Cable Inductances at 7500	30
1.10	rpm and Maximum Efficiency Operation	65
4.20	DC-link Voltage and Battery Current for Different Battery Series Resistances	33
	at 7500 rpm and Maximum Efficiency Operation	66

List of Figures 74

4.21	DC-link Voltage and Battery Current for Different Ideal Battery Open-circuit	
	Voltage at 7500 rpm and Maximum Efficiency Operation	66
4.22	Battery Current for Different SOCs at 7500 rpm	67
4.23	Turn-on and Turn-off Angles for Efficiency and RMS Current Optimization .	68
4.24	Harmonic Content of Radial Forces for Different Optimization Processes	70

List of Tables

2.1	States the Asymmetrical Half-bridge Converter	8
3.1	Parameters of LiFePO ₄ Cell by A123 Systems [1]	28
3.2	Torque and Power Capability of the Internal Combustion Engine	30
3.3	Values of Dimensions in Figure 3.29	42
3.4	Specific Loss of M330-35A Ferrite Material in W/kg	44
3.5	Steinmitz Parameters of M330-35A Ferrite Material	44
4.1	Considered Operating Points	50
4.2	Values of Parameters in the Range Extender System	50
4.3	Results for the Cases shown in Figure 4.4	51
4.4	Results for the Cases shown in Figure 4.5	52
4.5	Results for the Cases shown in Figure 4.6	53
4.6	Efficiency and DC-link Voltage Ripple for the Cases in Figure 4.7	55
4.7	Efficiency and DC-link Voltage Ripple for the Cases in Figure 4.8	56
4.8	Ideal Battery Voltage Variations and Corresponding Generated Power	59
4.9	Variations of Control Angles as Ideal Battery Voltage Changes to Meet Power	
	Requirement at 7500 rpm	59
4.10	Results for Cases shown in Figure 4.15	61
4.11	Results for the Cases shown in Figure 4.16	63
4.12	Results for the Cases shown in Figure 4.17	63

Bibliography

- [1] A123Systems. High Power Lithium Ion APR18650M1.
- [2] Aharon, I. and Kuperman, A. 'Topological Overview of Powertrains for Battery-Powered Vehicles With Range Extenders'. In: *Power Electronics, IEEE Transactions on* 26.3 (Mar. 2011), pp. 868 –876. ISSN: 0885-8993. DOI: 10.1109/TPEL.2011.2107037.
- [3] Barnes, M. and Pollock, C. 'Power electronic converters for switched reluctance drives'. In: *Power Electronics, IEEE Transactions on* 13.6 (Nov. 1998), pp. 1100 –1111. ISSN: 0885-8993. DOI: 10.1109/63.728337.
- [4] Buller, S. et al. 'Impedance-based simulation models of supercapacitors and Li-ion batteries for power electronic applications'. In: *Industry Applications, IEEE Transactions on* 41.3 (May 2005), pp. 742 –747. ISSN: 0093-9994. DOI: 10.1109/TIA.2005.847280.
- [5] Cameron, D. and Lang, J. 'The control of high-speed variable-reluctance generators in electric power systems'. In: *Industry Applications, IEEE Transactions on* 29.6 (Nov. 1993), pp. 1106 –1109. ISSN: 0093-9994. DOI: 10.1109/28.259720.
- [6] Cardenas, R. et al. 'Control of a switched reluctance generator for variable-speed wind energy applications'. In: *Energy Conversion, IEEE Transactions on* 20.4 (Dec. 2005), pp. 781 –791. ISSN: 0885-8969. DOI: 10.1109/TEC.2005.853733.
- [7] Carstensen, C. 'Eddy Currents in Windings of Switched Reluctance Machines'. PhD thesis. RWTH Aachen University, 2008.
- [8] Chapman, S. J. Electric Machinery Fundamentals. McGraw-Hill, 2005.
- [9] cogent. Electrical Steel Non Oriented Fully Processed.
- [10] De Doncker, R. et al. Advanced Eelctrical Drives. Springer, 2011.
- [11] Emadi, A. et al. 'Topological overview of hybrid electric and fuel cell vehicular power system architectures and configurations'. In: *Vehicular Technology, IEEE Transactions on* 54.3 (May 2005), pp. 763 –770. ISSN: 0018-9545. DOI: 10.1109/TVT.2005.847445.
- [12] Faiz, J. and Fazai, R. 'Optimal Excitation Angles of a High Speed Switched Reluctance Generator by Efficiency Maximization'. In: *Power Electronics and Motion Control Conference*, 2006. EPE-PEMC 2006. 12th International. 30 2006-sept. 1 2006, pp. 287–291. DOI: 10.1109/EPEPEMC.2006.4778414.
- [13] Kasper, K. 'Analysis and Control of the Acoustic Behavior of Switched Reluctance Drives'. PhD thesis. RWTH Aachen University, 2011.
- [14] Kioskeridis, I. and Mademlis, C. 'Optimal efficiency control of switched reluctance generators'. In: *Power Electronics, IEEE Transactions on* 21.4 (July 2006), pp. 1062 –1072. ISSN: 0885-8993. DOI: 10.1109/TPEL.2006.876827.

Bibliography 77

[15] Mademlis, C. and Kioskeridis, I. 'Optimizing Performance in Current-Controlled Switched Reluctance Generators'. In: *Energy Conversion, IEEE Transactions on* 20.3 (Sept. 2005), pp. 556–565. ISSN: 0885-8969. DOI: 10.1109/TEC.2005.852960.

- [16] Man, K. et al. Genetic Algorithms. London, UK: Springer, 1999.
- [17] Materu, P. and Krishnan, R. 'Estimation of switched reluctance motor losses'. In: *Industry Applications, IEEE Transactions on* 28.3 (May 1992), pp. 668 –679. ISSN: 0093-9994. DOI: 10.1109/28.137456.
- [18] Menne, M. et al. 'Critical states in generating mode of switched reluctance machines'. In: Power Electronics Specialists Conference, 2000. PESC 00. 2000 IEEE 31st Annual. Vol. 3. 2000, 1544 –1550 vol.3. DOI: 10.1109/PESC.2000.880535.
- [19] Merker, G. et al. Grundlagen Verbrennungsmotoren: Funktionsweise, Simulation, Messtechnik. Atz/Mtz-Fachbuch. Springer Verlag, 2011. ISBN: 9783834813930.
- [20] Mese, E. et al. 'Optimal excitation of a high speed switched reluctance generator'. In: Applied Power Electronics Conference and Exposition, 2000. APEC 2000. Fifteenth Annual IEEE. Vol. 1. 2000, 362 –368 vol.1. DOI: 10.1109/APEC.2000.826128.
- [21] Miller, T. Switched Reluctance Motors and Their Control. Monographs in Electrical and Electronic Engineering. Magna Physics, 1993. ISBN: 9780198593874. URL: http://books.google.co.uk/books?id=DtpiQgAACAAJ.
- [22] Mohan, N. et al. Power Electronics: Converters, Applications, and Design. Wiley, 2003.
- [23] Polaris Range EXtender Technology (REX). Polaris. May 2011. URL: http://www.dtic.mil/ndia/2011power/Session23_12836Stewart.pdf.
- [24] Range Extender Engines. Lotus Engineering. URL: http://issuu.com/lotuscars/docs/lotus_range_extender_r1?mode=window&printButtonEnabled=false&shareButtonEnabled=false&searchButtonEnabled=true&backgroundColor=%23222222.
- [25] Rogge, M. 'Simulation und regelungstechnische Optimierung eines Range-Extenders für den Einsatz in Elektrofahrzeugen'. MA thesis. RWTH Aachen University, 2011.
- [26] Semikron. SEMiX402GAL066HDs.
- [27] Semikron. SEMiX402GAR066HDs.
- [28] Sozer, Y. and Torrey, D. 'Closed loop control of excitation parameters for high speed switched-reluctance generators'. In: *Power Electronics, IEEE Transactions on* 19.2 (Mar. 2004), pp. 355 –362. ISSN: 0885-8993. DOI: 10.1109/TPEL.2003.823178.
- [29] Taylor, W. H. 'Obtaining Motive Power'. 8255. 1840.
- [30] Torrey, D. 'Switched reluctance generators and their control'. In: *Industrial Electronics*, *IEEE Transactions on* 49.1 (Feb. 2002), pp. 3 –14. ISSN: 0278-0046. DOI: 10.1109/41.982243.
- [31] Veltman, A. et al. Fundamentals of Electrical Drives. Springer, 2007.

Bibliography 78

[32] Venkatachalam, K. et al. 'Accurate prediction of ferrite core loss with nonsinusoidal waveforms using only Steinmetz parameters'. In: Computers in Power Electronics, 2002. Proceedings. 2002 IEEE Workshop on. June 2002, pp. 36–41. DOI: 10.1109/CIPE.2002.1196712.

[33] West, J. 'DC, induction, reluctance and PM motors for electric vehicles'. In: *Power Engineering Journal* 8.2 (Apr. 1994), pp. 77–88. ISSN: 0950-3366. DOI: 10.1049/pe: 19940203.